STATE SPACE GEOMETRY OF LOW DIMENSIONAL QUANTUM MAGNETS

James Lambert, B.Sc.

A Thesis Submitted to the School of Graduate Studies in
Partial Fulfilment of the Requirements for the Degree Doctor of Philosophy

December 18, 2022

McMaster University

Doctor of Philosophy (2022)

Hamilton, Ontario (Department of Physics and Astronomy)

TITLE: State Space Geometry of Low Dimensional Quantum Magnets

AUTHOR: J. Lambert, B.Sc.

SUPERVISOR: Dr. Erik S. Sørensen

NUMBER OF PAGES: 102

Lay Abstract

Systems composed of many bodies tend to order as their energy is reduced. Steam, a state characterized by the complete disorder of the constituent water molecules, condenses to liquid water as the temperature (energy) decreases, wherein the water molecules are organized enough for insects to walk atop them. Water freezes to ice, which is so ordered that it can hold sleds and skaters. Quantum mechanics allows for patterns of organization that go beyond the solid-liquid-gas states. These patterns are manifest in the smallest degrees of freedom in a solid, the electrons, and are responsible for fridge magnets and transistors. While quantum systems still tend to order at lower energies, they are characterized by omni-present fluctuations that can conceal hidden forms of organization. One can imagine that the states of matter live in a vast space, where each point represents a different pattern. In this thesis we show that by probing the geometry of this space, we can detect hidden kinds of order that would be otherwise invisible to us.

Abstract

In recent decades enormous progress has been made in studying the geometrical structure of the quantum state space. Far from an abstraction, this geometric structure is defined operationally in terms of the distinguishability of states connected by parameterizations that can be controlled in a laboratory. This geometry is manifest in the kinds of response functions that are measured by well established experimental techniques, such as inelastic neutron scattering. In this thesis we explore the properties of the state space geometry in the vicinity of the ground state of two paradigmatic models of low dimensional magnetism. The first model is the spin-1 anti-ferromagnetic Heisenberg chain, which is a central example of symmetry protected topological physics in one dimension, exhibiting a non-local string order, and symmetry protected short range entanglement. The second is the Kitaev honeycomb model, a rare example of an analytically solvable quantum spin liquid, characterized by long range topological order.

In Chapter 2 we employ the single mode approximation to estimate the genuine multipartite entanglement in the spin-1 chain as a function of the unaxial anisotropy up to finite temperature. We find that the genuine multipartite entanglement exhibits a finite temperature plateau, and recove the universality class of the phase transition induced by negative anisotropy be examining the finite size scaling of the quantum Fisher information. In Chapter 4 we map out the zero temperature phase diagram in terms of the QFI for a patch of the phase space parameterized by the anisotropy and applied magnetic field, establishing that any non-zero anisotropy enhances that entanglement of the SPT phase, and the robustness of the phase to finite temperatures. We also establish a connection between genuine multipartite entanglement and state space curvature.

In Chapter 3 we turn to the Kitaev honeycomb model and demonstrate that, while the QFI associated to local operators remains trivial, the second derivative of such quantities with respect to the driving parameter exhibit divergences. We characterize the critical exponents associated with these divergences.

Acknowledgements

So much of this thesis is owed to my supervisor Dr. Erik S. Sørensen, who encouraged me to pursue my curiosity wherever it might take me. His patience and guidance were invaluable. To Duncan O'Dell and Sung-Sik Lee, thank you for the many lessons you've taught me in committee meetings and classes.

Sarah, Joe, Alex, Wyatt, Hector, Jon, Alejandra, Laszlo, Julie, Carmen, Claude, Thanassis, Anika, Ryan, Leanne, Sean and Jacqueline we've survived comprehensive exams, a global pandemic, wars, revolutions, and more nights of revelry than I could remember if I tried. Together we made Hamilton feel like home. Shane, Jerrica, Adam, Akshaya, Matt, Myke, and the rest of the Waterloo crew, to me you will always be family. Physics has been my lifelong passion, made all the more profound by the camaraderie of my colleagues. Anton, Jon, Jesse, Ryan, Addison, Wyatt it has been a distinct joy to find in each of you a kindred spirit.

Mom and Dad, none of this would have been possible without you. Thank you for giving me the courage to follow my heart. I couldn't ask for better parents. Aaron, I can't imagine these last twenty five years without your friendship. Thanks to you I walk through life with the confidence of knowing that somebody will always have my back. I hope you know I'll always have yours. Grandma, Nana, you've been bastions of love and support since before I started to remember, in ways you cannot know, you've helped me weather many storms.

To those mentioned above and those I didn't mention but still love: time will tick forward and the universe will take each of us down our own strange trails. On this journey, I feel lucky to be have become entangled with each of you.

vii

Contents

List of Figures

List of Tables

Declaration of Academic Achievement

Contributed Works

Chapter 2 (Paper I)

J. Lambert, E. S. Sørensen

Estimates of the quantum fisher information in the spin-1 antiferromagnetic Heisenberg model with uniaxial anisotropy

Phys. Rev. B **99**, 045117 (2019)

The project was conceived collaboratively with E. S. Sørensen with all calculations being done by J. Lambert. The main body of the paper was written by J. Lambert with E. S. Sørensen contributing substatially to the introductory chapters. The quantum Monte Carlo calculation was programmed from scratch by J. Lambert.

Chapter 3 (Paper II)

J. Lambert, E. S. Sørensen

Revealing divergent length scales using quantum Fisher information in the Kitaev honeycomb model

Phys. Rev. B **102**, 224401 (2020)

The idea for this paper was conceived by J. Lambert with numerical validation for results coming from E. S. Sørensen. All calculations included were performed by J. Lambert. The paper was written primarily by J. Lambert with input from E. S. Sørensen.

Chapter 4 (Paper III)

J. Lambert, E. S. Sørensen

State Space Geometry of the Spin-1 Antiferromagnetic Heisenberg Chain

arXiv:2209:05005 (Submitted for publication to Phys. Rev. B)

The idea for this paper was conceived by J. Lambert with numerical validation for results coming from E. S. Sørensen. All calculations included were performed by J. Lambert. The paper was written primarily by J. Lambert with input from E. S. Sørensen.

Other Works

Quantum fluctuations inhibit symmetry breaking in the Hamiltonian mean-field model

R. Plestid, J. Lambert

Phys. Rev. E **101** 012136 (2020)

This paper was initiated by R. Plestid who did the original calculation. J. Lambert checked this calculation and discovered an error which qualitatively changed the results of the paper. The introduction and results sections were written by R. Plestid while J. Lambert contributed to the discussion and conclusions of the paper.

Chapter 1

Introduction

> "There is no royal road to geometry."
>
> Euclid

The study of many body systems is the study of fluctuation and correlation. In the classical approach to statistical mechanics, fluctuations arise due to an exchange with the environment of heat or particle number, while correlations arise in the absence of fluctuation. At high temperatures, fluctuations in the position of water molecules are so significant that they are hardly correlated at all, while at low temperatures water organizes into crystal structures so hard that they can split rock. Quantum mechanics introduces novel kinds of fluctuations due to the principle of uncertainty and these fluctuations can, themselves, become correlated through the principle superposition. Electron spins might look individually as if they are exhibiting completely random motions, yet these fluctuations belie a deep kind of correlation that we call entanglement. These quantum correlations and fluctuations are the defining features of exotic states of matter, found in the low temperature regimes where quantum effects dominate. They also provide the basis for the technological applications of quantum mechanics. Sensors that can exceed traditional limitations on precision and quantum computers that can surpass classical limits both rely on quantum fluctuations and correlations to function. Leveraging the potential of quantum effects requires us to

1

distinguish them from their thermal analogues. How can we tell whether correlations in a system are from the presence of entanglement or simply the classical tendency to order at low temperature? What makes quantum fluctuations distinct from thermal fluctuations?

In this thesis we approach this challenge from the perspective of information geometry. By quantifying the degree to which two probability distributions are distinguishable from one another in some set of measurements, we can induce a notion of distance. Far from a mathematical abstraction, this notion of distance is, by its very definition, rooted in the outcomes of measurements, thus allowing for quantum fluctuations and correlations to be probed directly. Our interest will be in the study of many body state space, where the full geometry of the space is highly dependent on the choice of parameterization. By choosing judicious submanifolds and directions, we can chart the quantum state space and reveal the rich and varied landscapes induced by strongly correlated phases and quantum critical points.

The remainder of the introduction is divided into three sections. The first is a pedagogical review of the field of quantum information geometry that begins with the classical theory and establishes the connection between quantum geometry and entanglement. The second reviews the spin-1 Heisenberg chain which is of particular relevance for Papers I and III. The final section gives a brief overview of the current state of field, highlighting a number of the key experiments.

1.1   Information Geometry and Entanglement

In this section we first review the concept of quantum entanglement. We then introduce the fundamental concepts in information geometry, beginning with classical information theory. From the Shannon information we derive the metric on the space of classical distributions using the relative entropy. These quantities are then generalized to the quantum case, where their relationship to genuine multipartite entanglement and linear response functions is discussed. We then introduce the quantum variance and the fidelity susceptibility, both of which are manifestations of

quantum information geometry.

1.1.1   Pure States and Mixed States

The study of any many body system begins with identifying the relevant degrees of freedom. These might be the positions and momenta of particles in a gas, or the orientations of the magnetic moments in an insulator. A pure state is one which specifies these degrees of freedom to the highest level allowed by the theory. In classical systems, it is in principle always possible to specify all of the degrees of freedom simultaneously. A classical pure state would then correspond to, for example, a list of positions and momenta for each particle. The experimental intractability of determining exactly each microscopic degree of freedom is then handled by imagining the state of the system to be some mixture of the possible pure states, consistent with the more easily observable macroscopic degrees of freedom. We refer to the space of all possible pure and mixed states as the *state space* of the system. If a classical N-body pure state $\mathcal{S}$ can be represented as a series of positions a momenta $(\vec{r}_{\mathcal{S},1}, ..., \vec{r}_{\mathcal{S},N}, \vec{p}_{\mathcal{S},1}, ...\vec{p}_{\mathcal{S},N})$, then a mixed state can be represented as a probability distribution over all possible pure states $P(\mathcal{S})$. Classical many body mixed states exhibit fluctuations due to two main sources. The first is the constant dynamics induced in the system by exchanges, whether or energy or particles, with the surrounding environment. The second is due to the presence of non-identical copies of the system under study. For example, a one dimensional system of magnetic moments may be physically manifest in a quasi one dimensional material, where each quasi one dimensional chain has its own sets of imperfections. Measurements are then partially distributed according to the variances in the quasi one dimensional chains.

Quantum mechanics differs fundamentally from this classical picture due the uncertainty principle, which constrains our ability to simultaneously specify all of the degrees of freedom. We might specify the position *or* the momentum, the z component of spin *or* the x component, but not both. A quantum pure state is not

3

a specification of each observable's precise value, but is rather a vector $|\psi\rangle$, that tells us how to construct probability distributions for various observables.

Quantum mixed states are probability distributions over the space of pure states, and can be represented by the density matrix,

$$\hat{\rho} = \sum_j p_j |\psi_j\rangle \langle\psi_j| \tag{1.1}$$

So in quantum systems we have the same sources of fluctuation that occur in classical systems, but with the additional fluctuations caused by the uncertainty intrinsic to the pure states themselves. One sometimes refers to the fluctuations induced by classical effects as *incoherent* to emphasize the fact that they are not governed by a single wave function, while quantum fluctuations are termed *coherent*. The quantum state space is the space of all possible mixed states, which include the pure states as the special case where $p_j = \delta_{ij}$ in Eq. 1.1.

Both the classical and quantum state space are *convex* sets. This means that any mixture of pure states is also a valid state of the system. An important difference between the two is that the classical state space is a simplex. That is to say, any classical mixed state is a *unique* mixture of pure states. Imagine, for example, the state space for two coins with variable weighting. For trick coins that always show one outcome or another, the system will results in either HH, HT, TH, or TT with probability 1, and so these are the pure states of the system. If the coins have any other weighting, the state describing the outcome of N trials will be some unique mixture of these pure states. For example, for two completely fair coins (heads or tails equally likely), the distribution would be $p_{HH} = p_{HT} = p_{TH} = p_{TT} = \frac{1}{4}$.

By contrast, quantum mixed states (density matrices) are not unique mixtures of pure states in general. For example, the mixed state of a single qubit corresponding to 50-50 mixture of the spin pointing up or down along the z axis might be equivalently written as,

$$\hat{\rho}_0 = \frac{1}{2} |+_z\rangle \langle+_z| + \frac{1}{2} |-_z\rangle \langle-_z| \tag{1.2a}$$

$$\hat{\rho}_0 = \frac{1}{2} |+_x\rangle \langle+_x| + \frac{1}{2} |-_x\rangle \langle-_x| \tag{1.2b}$$

where $|\pm_\alpha\rangle$ are the eigenstates of the Pauli operator σ_α. In fact there are infinitely many ways to write the state $\hat{\rho}_0$ in terms of mixtures of pure states of a single qubit. We can visualize the state space of a single qubit on a Bloch sphere, where the surface of the sphere represents the pure state and the interior represents the mixed states. Geometrically, the non-uniqueness of $\hat{\rho}_0$ can be see by noticing that this state sits at the origin of the Bloch sphere, and can be represented as an equal mixture of any two antipodal points. There is, of course, nothing special about $\hat{\rho}_0$, and the same argument would be true of the mixed state corresponding to mixture $\frac{3}{4}$ spin up to $\frac{1}{4}$ spin down.

There is another important distinction between quantum and classical pure states. Let h^C and h^Q be the vector spaces corresponding to the state of a classical and quantum particle respectively, with only spatial degrees of freedom. The classical state of N particles then lives in the many body state space $H_N^C = \bigoplus_{i=1}^{N} h_i^C$, which is just the direct sum over the individual state spaces. Specifying the many body pure state is equivalent to specifying N single body pure states, for any such system. The state of a quantum system is, by virtue of the Schrödinger equation, $H_N^Q = \bigotimes_{i=1}^{N} h_i^Q$. This means that a generic N body pure state cannot necessarily be decomposed into a pure state on each subsystem. This is the phenomenon of entanglement and we discuss it more in the following section.

1.1.2   Entanglement

Aside from the Heisenberg uncertainty principle, entanglement is the fundamental feature of quantum mechanics. It arises due to the principle of superposition. A general quantum many-body pure state may not be expressible in terms of a pure state on each subsystem. The prototypical example of bi-partite entanglement is the spin singlet,

$$|\psi\rangle = \frac{1}{\sqrt{2}}(|\uparrow_A\downarrow_B\rangle - |\downarrow_A\uparrow_B\rangle), \tag{1.3}$$

The notion of bipartite entanglement can be generalized as follows. Let $|\Psi\rangle$ be an N-body pure state. This state is called *m-producible* if it can be written as a product over M factors, each containing at most m particles. Formally, if we can

write $|\Psi\rangle = \bigotimes_{l=1}^{M} |\psi_l\rangle$ where the states $|\psi_l\rangle$ consist of $N_l \leq m$ particles then $|\Psi\rangle$ is called m-producible. If $|\Psi\rangle$ is m producible but not $(m-1)$-producible, then we say the $|\Psi\rangle$ is m-partite entangled. This definition can be generalized to mixed states. The producibility of the state is convex under mixture. That is to say, a mixture for k-producible states may be m-producible where $m < k$.

1.1.3   Classical Information Geometry

Shannon Information and Relative Entropy

One possible mathematical notion of information quantifies the information learned by observing a random process. Events which are deterministic, such a flipping a trick coin with both sides heads, tell us nothing new about the world, and hence observing such an outcome conveys no new information. Conversely, a fair coin is fair precisely because neither party participating in the toss has any clue what it will be; observing the outcome of the toss conveys some quantity of information to the observer. From this perspective, information goes hand in hand with unpredictability, with less predictable processes (i.e. those with higher variance), conveying more information than low variance processes. In 1948, Claude Shannon introduced the modern formula which quantifies this intuition [1],

$$S_b(P) = -\sum_j p_j \log_b(p_j) \tag{1.4}$$

where $P = \{p_1, \ldots, p_N\}$ is the probability that some random process X will have outcome x_j. The base of the logarithm is a free choice and sets the units of information. The two choices that we will apply here are *bits* ($b = 2$) and *nats* ($b = e$). Often in this thesis we will regard the probabilities p_j as depending on some parameter λ. In this case we might write, for a discrete sample space $p_j = p_j(x_j|\lambda)$. The quantity $p_j(x_j|\lambda)$ is conventionally read as the probability of the event x_j given the value of the parameter λ. We might equivalently read it as the likelihood of the parameter have the value λ given the observation of the outcome x_j. In this context one sometimes write $L(\lambda|x_j)$. In the following discussion we will continue to use the notion $p_j(x_j|\lambda)$,

6

but we refer to it interchangeably as the likelihood or the probability. In parameter estimation problems, one tends to be interested in the likelihood that the parameter λ assumes a particular value given a certain observed frequency of outcomes. One description of Eq. 1.4 that will prove useful later is to think of it as the expected value of the negative *log-likelihood*, $-\log_2(p_j)$.

Shannon's information formula may seem somewhat arbitrary but it has a number of properties that make it unique among measures of information. We list the key properties in App. A. Pure classical states, those whose distributions are characterized by a single outcome occurring with total certainty, have zero Shannon information.

In physics, Eq. 1.4 was known a century earlier in a specialized form, as the Boltzmann's entropy, which gives the entropy of W equally likely microstates corresponding to a given macrostate,

$$S = k_B \log(W), \tag{1.5}$$

Deriving this expression from Eq. 1.4 is easily done by substituting $p_j = \frac{1}{W}$ for all j. We can see that Shannon information is simply a natural generalization of the concept of entropy. For this reason we will use the terms entropy and information interchangeably from now on.

It is now natural for us to ask how distinguishable two probability distributions P and Q are in terms of their information content. To this end we introduce the *relative entropy* [2],

$$S_b(P||Q) = \sum_{j=1}^{N} p_j \log_b \left(\frac{p_j}{q_j} \right) \tag{1.6}$$

Amongst other things, it bounds the probability, E, that we would obtain frequencies corresponding to a distribution, P, when sampling $\mathcal{N}$ times from the distribution Q,

$$E \leq (\mathcal{N} + 1)^N b^{-\mathcal{N} S_b(P|Q)} \tag{1.7}$$

This result is called Sanov's theorem [3].

For example, one might ask how probable it is that a trick coin, $(q_H = 1, q_T = 0)$ flipped $\mathcal{N}$ times would be mistaken for a fair coin $(p_H = p_T = \frac{1}{2})$. In the limit of a

7

large number of trials, a fair coin would gives heads half of the time. The relative entropy, $S(P||Q) \to \infty$ in the limit $q_H \to 1$, and so E, the probability of mistaking the trick coin for a fair coin is zero. By contrast, the relatively entropy $S(Q||P) = 1$, and so the probability that a fair coin would be mistaken for a trick coin is bounded above by a decaying exponential as $\mathcal{N}$ goes to infinity.

Classical Fisher Information Metric

The notion of distinguishability captured by the relative entropy cannot be interpreted as a distance in and of itself because it is not symmetrical in the distributions P and Q. Despite this, we can use it to construct a notion of distance by considering the relative entropy between infinitesimally close distributions P and $P + \mathrm{d}P$ [4],

$$S(P||P + \mathrm{d}P) = \sum_i p_i \ln\left(\frac{p_i}{p_i + \mathrm{d}p_i}\right) \approx \frac{1}{2}\sum_i \frac{\mathrm{d}p_i \mathrm{d}p_i}{p_i} \tag{1.8}$$

At leading order, this quantity is symmetric, and we can imagine that it is, in some sense, the square of the distance element,

$$\mathrm{d}s^2 = \frac{1}{4}\sum_{i=1}^{N} \frac{\mathrm{d}p^i \mathrm{d}p^i}{p^i} \tag{1.9}$$

The normalization of $\frac{1}{4}$ has been chosen for reasons which will become apparent in a moment. From the expression for the distance element we can read off the metric,

$$F_{ij} = \frac{1}{4}\frac{\delta_{ij}}{p_i}. \tag{1.10}$$

We've chosen to label the metric F rather than with the conventional g because it's earliest appearance in the statistics literature is due to the work of Ronald Fisher [5, 6]. From now on we refer to this metric as the *classical Fisher information metric* (CFIM). To interpret this metric we can perform a change of variables,

$$x_i = \sqrt{p_i}, \quad \mathrm{d}x_i = \frac{\mathrm{d}p_i}{2\sqrt{p_i}} \tag{1.11}$$

in terms of which the line element now reads,

$$\mathrm{d}s^2 = \sum_{i=1}^{N} \mathrm{d}x_i \mathrm{d}x_i \tag{1.12}$$

with the constraint,

$$\sum_{i=1}^{N} p_i = \sum_{i=1}^{N} x_i^2 = 1. \tag{1.13}$$

Taken together, Eqs. 1.12 and 1.13 give the geometry of a unit sphere. In particular, the space of probability distributions is given by the positive hyper-octant (due to the restriction that all probabilities be positive). The distance between two distributions as measured by the CFIM is then,

$$D_{\mathrm{B}}(P, Q) = \cos^{-1}\left(\sum_{i=1}^{N} \sqrt{p_i q_i} \right). \tag{1.14}$$

which is the angle that subtends the arc of the great circle joining P and Q. This notion of distance on the state space is called the *Bhattacharyya distance* [7] and the summation inside the inverse cosine is called *classical fidelity*. Just as in standard Euclidean space, there are many other notions of distance that might be defined on the space of probability distributions. The Bhattacharya distance is special not only because of its connection to the distinguishability of distributions, but because it is the only metric on the space of probability distributions that is both Riemannian and monotone [8]. Monotone simple means that for any stochastic matrix T, the distance obeys the inequality $D(TP, TQ) \leq D(P, Q)$. In words: distributions become closer under coarse graining.

It is clear from Eq. 1.14 that pure states are always maximally separate from one another at a distance of $\frac{\pi}{2}$. This is because a pure state is in one particular configuration with absolute certainty, that is $p_i = \delta_{ij}$. This is due to the fact that the classical state space is a simplex as discussed in Sec. 1.1.1

It will usually be the case that we are interested in some subset of all possible distributions parameterized by an n-dimensional parameter $\vec{\lambda} \in \mathbb{R}^n$. In these new

coordinates we may transform the metric,

$$F_{ab} = \frac{1}{4} \sum_{i,j} \frac{\partial p^i}{\partial \lambda^a} \frac{\partial p^j}{\partial \lambda^b} F_{ij} \tag{1.15}$$

Using our definition from Eq. 1.10 we can write CFIM as,

$$F_{ab} = \frac{1}{4} \sum_j \frac{1}{p(x_j|\vec{\lambda})} \frac{\partial p(x_j|\vec{\lambda})}{\partial \lambda_a} \frac{\partial p(x_j|\vec{\lambda})}{\partial \lambda_b} \tag{1.16a}$$

$$F_{ab} = \frac{1}{4} \int_\Omega \mathrm{d}x \frac{1}{p(x|\vec{\lambda})} \frac{\partial p(x|\vec{\lambda})}{\partial \lambda_a} \frac{\partial p(x|\vec{\lambda})}{\partial \lambda_b}. \tag{1.16b}$$

The set of functions $p(x|\vec{\lambda})$ is often called a *statistical model* [4]. From now on when we refer to the CFIM (unless otherwise specified) we mean these two equations.

Before moving on, we introduce two equivalent forms of the CFIM that will be useful in our generalization to the quantum case. First notice that we may write,

$$F_{ij} = -\frac{1}{4} \partial_i \partial_j S(P) \tag{1.17}$$

The definition in Eq. 1.17 makes clear that this metric captures the shape of the Shannon information as a function of the probabilities. Second, we may write Eq. 1.16b as,

$$F_{ab} = \frac{1}{4} \int_\Omega \mathrm{d}x \, p \frac{\partial \ln p}{\partial \lambda_a} \frac{\partial \ln p}{\partial \lambda_b}. \tag{1.18}$$

This expression is the covariance between logarithmic derivatives of the probability density functions. One might expect that we would need to subtract off the expected value of the logarithmic derivative, but it is easy to see that this zero. Earlier we said that the Shannon information is the expected value of the negative log-likelihood. We can interpret the negative log-likelihood of an event as the information learned when that event occurs, and the logarithmic derivatives as tangent vectors on this landscape of information. From this perspective, Eq. 1.18 can be understood as an inner product on the tangent space, which is precisely how we are accustomed to defining the components of the metric tensor in differential geometry.

Cramér-Rao Bound

The entries of the CFIM quantify the amount of knowledge that we can learn about the parameters $\vec{\lambda}$ that model the random process. If $\hat{\lambda}_\mu$ are unbiased ($\langle \hat{\lambda} \rangle_\mu = \lambda_\mu$) estimators for the model parameters then the covariance in the estimators obeys the Cramér-Rao bound [9],

$$\mathrm{Cov}(\hat{\lambda}_\mu, \hat{\lambda}_\nu) \geq \frac{1}{F_{\mu\nu}} \tag{1.19}$$

where $\mathrm{Cov}(\hat{\lambda}_\mu, \hat{\lambda}_\nu) = \langle \hat{\lambda}_\mu \hat{\lambda}_\nu \rangle - \langle \hat{\lambda}_\mu \rangle \langle \hat{\lambda}_\nu \rangle$ This bound quantifies the extent to which we might learn about the parameters of our statistical model and represents a kind of classical uncertainty principle. We won't reproduce a general proof of the Cramér bound here, but it is easy to derive for the case of one dimensional parameter working in the representation of a continuous sample space.

By construction,

$$\int \mathrm{d}x \hat{\lambda}(x) p(x|\lambda) \mathrm{d}x = \lambda \tag{1.20}$$

Differentiating both sides with respect to λ gives,

$$\int \mathrm{d}x \hat{\lambda}(x) p(x|\lambda) \left(\frac{1}{p(x|\lambda)} \partial_\lambda p(x|\lambda) \right) = 1 \tag{1.21}$$

Now we notice that the left hand side of the above equation is just the covariance of the estimator with the logarithmic derivative of the probability. By the Cauchy-Schwarz inequality, we have,

$$\mathrm{Cov}\left(\hat{\lambda}, \partial_\lambda \ln(p(x|\lambda)) \right) \leq \mathrm{Var}(\hat{\lambda}) \mathrm{Var}(\partial_\lambda(\ln(p(x|\lambda)))) \tag{1.22}$$

we can now use Eq. 1.21 and the fact that the variance of the logarithmic derivative is the one parameter CFIM (see Eq. 1.16b), to write,

$$\mathrm{Var}(\hat{\lambda}) \geq \frac{1}{F_{\lambda\lambda}} \tag{1.23}$$

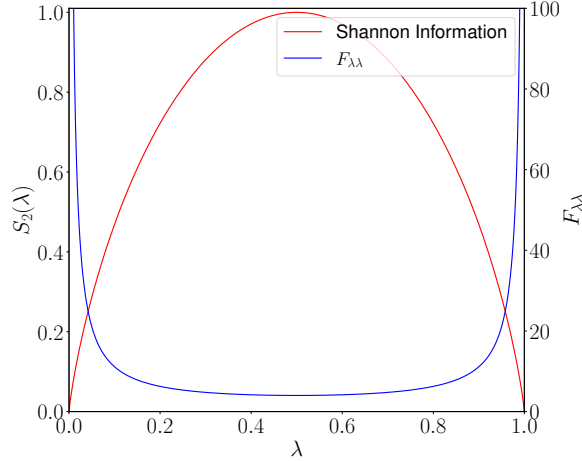which is the diagonal part of Eq. 1.19.

11

Figure 1.1: Shannon information (red) in bits and Fisher information (blue) for a coin toss with $p_H = \lambda$. The fair coin with $\lambda = 0.5$ is simultaneously the least predictable (high Shannon information), and the hardest to distinguish from its neighbours (low Fisher information).

Information Geometry of a Coin Toss

To illustrate the relationship between Shannon information and Fisher information we can consider the case of a weighted coin, with probability of heads $p_H = \lambda$. The Shannon information (red) (computed from Eq. 1.4) and Fisher information (computed from Eq. 1.16a) (blue) are given in Fig. 1.1. We can see that in a certain sense the Fisher information and the Shannon information are complimentary to one another, with the least predictable distributions have the highest Shannon information but the least Fisher information. Where Shannon information quantifies how unpredictable a distribution might be, Fisher information quantifies how distinguishable one random process is from another.

1.1.4   Quantum Information Geometry

Quantum mechanics is built on the principles of uncertainty and superposition. The former guarantees that even pure quantum states will exhibit fluctuations in complimentary degrees of freedom (such as orthogonal spin components), while the latter

allows for those fluctuating degrees of freedom to exhibit correlations. Together these quantum fluctuations and correlations are responsible for a rich variety of low temperature phases. In this section we develop an understanding of these two principles from the perspective of quantum information geometry. Our discussion begins with the von Neumann entropy and the associated entropy of entanglement. We then apply the notion of distinguishability to the case of pure quantum states, and explain how this geometry can be used to quantify the presence of both quantum fluctuations and correlations.

Roughly speaking, passing from classical to quantum mechanics involves replacing the probability distribution with the density matrix, and the integral with the trace. Schematically,

$$p(\vec{\lambda}) \to \hat{\rho}(\vec{\lambda}), \qquad \int \mathrm{d}x(\cdot) \to \mathrm{Tr}\{\cdot\}, \tag{1.24}$$

where,

$$\hat{\rho}(\vec{\lambda}) = \sum_j p_j \left| j \right\rangle \left\langle j \right|. \tag{1.25}$$

As we will see this process is straightforward for the Shannon information but introduces ambiguities when generalizing the CFIM.

von Neumann and Entanglement Entropy

By performing the classical-quantum mapping in Eq. 1.24 we can immediately obtain the von Neumann entropy [10][1],

$$\mathcal{S}_{\mathrm{vN}} = -\mathrm{Tr}\{\hat{\rho}\log_2(\hat{\rho})\}. \tag{1.26}$$

Like the Shannon information, the von Neumann entropy is zero for pure states, as can be seen by taking $p_j = \delta_{ij}$ in Eq. 1.25. For a Gibbs distribution at inverse temperature β,

$$\hat{\rho}_{\mathrm{Gibbs}} = \frac{e^{-\beta\hat{H}}}{Z}, \tag{1.27}$$

---

[1]As with the Shannon entropy we might in general use any base we like for the logarithm, our choice of 2 is just for convenience.

where,

$$Z = \text{Tr}\left\{e^{-\beta \hat{H}}\right\}, \tag{1.28}$$

the von Neumann entropy reduces to the Boltzmann entropy in the limit $\beta \to 0$. This limit is non-trivial, and in the intermediate region quantum effects can still be relevant particularly at low temperatures.

So far there is nothing quantum about any of this save for the formalism itself. We see that classical information theory lives inside quantum information theory as a special case, provided all of the relevant quantities commute with one another. There is, however, a crucial difference between classical and quantum pure states for many body systems. In classical statistical mechanics a many body pure state is pure all the way down. Specifying complete knowledge of the state of N particles, requires specifying completely the states of each particle individually as we saw in Sec. 1.1.1.

Quantum pure states are specified by a wave function, rather than by an exact account of every classical degree of freedom. Quantities that are complimentary, such as the orthogonal orientations of a spin, are bound to exhibit fluctuations even in pure quantum states. Due to the principle of superposition, these states may be entangled, as we saw in Sec. 1.1.2. If a quantum pure state is entangled, the state of its partitions will be mixed, and hence will exhibit a non-zero von Neumann entropy.

To be precise, A general N body pure state $|\Psi\rangle$ may be divided into partitions A and B, with one partition traced out,

$$\hat{\rho}_A = \text{Tr}_B\{|\Psi\rangle \langle\Psi|\} \tag{1.29}$$

The resulting state $\hat{\rho}_A$ will be pure provided that $|\Psi\rangle$ can be written as a product, $|\Psi\rangle = |\Phi_A\rangle |\Phi_B\rangle$. Taking the von Neumann entropy of the state $\hat{\rho}_A$ will give zero as long as the product form holds. Otherwise, the von Neumann entropy of the subsystem,

$$\mathcal{S}_A = \mathcal{S}_{\text{vN}}\{\hat{\rho}_A\} = -\text{Tr}\{\hat{\rho}_A \log_2(\hat{\rho}_A)\} \tag{1.30}$$

will be non-zero and will thus provide a measure of the uncertainty introduced by discarding subsystem B, and hence the amount of information stored in the entangle-

14

ment between the two subsystems. For this reason, Eq. 1.30 is called *entanglement entropy* (EE). It doesn't matter which partition we choose to keep, since $\mathcal{S}_A = \mathcal{S}_B$.

We can read Eq. 1.30 as the expectation value of the operator $\hat{H}_A = -\log_2(\hat{\rho}_A)$ which is termed the *entanglement Hamiltonian*. It is often sufficient to consider the lowest eigenvalue of the entanglement Hamiltonian when attempting to detect the presence of a critical point. Nonetheless, the spectrum of $\hat{H}_A$ exhibits a characteristic doubling when ψ is in a so called symmetric protected topological (SPT) phase [11].

Extending this concept to large many body systems has proven enormously fruitful [12]. The scaling of the von Neumann entropy with subsystem size, along with the spectrum of $\ln(\hat{\rho})$ have found extensive application in the classification of many-body quantum phases [11] and critical points [13]. The entanglement entropy can also be used to detect and classify topological phases of matter via a negative, subleading contribution to its scaling with subsystem size [14]. This *topological entanglement entropy* has become a major fixture of the study of topological phases from a theoretical perspective. For a more thorough review of the EE one may consult [15].

While entanglement entropy has seen vast theoretical application in condensed matter systems, its utility as an experimental probe is limited for two reasons. First, the entanglement entropy cannot detect the presence of entanglement in mixed states, since the interpretation of the subsystem von Neumann entropy as the entropy of entanglement relies on the assumption that the total state is pure. Since we are often interested in the entanglement at low but non-zero temperatures, the entanglement entropy is often not applicable. Second, measuring the entanglement entropy involves performing a full tomography on the state of the system, an intractable task for macroscopic materials.

Quantum Fisher Information Metric

The principle of superposition means that there are two ways for quantum states to be distinguishable from one another. Unlike classical states which are mixtures of pure states that are all maximally separated (in the sense of the Bhattacharyya distance), quantum states may be in either mixtures or superpositions of pure states.

In the case of the latter, the natural generalization of the Bhattacharyya distance is to replace the classical fidelity with the quantum fidelity, which is just the inner product between states [16],

$$D_{\text{QB}}(\psi_1, \psi_2) = \cos^{-1}\left(|\langle\psi_1|\psi_2\rangle|\right) \tag{1.31}$$

We can now determine the metric for the space of pure state by looking at the square of the distance between a state ψ and an infinitesimally displaced state $\psi + \text{d}\psi$,

$$|\psi\rangle = \sum_j \sqrt{c_j} e^{i\phi_j} |j\rangle \tag{1.32a}$$

$$|\psi\rangle + |\text{d}\psi\rangle = \sum_j \sqrt{c_j + \text{d}c_j} e^{i(\phi_j + \text{d}\phi_j)} |j\rangle \tag{1.32b}$$

Expanding $D_{QB}(\psi, \psi + \text{d}\psi)^2$ gives the line element [17, 18],

$$\text{d}s_{\text{FS}}^2 = \frac{1}{4} \sum_j \frac{\text{d}p_j^2}{p_j} + \left(\sum_j p_j(\text{d}\phi_j)^2 - \left(\sum_j p_j \text{d}\phi_j\right)^2\right) \tag{1.33}$$

This is the metric developed by Fubini [19] and Study [20], over two decades before the development of the modern quantum theory. It gives the line element on the complex projective space that is employed as the space of pure quantum states.

Central to the results in Papers II and III is the fact that, for a unitary path parameterized by λ and generated by the Hermitian operator $\hat{\Lambda}$ according to the Schrödinger equation,

$$\partial_\lambda |\psi\rangle = -i\hat{\Lambda} |\psi\rangle \tag{1.34}$$

the metric corresponding to this line element is given by the connected covariance,

$$\mathcal{F}_{\mu\nu}^{\text{unitary}} = 4\text{Cov}(\hat{\Lambda}_\mu, \hat{\Lambda}_\nu) \tag{1.35}$$

where $\text{Cov}(A, B) = \langle AB\rangle - \langle A\rangle\langle B\rangle$. Notice the similarity with the expression for the CFIM in Eq. 1.18, where we interpreted the covariance in the logarithmic derivatives as a dot product between tangent vectors on the space of information. Deriving Eq. 1.35 from Eq. 1.33 can be done by representing $|\psi\rangle$ in the eigenbasis of the

16

operator $\hat{\Lambda}$. We then write the change in the overall phase as $\mathrm{d}\phi_j \left| j \right\rangle = \mathrm{d}\lambda \hat{\Lambda} \left| j \right\rangle$ and consequently $(\mathrm{d}\phi)^2 \left| j \right\rangle = \mathrm{d}\lambda^2 \hat{\Lambda}^2 \left| j \right\rangle$. By assuming that the path is unitary, we can ignore the change in the amplitude of each state $\mathrm{d}c_j$, and hence the first term in Eq. 1.33 is zero. Here we see the same form appearing, with the generators of the transformation playing the role of the tangent vectors.

Accounting for the case of mixed states can be done through the mapping Eq. 1.24, however we immediately encounter a problem. If the parameterization changes the eigenstates of the density matrix, the ordering of the operators under the trace becomes unclear, since $[\hat{\rho}, \partial_\lambda \hat{\rho}] \neq 0$. To resolve this issue, we can introduce a super-operator [17, 21],

$$\mathcal{L}_\rho^{-1}(\hat{O}) = \frac{1}{2}(\hat{\rho}\hat{O} + \hat{O}\hat{\rho}). \tag{1.36}$$

The inverse of this super operator may be written in the eigenbasis of the density matrix as,

$$\mathcal{L}_\rho(\hat{O}) = \sum_{j,k} \frac{2}{p_j + p_k} O_{jk} \left| j \right\rangle \left\langle k \right| \tag{1.37}$$

with the sum running only over terms with $p_j + p_k > 0$. Applying the inverse to the derivative of the density matrix,

$$\mathcal{L}_\rho \left(\frac{\partial \hat{\rho}}{\partial \lambda} \right) \tag{1.38}$$

gives the *symmetric logarithmic derivative* (SLD). Using this expression as the quantum generalization of the logarithmic derivative allows us to generalize the form of the CFIM in Eq. 1.18 to the quantum Fisher information metric (QFIM) as,

$$\mathcal{F}_{\mu\nu} = \mathrm{Tr}\{\hat{\rho}\mathcal{L}_{\hat{\rho}}(\partial_\mu\hat{\rho})\mathcal{L}_{\hat{\rho}}(\partial_\nu\hat{\rho})\} \tag{1.39}$$

It is not at all obvious that the *symmetric logarithmic derivative* is the correct way to handle the ordering ambiguity induced by the non-commutativity of $\hat{\rho}$ with its derivative. In fact, the QFIM stated in Eq. 1.39 is just one of an infinite family of generalizations of the CFIM, each corresponding to a different way of handling the ordering ambiguity. These metrics were first classified by Morozova and Čencov [22], who found that each possible choice corresponds to an operator monotone function.

17

QFIM	monotone function
Symmetric logarithmic derivative	$\frac{1+x}{2}$
Bogoliubov-Kubo-Mori	$\frac{x-1}{\log(x)}$
right logarithmic derivative	x
left logarithmic derivative	1
Skew information ($\alpha = 1$)	$\frac{(\sqrt{x}+1)^2}{4}$

Table 1.1: A partial reproduction of the table in [23] listing several different forms the QFIM along with the associated monotone function.

More generally we might express the ambiguity in the operator ordering using the superoperators [23],

$$R_{\hat{\rho}}(\hat{O}) = \hat{O}\hat{\rho} \tag{1.40a}$$

$$L_{\hat{\rho}}(\hat{O}) = \hat{\rho}\hat{O} \tag{1.40b}$$

$$(\mathcal{L}_{\hat{\rho}}^f)^{-1} = f(L_{\hat{\rho}}R_{\hat{\rho}}^{-1})R_{\hat{\rho}} \tag{1.40c}$$

where f is the aforementioned operator monotone function. The most general QFIM is then given by,

$$\mathcal{F}_{\mu\nu} = \text{Tr}\{\hat{\rho}\mathcal{L}_{\hat{\rho}}^f(\partial_\mu\hat{\rho})\mathcal{L}_{\hat{\rho}}^f(\partial_\nu\hat{\rho})\} \tag{1.41}$$

where the definition in Eq. 1.39 is recovered for the choice

$$f = \frac{1+x}{2} \tag{1.42}$$

There are many other possible choices (we list several in Tab. 1.1) , but the QFIM is distinguished by the fact that it finds the maximal distance between states, and is, in this sense, unique [4]. We will return to the more general definition of the QFIM when we discuss the quantum variance. For the remainder of this section we will continue to work with the SLD form of the QFIM.

In general, the QFIM can be broken into two components, one for the part of the parameterization that changes the eigenvalues (non-unitary), and one for the part of

the parameterization that changes the eigenstates (unitary),

$$\mathcal{F}_{\mu\nu} = \mathcal{F}_{\mu\nu}^{\text{non-unitary}} + \mathcal{F}_{\mu\nu}^{\text{unitary}} \tag{1.43}$$

The non-unitary component,

$$\mathcal{F}_{\mu\nu}^{\text{non-unitary}} = \frac{1}{4} \sum_j \frac{1}{p_j} \partial_\mu p_j \partial_\nu p_j \tag{1.44}$$

is just the CFIM recast in the quantum formalism. In the same way that von Neumann entropy re expresses Shannon information in the mathematical language of quantum mechanics, so too does the non-unitary QFIM re-express the CFIM. It can be written using the same form of the CFIM given in Eq. 1.17

Alternatively, we may consider the unitary transformation generated by a Hermitian operator $\hat{\Lambda}_\mu$ according to the von Neumann equation,

$$\partial_\mu \hat{\rho} = i \left[\hat{\rho}, \hat{\Lambda}_\mu \right], \tag{1.45}$$

where $\partial_\mu \equiv \partial_{\lambda_\mu}$. In this case the QFIM is given by [17],

$$\mathcal{F}_{\mu\nu}^{\text{unitary}} = 2 \sum_{j,k} \frac{(p_j - p_k)^2}{p_j + p_k} [\Lambda_\mu]_{jk} [\Lambda_\nu]_{kj}^* \tag{1.46}$$

The above expression has no classical analogue. It emerges specifically due to the non-commutativity of quantum observables. Considering the fact that the QFIM quantifies the degree of distinguishability along the path generated by the hermitian operator $\hat{\Lambda}_\mu$, it is not surprising that the unitary component of QFI has a convenient representation in terms of the dissipative part of the linear response [24],

$$\mathcal{F}_{\mu\nu}^{\text{unitary}} = \frac{4}{\pi} \int_0^\infty \mathrm{d}\omega \tanh\left(\frac{\omega}{2T}\right) \chi''_{\mu\nu}(\omega). \tag{1.47}$$

where,

$$\chi(\omega) = \int_0^\infty \mathrm{d}t e^{-i\omega t} \operatorname{Tr}\left\{ \hat{\rho} \left[\hat{\Lambda}_\mu(t), \hat{\Lambda}_\nu \right] \right\}. \tag{1.48}$$

Analogous formulas can be shown to hold for all of the QFIM's (that is, for any choice of monotone function f. The general relationship is given by,

$$\mathcal{F}_{\mu\nu}^{\text{unitary}}\{f\} = \frac{2}{\pi} \int_0^\infty \mathrm{d}\omega \frac{1 - e^{-\beta\omega}}{f(e^{-\beta\omega})} \chi''_{\mu\nu}. \tag{1.49}$$

If we consider the state $\hat{\rho}$ to be the Gibbs state in Eq. 1.27 (as we do in Paper I), the zero temperature limit recovers the pure state definition in Eq. 1.35, with different choices of f causing us to replace the factor of 4 with some other number, A. Consistent with our understanding of the SLD QFIM as the maximal choice, the value of A for other choice of f will always be bounded by $0 < A < 4$ [25].

The SLD QFIM can be used to define the Bures distance between mixed states in analogy with Eq. 1.31 [26],

$$D_{\text{Bures}}(\hat{\rho}_1, \hat{\rho}_2) = \cos^{-1}\left(\sqrt{F(\hat{\rho}_1, \hat{\rho}_2)} \right), \tag{1.50}$$

where

$$F(\hat{\rho}_1, \hat{\rho}_2) = \text{Tr}\left(\sqrt{\sqrt{\hat{\rho}_1}\hat{\rho}_2\sqrt{\hat{\rho}_1}} \right)^2 \tag{1.51}$$

is the Uhlmann fidelity [27]. The above expression can be interpreted as the transition amplitude between mixed states in exactly the same way as the quantum fidelity can be interpreted as the transition amplitude between pure states. Taking the SLD QFIM for granted, the Bures distance is the broadest generalization of Riemannian distance on the quantum state space.

The Cramér-Rao bound can be generalized to the quantum case, with the covariance of the estimator for the underlying parameters given by,

$$\text{Var}(\hat{\lambda}_\mu) \geq \frac{1}{\sqrt{\mathcal{F}_{\mu\mu}}} \tag{1.52}$$

where $\hat{\lambda}_\mu$ is the estimator corresponding to parameter λ in analogy with the previous section. The presence of entanglement allows for the QFIM to be greater than the CFIM, and thus for quantum sensors to exceed the bounds of classical measurement precision [28].

Geometry and Entanglement

In Sec. 1.1.4 the von Neuamnn entropy of a subsystem (i.e. the entanglement entropy) was introduced as a measure of entanglement between the subsystem and its complement. This notion of entanglement was restricted to pure states, and required

20

the laborious process of full state tomography to be accessed in experiment. Another limitation is that the entanglement entropy is a measure of the bi-partite entanglement between the subsystem and its compliment. Information about the genuine multipartite entanglement must be inferred either from scaling laws [29], or features of the spectrum of the entanglement Hamiltonian [11].

The trace of the QFIM can be used to introduce bounds on the genuine multipartite entanglement of a spin system for particular choices of the generators Λ_μ. In particular, for a many body spin system, the following generator can be defined,

$$\Lambda_{\hat{n}_r} = \sum_{r=1}^{N} \hat{n}_r \cdot \vec{S}_r \tag{1.53}$$

where $\hat{n}_r$ is a site dependent unit vector,

$$\hat{n}_r = (\cos(\theta_r)\sin(\phi_r), \sin(\theta_r)\sin(\phi_r), \cos(\phi_r)) \tag{1.54}$$

In general we are free to choose these relative orientations however we like. Once the orientations of the unit vectors are set, we may define two more operators. Labelling the initial generator Λ_3, (whatever its local orientations) and defined the orientation on each site as $\tilde{S}^z$, we may define the operators Λ_1 and Λ_2 as the operators with the orientations on each site set to $\tilde{S}^x$ and $\tilde{S}^y$. Now we can consider three orthogonal paths in state space generated by the operators Λ_μ, and consider the corresponding unitary QFIM, $\mathcal{F}_{\mu\nu}$ (we drop the superscript and work from now on only with the unitary component). The trace of the QFIM density obeys the bound [30],

$$\bar{f} := \frac{1}{3N}\operatorname{Tr}(\mathcal{F}) \geq \frac{2}{3}m \tag{1.55}$$

for a state that is $(m+1)$-partite entanglement. Each diagonal entry of the QFIM can also be used independently as a probe of entanglement via the bound [30],

$$f_{\mu\mu} := \frac{1}{N}\mathcal{F}_{\mu\mu} \geq m \tag{1.56}$$

In neutron scattering experiments this bound needs to be normalized by an additional factor [31, 32], so we take the definition of the QFIM in Eq. 1.55 to be,

$$\mathcal{F}_{\mu\nu} = \frac{\mathcal{F}_{\mu\nu}^{\text{unitary}}}{12S^2}. \tag{1.57}$$

21

In Paper III we include this normalized bound in our study of the $S = 1$ Heisenberg chain.

The bounds above are not perfect detectors of multipartite entanglement. Strictly speaking these bounds are only true when m is a divisor of the system size. The studies conducted in this thesis are always done for large systems. In particular, Paper II and Paper III concern systems that are effectively in the thermodynamic limit. Consequently we assume that m is always a divisor of N. When a state is m partite entanglement and m is equal to or greater than $\frac{N}{2}$, the bounds given above can be saturated from below by separable states, as we will see in Sec. 1.1.7.

The QFIM, coupled with its representation in terms of the dynamical structure factor, thus allows us a direct experimental probe of the genuine multipartite entanglement of the spin degrees of freedom. Whether or not entanglement is actually detected depends sensitively on the choice of Λ_1, as we will see. This bound in Eq. 1.55 coupled with Eq. 1.47, allow for the experimental witnessing of genuine multipartite entanglement even up to finite temperature.

One expects that the genuine multipartite entanglement will decrease monotonically as a function of the temperature. In gapped systems, there is a low temperature plateau where the gap protects the multipartite entanglement [33]. In Paper I, we apply the fluctuation-dissipation theorem to re-express Eq. 1.47 in terms of the dynamical structure factor. We then apply the single mode approximation to the spin-1 antiferromagnetic Heisenberg chain and demonstrated the finite temperature plateau in the genuine multipartite entanglement. Our application of the single mode approximation allowed us to estimate the QFI without the need for analytic continuation to determine the full structure factor.

Another key result of Paper I is the witnessing of entanglement in a phase characterized by hidden order. The spin-1 Heisenberg chain manifests short range entanglement that is protected provided that certain symmetries of the Hamiltonian are respected [34]. For this reason it is considered a symmetry protected topological (SPT) phase. Despite the fact that the ground state magnetization is zero in the bulk, and hence exhibits no traditional order, the presence of this robust short range entanglement is indicative of hidden order. The QFI can detect this hidden order

22

directly by measuring the entanglement.

The QFIM has also been studied for non-local generators. In particular, in [35], the topologically distinct phases of the Kitaev wire were found to exhibit super-extensive scaling of the QFIM generated by operators corresponding to string order.

1.1.5   Manifolds in State Space

For many body systems, the space of possible parameterizations approaches infinity in the thermodynamic limit. To gain understanding of such a vast space, demands a judicious choice of parameterization. While there are many interesting choices to consider (see Sec. 1.3), we here present a parameterization of the state space that allows us to make a connection between entanglement and curvature. This is the key result of Paper III, and in this section we develop the basis for that result using the formalism discussed in the preceding sections.

First notice that for any choice of parameterization, the QFIM can be decomposed as follows [36],

$$\mathcal{F}_{\mu\nu} = g_{\mu\nu} + i\Gamma_{\mu\nu}, \tag{1.58}$$

where $g_{\mu\nu}$ is real and symmetric, and is hereafter referred to as the *quantum metric*. $\Gamma_{\mu\nu}$ is anti-symmetric, and is know as the *Berry curvature* [37]. This decomposition is different from that adopted in Eq. 1.43. In general, the non-unitary component of the QFIM will contribute only to the real symmetric part of the manifold, while the unitary component will contribute to both g and Γ. The quantum metric can be used to compute the volume of a manifold $\mathcal{M}$ via the formula,

$$V = \int_{\mathcal{M}} \sqrt{\det(g)} \mathrm{d}V. \tag{1.59}$$

We now introduce a special choice of manifold on the state space. Let $|\psi(\gamma; h, \theta, \phi)\rangle$ be the ground state of the Hamiltonian,

$$\mathcal{H} = \hat{H}_0(\gamma) + h\hat{\Lambda}(\theta, \phi) \tag{1.60}$$

where,

$$\hat{\Lambda}(\theta, \phi) = R^{-1}(\theta, \phi) \left(\sum_{r=1}^{N} \hat{n}_r \cdot \vec{S}_r \right) R(\theta, \phi) \tag{1.61}$$

23

and

$$\hat{R}(\theta, \phi) = e^{-i\theta S_r^z} e^{-i\phi S_r^y} \tag{1.62}$$

is the rotation operator. The operator $\hat{H}_0(\gamma)$ is any spin Hamiltonian dependent on the parameter γ (which we could take to be multidimensional).

Using this setup, we now make precise our description of the particular metric used in the entanglement bound in Eq. 1.55. We first take the case of $(\theta, \phi) = (0, 0)$. This operator is labelled as $\Lambda_{\tilde{z}}$ where we use tildes to make a distinction between orientations in the state space and the lab frame coordinates. Now by the two global rotations $(\theta, \phi) = (0, \frac{\pi}{2})$ and $(\theta, \phi) = (\frac{\pi}{2}, \frac{\pi}{2})$ we define two new operators labelled $\hat{\Lambda}_{\tilde{x}}$ and $\hat{\Lambda}_{\tilde{y}}$ respectively. Together, these three operators can be taken as the generators of translations in a three dimensional submanifold of the Hilbert space with coordinates $(\tilde{x}, \tilde{y}, \tilde{z})$ for the case where $h = 0$ in Eq. 1.60. By taking the trace of the associated QFIM, we thus determine the entanglement of the state $|\psi(\gamma; h = 0)\rangle$. Taking the trace of the QFIM allows us to bound the genuine multipartite entanglement in these states as per the bound in Eq. 1.55.

As we discuss in Sec. 1.3, there is a large branch of literature dedicated to explore the quantum metric just in the vicinity of the ground state for operators linear in the spin degrees of freedom. Indeed, such explorations are central results in all three of the papers that constitute Chapters 2, 3, and 4 of this thesis. A major result of Paper III was to extend this notion and to explore the state space locally around the ground state $|\psi(\gamma)\rangle$. This can be done by choosing h to be small but non-zero. This allows us to construct the state space metric in the space of $(\tilde{x}, \tilde{y}, \tilde{z})$ away from the origin (where the ground state sits). It is convenient to switch to spherical coordinates in this space. Rather than talk about $(\tilde{x}, \tilde{y}, \tilde{z})$, we can instead speak in terms of (h, θ, ϕ). The associated generator can be found by taking,

$$\hat{\Lambda}_\mu(h, \theta, \phi) = \partial_\mu \mathcal{H}(\gamma; h, \theta, \phi) \tag{1.63}$$

In practice we will be especially interested in the 2D spheres parameterized by (θ, ϕ) at fixed values of h. The mapping between orientations of the field operator and the state space is depicted schematically in Fig. 1.2.
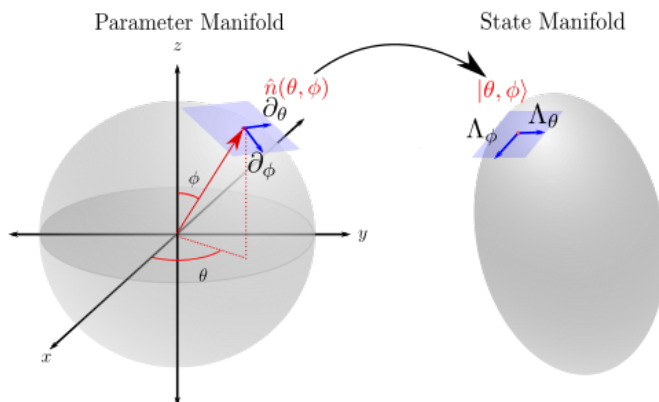
Figure 1.2: A schematic of the 2D manifold generated by the operators $\hat{\Lambda}$ reproduced from Paper III [38].

To understand what this manifold looks like it helps to first consider the case where $H_0 = 0$. Here the space of states parameterized by (h, θ, ϕ) is spherically symmetric, with different points related by the rotation operator defined in Eq. 1.62. Using the covariance form of the QFIM for pure states from Eq. 1.35 we can compute the volume (really the surface area) of this manifold at a fixed value of h,

$$V(h) = 4\pi \left(\frac{2N}{S} \right) h^2. \tag{1.64}$$

This is just the surface area of N spheres with radius $\sqrt{\frac{2}{S}}h$, which is what we would expect given the symmetry of the space and the extensive nature of the generators. Notice that in the classical limit the radius of this sphere will tend to zero, and so the quantum volume for manifolds in the vicinity of a classical state is zero.

It is possible to generalize Eq. 1.64 slightly to the case where $H_0(\gamma)$ is non-zero but still has spherical symmetry. We also make the simplification of taking $\tilde{z}$ to correspond to the staggered magnetization along the z axis. The appendix of Paper III presents the details of the calculation. The result is,

$$V^{\text{spherical}}(\gamma; h) = 4\pi \frac{4}{S^2} h^2 \sqrt{\Xi_{xxyy}(\gamma; h)} \tag{1.65}$$

where,

$$\Xi_{abcd} = \mathcal{A}_{ab}\mathcal{A}_{cd} - \mathcal{A}_{ac}\mathcal{A}_{bd} \tag{1.66}$$

and $\mathcal{A}_{ab}$ is the real part of the correlation matrix,

$$\mathcal{C}^{ab} = \sum_{r_1, r_2} (-1)^{r_1 + r_2} \text{Cov}_{\psi(\theta, \phi)}(\hat{S}_{r_1}^a, \hat{S}_{r_2}^b) \tag{1.67}$$

with $\phi = \pm 1$ and $a, b, c, d \in \{x, y, z\}$ represent the spin components in the lab frame. Different choices of relative orientation would yield different, site dependent, prefactors for the correlation matrix above, and so in general this matrix should be thought of as functionally dependent on the set of local orientations $\hat{n}_r$..

Eq. 1.65 is again the surface area of a sphere, where the radius of this sphere is controlled by the square root of the fluctuations in the directions that are transverse to $\hat{\Lambda}_h$. This appears as a dependence on the x and y correlations only because of the spherical symmetry, which allows us to determine the transverse correlations for any orientation from the correlations along the z axis. The quantum volume in the vicinity of the ground state can then be interpreted as a measure of the degree of fluctuation in the state at the origin.

The curvature of a space can be determined by considering the ratio of the volume of a $d-1$ sphere in $\mathcal{M}$ relative to a $d-1$ sphere in flat space, in the limit of small radius. For a d dimensional manifold $\mathcal{M}$ with Ricci curvature R, the volume ratio for $d-1$ sphere of radius ϵ exhibits the behaviour,

$$v = \frac{V_\mathcal{M}}{V_\text{flat}} = 1 - \frac{1}{6d} \epsilon^2 R + \mathcal{O}(\epsilon^3) \tag{1.68}$$

In Paper III we explore this quantity for the ground state of the spin-1 Heisenberg model as a function of uniaxial anisotropy and find that the presence of genuine multipartite entanglement comes with a positive state space curvature.

1.1.6   QFIM's in different Guises

Fidelity Susceptibility

A separate thread in the development of quantum information geometry begins with the work of Zanardi and Pauković [39], and the work of Gu [40] who introduced the

ground state overlap[2] as a probe of quantum criticality. The second derivative of this overlap was then developed into the idea of the quantum geometric tensor [36] which is the same notion of distance as that described by the QFIM, but specialized to the case where the parameterization corresponds to terms in the Hamiltonian whose ground state is being considered [41, 42].

Concretely, consider a parameter dependent Hamiltonian $H(\lambda)$, where λ induces a critical point between two phase transitions at the critical value λ_c. Then the fidelity susceptibility is given by the second derivative of the overlap with respect to λ and exhibits a divergence at the critical point that can be analyzed in terms of scaling [43]. As a special case of the QFIM, the relationship to the response functions of the generators still holds [44]. A key difference is that the QFIM corresponding to such parameterizations does not necessarily herald the presence of genuine multipartite entanglement, since the parameter λ might couple to terms in the Hamiltonian that are not linear in the spin degrees of freedom. For example, the FS associated to the uniaxial anisotropy discussed in Sec. 1.2 couples to a term which is a sum of spin operators squared. In so far as the FS associated to this term detected genuine multipartite entanglement, it is only in the square of the spin degrees of freedom. Moreover, the proof provided in [30] considers only the unitary component of the QFIM. Since the FS contains non-unitary contributions, these would not be expected to detect genuine multipartite entanglement.

The simple covariance form of the QFIM in Eq. 1.35 is also claimed not to hold for the fidelity susceptibility, which is computed using a perturbation theory treatment and thus has both unitary and non-unitary contributions, especially near the critical point [41]. This treatment is equivalent to the covariance form in cases where the change in parameter occurs adiabatically. This will not be the case at the critical point itself. In fact the QFIM is stated to have a different scaling relationship at the critical point (see the supplemental discussion in [24]).

The fidelity susceptibility holds special interest due to its ability, by explicit con-

---

[2]This is a pure state version of the Ulhmann Fidelity [27], an interesting quantity in its own right giving the transition probability between density matrices, it can be used to define the Bures distance [26] which, over infinitesimal distances gives precisely the QFIM [4]

struction, to herald the presence of quantum critical points even when the phases being studied are characterized by non local forms of order, such as topological order [45, 46, 47], which cannot necessarily be observed through local correlation functions. In Paper II, we demonstrate that higher derivatives of the QFIM for linear spin operators also signal the presence of such phase transitions. While such divergences unlikely to be observable in the ground state due to experimental limitations, we speculate that they may be observable in the finite temperature critical fan.

Within the bulk of the phase (i.e. away from the critical points), the QFIM corresponding to the fidelity susceptibility may also yield valuable information about the nature of the phase. In particular, one might consider the state space manifold parameterized by a parameter in the Hamiltonian and a twist in the boundary conditions. The topology of this manifold in terms of the Euler Characteristic can be then be used to distinguish between different phases in, for example the XY model [48]. This kind of analysis requires computing (or measuring) the geometry over the entire ground state manifold for a given phase, and relies on parameterizations, such as twists at the boundary, that may be difficult to implement in experiments.

The Quantum Variance

A recent approach to quantifying the presence of coherent quantum fluctuations is the quantum variance [49]. For a hermitian operator $\hat{\Lambda}$ and a Gibbs state (see Eq. 1.27), the fluctuations can be decomposed into a coherent, quantum contribution, and an incoherent thermal contribution,

$$\text{Var}(\hat{\Lambda}; \hat{\rho}) = \text{Var}_{\mathcal{T}}(\hat{\Lambda}; \hat{\rho}) + \text{Var}_{\mathcal{Q}}(\hat{\Lambda}; \hat{\rho}), \tag{1.69}$$

where $\text{Var}_{\mathcal{Q}}$ is the *quantum variance* (QV) and $\text{Var}_{\mathcal{T}}$ is the *thermal variance*. The thermal contribution to the variance can be defined by adding the operator $\hat{\Lambda}$ directly to the Hamiltonian coupled with a field λ,

$$\mathcal{Z}(h) = \text{Tr}\Big(\exp\Big(-\beta(\hat{H} - \lambda\hat{\Lambda})\Big)\Big). \tag{1.70}$$

The thermal variance is then,

$$\text{Var}_{\mathcal{T}}(\hat{\Lambda}; \hat{\rho}) = \frac{1}{\beta}\chi_{\hat{\Lambda}} := \frac{\partial^2 F}{\partial h^2} \tag{1.71}$$

where $F = -\frac{1}{\beta}\ln(\mathcal{Z}(h))$, is the free energy and $\chi_{\hat{O}}$ is the *static thermal susceptibility*. The QV is then defined by using the definition in Eq. 1.71 and rearranging Eq. 1.69,

$$\text{Var}_{\mathcal{Q}}(\hat{\Lambda}; \hat{\rho}) = \text{Var}(\hat{\Lambda}; \hat{\rho}) - \frac{1}{\beta}\chi_{\hat{\Lambda}} \tag{1.72}$$

By reformulating the above expressions as path integrals, it can be shown that the thermal variance corresponds to fluctuations in the eigenstate while the quantum variance corresponds to fluctuations around the centroid for a given eigenstate. In this way, the thermal and quantum variances quantify the coherent and incoherent fluctuations respectively.

It helps to consider the case of a free particle in equilibrium with a heat bath at temperature T. In this case the quantum variance of the position is [49],

$$\text{Var}_{\mathcal{Q}}(\hat{x}; \hat{\rho}) = \frac{1}{24\pi}\lambda_{dB}^2 \tag{1.73}$$

where $\lambda_{dB} = \sqrt{\frac{2\pi\hbar^2}{mk_BT}}$ is the *thermal de Broglie wavelength*. It decreases monotonically to zero as the temperature increases, indicating the falling off of quantum fluctuations at finite temperature.

Another important property of the QV is its relationship to the Wigner-Yanase-Dyson (WYD) skew information [50, 51],

$$\mathcal{I}_\alpha(\hat{\Lambda}; \hat{\rho}) = -\frac{1}{2}\text{tr}\left(\left[\hat{\Lambda}, \hat{\rho}^\alpha\right]\left[\hat{\Lambda}, \rho^{\hat{1}-\alpha}\right]\right). \tag{1.74}$$

This quantity is yet another form of the QFIM, corresponding to the choice of monotone function [23],

$$f_\alpha(x) = \alpha(1-\alpha)\frac{(x-1)^2}{(x^\alpha - 1)(x^{1-\alpha} - 1)}. \tag{1.75}$$

It is shown in Ref. [49] that the QV may be written as,

$$\text{Var}_{\mathcal{Q}}(\hat{\Lambda}; \hat{\rho}) = \int_0^1 d\alpha \, \mathcal{I}_\alpha(\hat{\Lambda}; \hat{\rho}). \tag{1.76}$$

29

So we see that the quantum variance is the average over a particular family of QFIM's. Relative to the SLD QFIM (which we just write as $\mathcal{F}_{\mu\nu}$, the QV acts as both an upper and lower bound,

$$4\text{Var}_{\mathcal{Q}}(\hat{\Lambda}_{\mu}) \leq \mathcal{F}_{\mu\mu} \leq 12\text{Var}_{\mathcal{Q}}(\hat{\Lambda}_{\mu}) \tag{1.77}$$

In Paper I we apply this bound to determine the region of validity of our single mode approximation. Working with the QV is especially appealing from the perspective of stochastic series expansion [52] and path integral Monte Carlo algorithms [53], where there are efficient estimators of the static thermal susceptibility $\chi_{\hat{\Lambda}}$ [54]. We also present a slice of the quantum critical region in terms of the QV above the critical point, where the QV decays with a power law.

Using the representation of the WYD information in terms of response functions, Eq. 1.76 can be written as [55],

$$\text{Var}_{\mathcal{Q}}(\hat{\Lambda}; \hat{\rho}) = \hbar \int_{0}^{\infty} \frac{\text{d}\omega}{\pi} L\left(\frac{\beta\hbar\omega}{2}\right) \chi_{\hat{\Lambda}}''(\omega) \tag{1.78}$$

where,

$$L(x) = \coth(x) - \frac{1}{x} \tag{1.79}$$

is the Langevin function.

The quantum variance can be extended to the *quantum covariance*, which is defined by subtracting off the thermal susceptibility from the correlation function in analogy with Eq. 1.72 [56],

$$\text{Cov}_{\mathcal{Q}}(\hat{\Lambda}_{\mu}, \hat{\Lambda}_{\nu}; \hat{\rho}) = \text{Cov}(\hat{\Lambda}_{\mu}, \hat{\Lambda}_{\nu}; \hat{\rho}) - \text{Cov}_{\mathcal{T}}(\hat{\Lambda}_{\mu}, \hat{\Lambda}_{\nu}; \hat{\rho}) \tag{1.80}$$

where,

$$\text{Cov}_{\mathcal{T}}(\hat{\Lambda}_{\mu}, \hat{\Lambda}_{\nu}; \hat{\rho}) = \partial_{h_{\mu}}\partial_{h_{\nu}} F \tag{1.81}$$

The form in Eq. 1.78 can be extended to include quantum correlations, and we can thus define a quantum covariance matrix with is the same kind of object as the QFIM but with a different weighting function.

1.1.7 Applied Examples of Quantum Geometry

Quantum Variance and QFI for a Single Qubit

We consider a single qubit in thermal equilibrium with a bath of inverse temperature β. We denote explicitly the gap of the qubit with Δ.

$$\rho = \frac{1}{\mathcal{Z}} e^{-\beta \Delta \sigma^z} \tag{1.82}$$

It is easy to rewrite the density matrix explicitly as,

$$\rho = \frac{1}{2}(\mathbb{I} - \tanh(|\Delta|\beta)\hat{\sigma}^z) \tag{1.83}$$

We consider parameterizations of the Hilbert space generated unitarily by the magnetization operator in direction $\hat{n}$,

$$\hat{\Lambda}(\theta, \phi) = \hat{n} \cdot \vec{\sigma} = \cos(\theta)\sin(\phi)\hat{\sigma}^x + \sin(\theta)\sin(\phi)\hat{\sigma}^y + \cos(\phi)\hat{\sigma}^z \tag{1.84}$$

Below we calculate the variance, its quantum and thermal components, and the QFI as a function of β, θ, and ϕ. It is helpful for this purpose to compute the partition function with a source term,

$$\mathcal{Z}(h) = \text{tr}\{\exp\left(-\beta(\Delta\hat{\sigma}^z - h\hat{\Lambda}(\theta, \phi))\right)\}$$

The variance, QV (from Eq. 1.72), and QFI (from Eq. 1.46), for $\phi = \frac{\pi}{2}$ and $\phi = \frac{\pi}{4}$ are shown in Fig. 1.3 with details of the calculations given in App. B.1. We can see that regardless of the orientation, the variance will always saturate at its maximal value in the limit of infinite temperature ($\beta \to 0$). If we imagine the Bloch sphere with its interior as the prototypical representation of the space of pure and mixed states, then the infinite temperature limit corresponds to the center of this sphere. From an information theory perspective, it is the equivalent of a black hole, as all states taken to this limit become indistinguishable. This manifests in the QFI going to zero. We see that the quantum variance also tends to zero. While both the QV and QFIM must go to zero in this limit, they do so at slightly different rates. Their difference is not constant but peaks at some value of β that scales with the energy gap of the system.
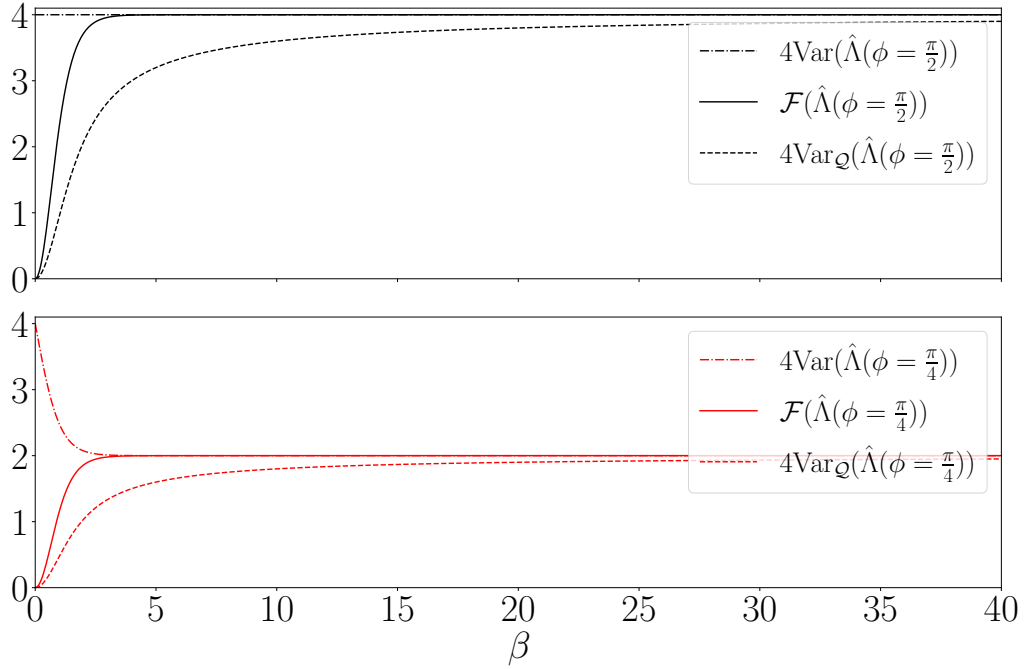
Figure 1.3: Plots of the variance, quantum variance, and quantum Fisher information for two choices of the magnetization operator.

Geometry of two-partite states

Let's consider the following two states,

$$|\psi(\lambda)\rangle = \cos(\lambda) |\!\uparrow_A\downarrow_B\rangle - \sin(\lambda) |\!\downarrow_A\uparrow_B\rangle, \tag{1.85a}$$

$$|\phi(\lambda)\rangle = \cos(\lambda) |\!\uparrow_A\downarrow_B\rangle + \sin(\lambda) |\!\downarrow_A\downarrow_B\rangle \tag{1.85b}$$

on the interval $\lambda \in [0, \frac{\pi}{2}]$. The first state is the singlet in Eq. 1.3 for $\lambda = \frac{\pi}{4}$. This state is maximally entangled, containing one bit of entanglement entropy, as can be seen from the solid red curve in Fig. 1.4. The second state is separable for all possible values of λ and therefore has an entanglement entropy of zero. For both states we can compute the QFI associated with the parameter λ and find that they are identical. The QFI associated with this parameter tells us nothing about the entanglement content of the state. It's easy to see that any single parameter family of states that interpolates smoothly between two orthogonal states in the form given
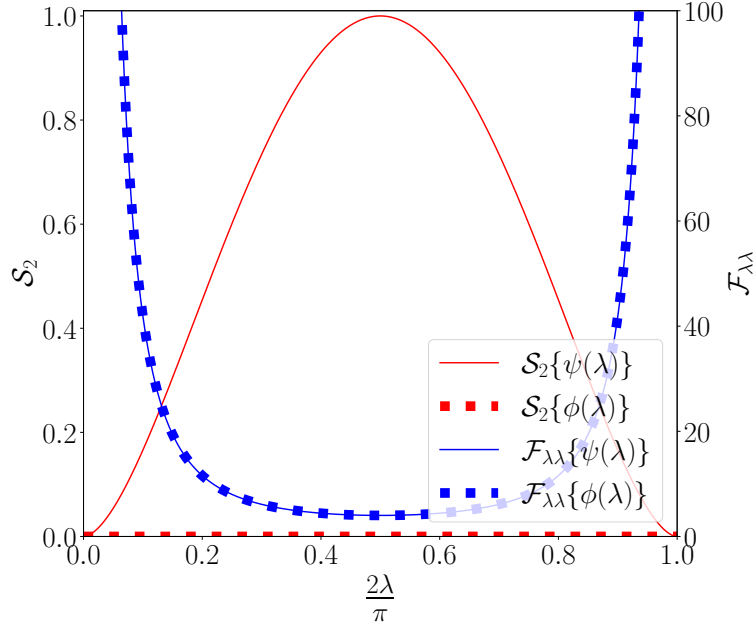
Figure 1.4: Fisher information and Entanglement entropy of the states in Eq. 1.85a and Eq. 1.85b. Here the Fisher information is taken with respect to the parameter λ itself, and is identical for both states. The EE for $|\psi\rangle$ attains a maximum of one bit when the state is maximally entangled, while the EE for $|\phi\rangle$ is always zero.

about will always yield the QFI,

$$F_{\lambda\lambda} = \sec^2(\lambda)\csc^2(\lambda) \tag{1.86}$$

To distinguish between entangled and separable states we must consider a path generated by an operator that is local in the spin degrees of freedom. Even for two spins there is considerable freedom in which operators we might choose. Two choices that will be relevant through this thesis are the ferromagnetic and anti ferromagnetic combinations of each of the three spin operators,

$$\hat{\Lambda}_\mu^\pm = \hat{S}_A^\mu \pm \hat{S}_B^\mu \tag{1.87}$$

where $\mu \in \{x, y, z\}$.

There are now two kinds of parameterizations at play. The first is the parameterization given by λ that connects to the two pure separable states. If, hypothetically,

$|\psi(\lambda)\rangle$ where the ground state of a Hamiltonian depending on λ, then we would call the associated QFI, $\mathcal{F}_{\lambda\lambda}$, the fidelity susceptibility.

The second kind of parameterization is that generated by the operators defined in Eq. 1.87. In this context we only care about this parameterization in the region infinitesimally close to the state. Because the parameterization is unitary, we can compute the associated QFIM entries from the covariance form in Eq. 1.35 for detecting 2-partite entanglement.

Each of these generators defines a unitary operator, which induces an infinitesimal displacement in the state along a path parameterized by h^3,

$$|\lambda, \mathrm{d}h\rangle = e^{i\mathrm{d}h\Lambda_{\mu}^{\pm}} |\lambda\rangle \tag{1.88}$$

The distance between $|\lambda, 0\rangle$ and $|\lambda, \mathrm{d}h\rangle$ is then given by (following Eq. 1.35,

$$F_{\mu\mu}^{\pm}\{\psi\} = 4\mathrm{Cov}_{\psi}(\hat{\Lambda}_{\mu}^{\pm}, \hat{\Lambda}_{\mu}^{\pm}) \tag{1.89}$$

The QFI densities generated by the ferromagnetic and anti ferromagnetic operators are given in Fig. 1.5.

While the separable state, $|\phi\rangle$ never exceeds the bound given in Eq. 1.56, we can see the for the entangled state $|\psi\rangle$ the bound is exceeded by three of the different paths chosen. First for the path given in terms of the z component for the anti-ferromagnetic spin combination, bi-partite entanglement is detected for a window the parameter space $\lambda \in \left[\frac{\pi}{8}, \frac{3\pi}{8}\right]$. The bound is also always violated for the parameterizations generated by the anti ferromagnetic x and y operators for the entire span of λ except at the separable points.

The three ferromagnetic operators defined in Eq. 1.87 (or, equivalently, the three anti-ferromagnetic spin operators), are related to each other by global rotations. We can thus consider the QFIM corresponding to the three dimensional submanifold whose parameterization is generated by these operators and take its trace. The results for the ferromagnetic and anti ferromagnetic operators are given in Fig. 1.6.

---

[3]Technically each operator in Eq. 1.87 corresponds to a different path, so we could write the parameter as $h_{\mu}^{\pm}$
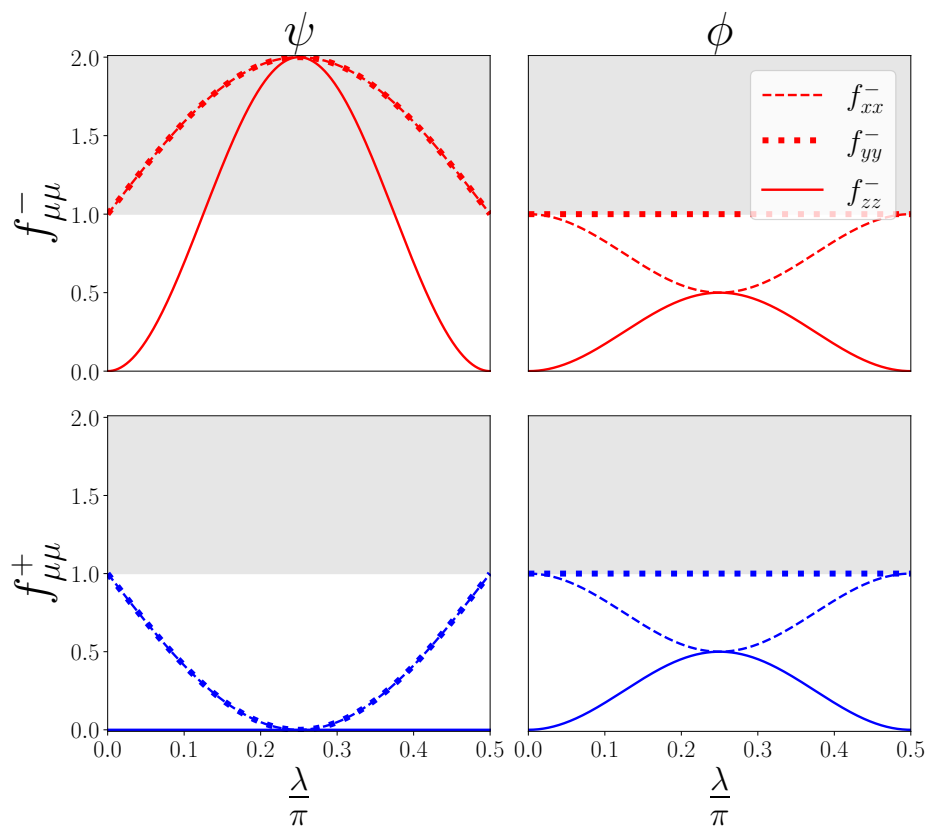
Figure 1.5: Diagonal entries of the QFIM matrix associated with the three ferromagnetic (blue) and anti ferromagnetic (red) generators defined in Eq. 1.87. The three line styles correspond to the x (dashed), y (dotted), and z (solid) lab frame directions. The grey region indicates the bound given in Eq. 1.56.

The bound corresponding to Eq. 1.55 is again given in grey. Here we see that only the anti-ferromagnetic spin combinations detect entanglement.

Notice that at the at the point $\lambda = \frac{\pi}{4}$ all three components of the QFIM for the ferromagnetic combination are zero. The singlet is an eigenstate of the magnetization operator, having total magnetization zero in any of the three spin directions. This special case implies a general principle. If a state $|\psi\rangle$ is an eigenstate of the generator of a parameterization, then its QFI along that parameterization will be zero. This is easy to see if one considers the fact that the QFI for a pure state is just the covariance of the generator for that state.
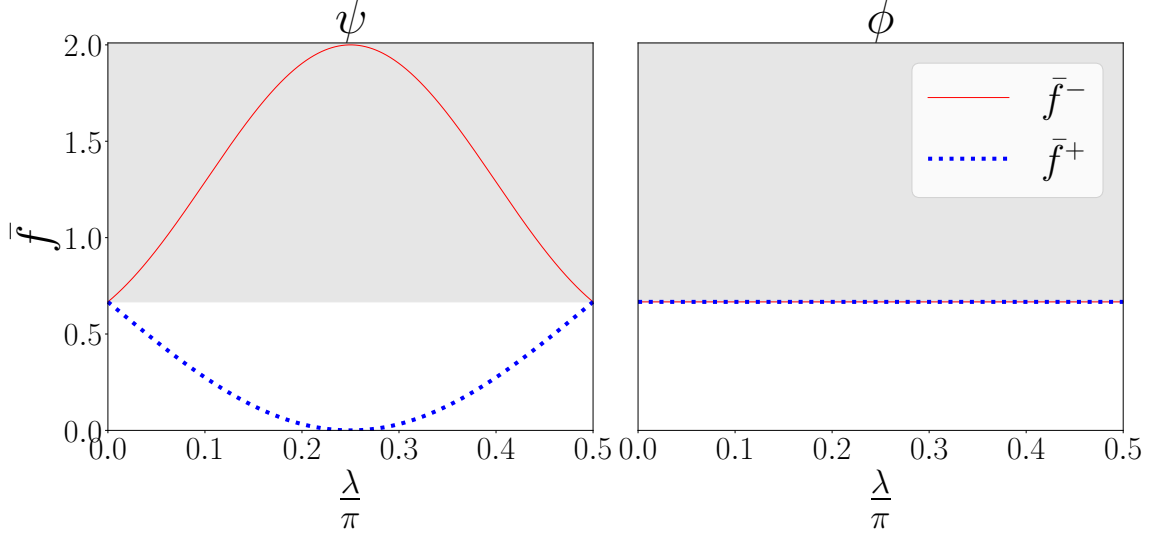
35

Figure 1.6: Trace of the QFIM matrix for the three symmetric (blue) and anti-symmetric (red) generators defined in Eq. 1.87. The grey region indicates the bound on entanglement given in Eq. 1.55 for detecting 2-partite entanglement. Notice that only the symmetric choice detects the bi-partite entanglement in the state $|\psi\rangle$.

More generally, if the Hamiltonian of a system commutes with the generator, then the ground state of that Hamiltonian will tend to exhibit zero QFI. An exception is in the case where the ground state is degenerate. For example, the ferromagnetic Heisenberg chain has a three fold degenerate ground state manifold, which can be used to construct entangled states for which the QFI associated with the ferromagnetic generator does detect entanglement.

In practice, measuring the QFI means applying the generator as a perturbation to the Hamiltonian. This perturbation lifts the degeneracy. The ground state under the perturbation will thus always be an eigenstate of both the generator and the unperturbed Hamiltonian (provided they commute with each other). Consequently, in practice, the QFI shouldn't detect entanglement in this case, despite the fact that the degenerate ground state manifold of the un perturbed Hamiltonian contains states which are not eigenstates of the generator.

36

1.2   The Spin-1 Heisenberg Chain

The results of papers I and III are primarily concerned with the physics of the spin-1 anti-ferromagnetic Heisenberg model,

$$\hat{H} = J \sum_j \vec{S}_j \cdot \vec{S}_{j+1} + D \sum_j (S_j^z)^2 + B_z \sum_j (S^z)j) \tag{1.90}$$

where D controls the uniaxial anisotropy and B_z represents an applied field along the z direction. Unlike the spin-$\frac{1}{2}$ chain which exhibits gapless excitations [57], the ground state of the isotropic ($D = B_z = 0$) chain is gapped. The presence of such a gap was first conjectured by Haldane [58, 59]. The conjecture was experimentally verified in the work of [60, 61]. A major advance was made via the work of Affleck, Kennedy, Tasaki, and Lieb (AKLT) [62], whose insight was to add a biquadratic exchange term,

$$H_\beta = \beta \sum_j \left(\vec{S}_j \cdot \vec{S}_{j+1} \right)^2 \tag{1.91}$$

to the isotropic Heisenberg exchange. When $\beta = -\frac{1}{3}$, the model becomes a sum over projectors onto the spin-2 subspace of neighbouring spin pairs. The ground state can then be understood as a so called *valence bond solid*, where each spin-1 particle considered as a triplet of two spin-$\frac{1}{2}$ degrees of freedom, with each spin-$\frac{1}{2}$ is in a singlet with the spin-$\frac{1}{2}$ on the neighbouring site. This leaves "free" spin-$\frac{1}{2}$ degrees of freedom at the boundary of the open chain that exhibit gapless edge modes.

The combination of a gapped bulk with gapless edge modes is reminiscent of phases of matter that have topological order, like the quantum Hall states [63]. Unlike these states, the bulk gap in the isotropic phase is only protected provided certain symmetries are respected. In particular the $\mathbb{Z}_2 \times \mathbb{Z}_2$ symmetry corresponding to parity and time reversal [11, 64]. For this reason the isotropic phase is considered an example of symmetry protected topological (SPT) order. Unlike phases with intrinsic topological order, the entanglement in the ground state of SPT phases is short ranged [34].

In Papers I and III we demonstrate that the QFI generated by the anti-ferromagnetic magnetization operator detects the presence of this short range entanglement. By
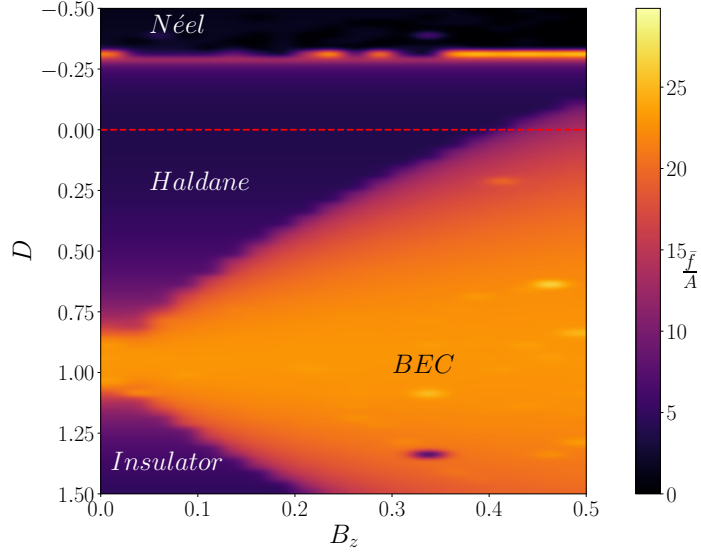
Figure 1.7: Figure reproduced from Paper III [38]. Phase diagram of the genuine multipartite entanglement in the spin-1 AFM Heisenberg model as a function of uniaxial anisotropy, D and applied magnetic field, B_z. The QFIM is generated by the three anti-ferromagnetic operators.

contrast, our study of the Kitaev honeycomb model in Paper II reveals that the QFI associated with operators that are local in the spin degrees of freedom does not appear to exceed the bounds given in Eq. 1.55. Paper III also demonstrates that, for the submanifold defined in Sec. 1.1.5, the isotropic phase has a positive state space curvature.

Above the Haldane gap is a threefold degenerate magnon band. The applied magnetic field, B_z will bring down the energy of the corresponding magnon (x, y, or z), until it hybridizes with the ground state forming a phase which can be understood as a magnon Bose-Einstein condensate (BEC) [65, 66, 67]. The transition occurs at the lower critical field $B_z^{\text{lower}} \approx 0.41$, which is equal to the size of the Haldane gap [68]. At an upper critical field $B_z^{\text{upper}} \approx 4$ the chain becomes a non-degenerate paramagnetic.

The uniaxial anisotropy also drives two phase transitions. At $D \approx -0.31$ there is a Ising type transition to a phase with quasi Néel ordering. In Paper I we confirm
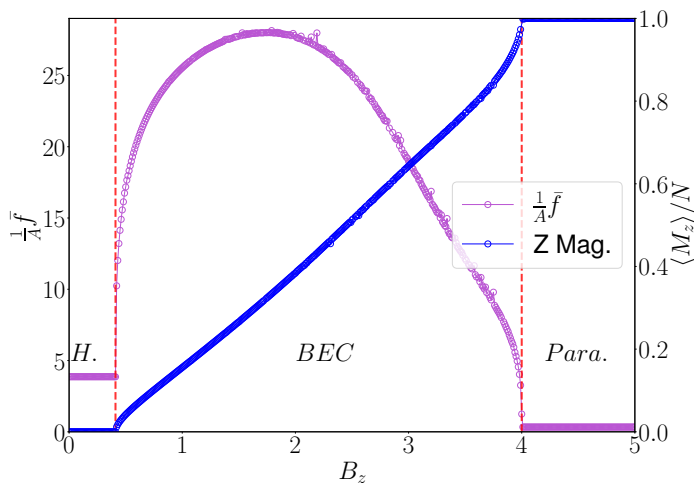
38

Figure 1.8: QFI density along the red line in Fig. 1.7 reproduced from Paper III[38], this slice of the state space goes to larger values of B_z than the phase diagram in Fig. 1.7, and includes the fully polarized phase. The blue curve shows the magnetization per site.

that the scaling relations for the single mode approximated QFI agree with this universality class. There is also a Gaussian type transition to a phase that can be understood as a trivial insulator. In Paper III we determine the phase diagram of the spin-1 chain in terms of the genuine multipartite entanglement for a range of values of D and B_z (see Fig. 1.7).

1.3 Overview of the Field

Surveying the field of quantum geometry, one is given the impression of many branches sprouting from a great tree. In their search for the light, these branches grow towards and away from one another, intermingling and spreading out. The roots of this tree partially predate quantum mechanics itself. They are the mathematical foundations laid by Fubini [19] and Study [20] on the geometry of complex projective spaces (later generalized to account for density matrices by [26]), along side the work of Fisher [5] on statistical distance.

The first branch to sprout (we take time to be vertical) comes from the work of

Helstrom [69] and Holevo [70] who adapted the work of Fisher to the case of quantum decision theory, and the closely related (and somewhat less formally rigorous) work of Wootters [16] who derived a notion of statistical distance for pure states. Wootter's work was later generalized by Braunstein and Caves [17] to include the distinguishability of mixed states (a re casting of the work of Bures [26] interpreted in terms of distinguishability). A summary of the work done by these authors can be found in [71]. This is the branch of quantum metrology, and its central achievement is the generalizing of the classical Cramér-Rao bound given in Eq. 1.19 to the case of quantum mechanics. For a recent review of quantum metrology one may refer to [72]. A major achievement has been the recognition first that the QFI detects genuine multipartite entanglement [30], and second that this entanglement can be leveraged to produce more sensitive measurements of the corresponding Hermitian generators [28]. This branch gives us the term quantum Fisher information, and subsequently, quantum fisher information matrix [73] in the context of multi-parameter estimation.

The second branch begins almost concurrently with the first with the work of Provost and Vallee [74] who take an interest in the Riemmanian structure of the space of coherent states. This work is the first in the physics literature to emphasize the Riemannian structure of the state space as interesting in and of itself. This branch can really be seen as the dual to the work initiated by Berry on the symplectic structure of quantum states [37]. The Symplectic and Riemmanian structures of the Hilbert space are both encapsulated in the QFIM.

The Riemannian geometry of the state space becomes particularly relevant to the study of condensed matter after Zanardi introduced the fidelity susceptibility [39, 36] as a means of detecting quantum critical points (see Sec. 1.1.6). Early achievements involved considering the fidelity susceptibility as a function of temperature [41], and extracting scaling exponents connecting the fidelity susceptibility to the universality class of the quantum phase transitions [43]. In principle it is possible to measure the fidelity susceptibility experimentally [44], but the concept really comes into its own as a theoretical tool, not least of all because of its easy estimation in quantum Monte Carlo simulations [75].

Taking into account multiple directions in the parameter space simultaneously allows for the construction of a geometric tensor for the manifold of ground states (see, for instance [76]). This quantum geometric tensor (QGT) describes at once the Riemannian structure described by Provost and Vallee, and the symplectic structure described by Berry. The symplectic component to the QGT has been applied extensively to the study of topological insulators, which are characterized by the integral of the symplectic component of the manifold (the Chern number) over some relevant space of parameterization (usually the Brillouin zone) [77]. It is natural then to examine the analogous topological invariant for the Riemannian component of the metric, the Euler characteristic. It is perhaps not surprising that the Euler characteristic has also been shown to detect topologically non-trivial insulators [78, 79, 80, 81]. A recent development is the introduction of a generalized Bloch sphere which can be used to understand the Chern number of N level systems [82]. This work has lead to experiments in superconducting qubits [83] and at the NV centers of diamond [84].

While the work on the Euler characteristic has tended to emphasize the QGT associated with the Brillouin zone, work has also been done to consider the topology to the ground state manifold itself. In the work of Kolodrubetz et al. [44, 48], the Euler characteristic of the manifold of the ground states for the XY chain was examined. In that case, the authors consider the manifold created by varying the anisotropy and by included a twist at the boundary. This manifold is found to have topologically singular cusps that distinguish the ferro magnetic and paramagnetic phases.

That this quantum geometric tensor is really the same thing as the quantum fisher information was pointed out by [85]. Until this point it seems that the branch of Heltstrom and the branch of Provost proceeded largely in parallel to one another.

With the work of Hauke et. al [24] a third branch has emerged with exciting connections to the first two. While limits on resolution make examining the quantum critical point itself experimentally challenging [31], the fact that the QFI can be probed directly has opened a new experimental window into the multipartite entanglement of real materials [32, 31]. A recent proposal [86] extends this connection to examine the entanglement is systems that are out of equilibrium. This

follows a number of theoretical investigations. For instance, in the work of Pezze and collaborators [33], the QFI associated with string order generators was found to scale super-extensively in phases of the Kitaev wire with non-trivial band structures. There have also been theoretical studies of Ising chain [24], the XY chain [85], the XXZ chain [87], and the Lipkin-Meshkov-Glick model [88]. The study conducted in Paper I is the first for the spin-1 Heisenberg chain, and establishes the presence of the finite temperature entanglement plateau predicted in [35]. Paper II examines the QFI for the Kitaev honeycomb model [14], finding that, while the QFI does not detect genuine multipartite entanglement, its derivatives do signal the presence of the quantum critical point, with the second derivative diverging. While the motivations of this branch are closely related to the second branch, the means are somewhat different. Rather than consider the geometry in terms of parameters of the Hamiltonian, one considers the geometry in terms of Hermitian generators that are related to the genuine multipartite entnaglement content. As we demonstrate in Paper III, the QFI associated with such generators responds much more strongly to certain transitions, such as the transition from the isotropic phase to the insulator phase in the spin-1 chain, than does the fidelity susceptibility [89, 90].

The quantum variance [49, 56] (discussed in Sec. 1.1.6) compliments nicely the study of the QFI, providing both a bound and a numerically more tractable quantity. Through the study of the QV, one can detect the critical fan found at finite temperatures about the critical point [55]. This work has lead to a connection between the first and third branches in the form of quantum critical metrology [91], wherein the diverging entanglement at the critical point is proposed as a tool for highly sensitive quantum probes.

The central result of Paper III is concerned with connecting the second and third of these branches by introducing a manifold that generalizes those considered experimentally in [84] and [83] to the case of a many body spin-1 system. By understanding the QFI's discussed in the first branch of research as perturbations to the Hamiltonian, and taking these perturbations to be small but not infinitesimal, we used the QFI matrix as a metric (the quantum Fisher information metric discussed above). By computing the volume of spherical manifolds in state space with the

ground state of the spin-1 chain at the center we compute the local curvature in the state space in the vicinity of the ground state for a range of values of the uniaxial anisotropy. Remarkably, our work establishes evidence of a connection between the presence of entanglement as detected by the trace of the QFIM and local curvature in the state space.

Because the results of Paper III rely on operators readily accessible in neutron scattering experiments, this curvature could be measured and manipulated. In light of the results of Paper II, it seems unlikely that the QFI will be applicable to detecting the kinds of long range entanglement that are of interest in the study of quantum spin liquids [92], however other geometrical properties of the state space, such as the curvature, may yet prove to have relevance in this context.

Chapter 2

Entanglement Plateaus in the Spin-1 Chain

Estimates of the quantum Fisher information in the $S = 1$ antiferromagnetic Heisenberg spin chain with uniaxial anisotropy

J. Lambert[*] and E. S. Sørensen[†]

Department of Physics & Astronomy, McMaster University, 1280 Main St. W., Hamilton, ON, Canada L8S 4M1

The quantum Fisher information is of considerable interest not only for quantum metrology but also because it is a useful entanglement measure for finite temperature mixed states. In particular, it estimates the degree to which multipartite entanglement is present. Recent results have related the quantum Fisher information to experimentally measurable probes. While in principle possible, a direct evaluation of the quantum Fisher information at finite temperatures is technically challenging and here we show that a simple estimate can be obtained for materials where the single-mode approximation is valid. We focus on the $S = 1$ antiferromagnetic Heisenberg model with uniaxial anisotropy. Quantum Monte Carlo techniques are used to determine low-temperature correlations from which the quantum Fisher information can be estimated within the single-mode approximation. The quantum Fisher information is compared to the quantum variance for the staggered magnetization operators in the transverse direction and inequalities between the quantum Fisher information, the quantum variance, and the full variance are discussed. Both the quantum and full variance as well as the quantum Fisher information are examined at finite temperatures above the isotropic point and at the quantum critical point for the Haldane-Néel transition. A finite size scaling study of the quantum Fisher information is performed at the quantum critical point and used to confirm the Ising nature of the Haldane-Néel transition.

I. INTRODUCTION

The quantum Fisher information (QFI), F_Q, is often studied in quantum metrology [1–6]. There, one considers unitary dynamics $U = \exp(-i\hat{O}\theta)$ and the phase estimation sensitivity is then limited by the Cramér-Rao bound $(\Delta\theta)^2 \geqslant 1/F_Q[\hat{O}]$ for *any* measurement. From a condensed-matter perspective, the quantum Fisher information is particularly interesting since it can be used to estimate multipartite entanglement even at finite temperatures since $F_Q/N > m$ with m a divisor of N signals $(m + 1)$-partite entanglement [4,6–8]. Significant progress in the understanding of, in particular, bipartite, entanglement in quantum many-body systems has been made [9–11]. More recently, a host of techniques have been developed to efficiently quantify multipartite entanglement in quantum many-body systems. (For a review of entanglement witnesses, see [12–15]). For our purpose we will take the definition of multipartite entanglement to be the natural generalization of bipartite entanglement. Namely, consider an N-body quantum state $|\psi_N\rangle$. Now imagine expressing this state as a product of m states each containing N_m particles $|\psi_N\rangle = \bigotimes_{i=0}^m |\phi_i\rangle$. A k-partite entangled state is one for which the largest constituent state ϕ_i contains $N_i = k$ particles, and cannot be further decomposed. It's clear that one can recover from this the usual definition of bipartite entanglement. Measuring bipartite entanglement is often achieved through the von Neumann entropy, $S_A = -\text{Tr}(\hat{\rho_A} \ln \hat{\rho_A})$, where ρ_A is the partial trace of the full density matrix $\hat{\rho}$. This measure determines the amount of entanglement between the subsystem A and its complement, B. It does not, however, tell us how many particles are entangled in the state. It is in this respect that the QFI differs from the von Neumann entropy in that the QFI allows for measurments of the precise number of particles that are in the most entangled factor state. Ideally, for the study of multipartite entanglement, one would like to use techniques that do not rely on a particular knowledge of the density matrix, as these are the techniques most easily connected to experiment and the QFI seems well suited for this purpose.

Quantifying multipartite entanglement is well motivated by the study of quantum criticality, particularly in systems with phases that are topological in nature. These phases are not characterized by a local order parameter, making the detection of these phases challenging. By measuring the multipartite entanglement through the QFI, progress has been made in exploring the phase diagram of the Kitaev model, which exhibits a topological phase [16]. The QFI has also found application in exploring the non-Markovian limit of open quantum systems [17]. In general, multipartite entanglement must also play a role in isolated quantum dynamics, where systems appear to locally thermalize. Experimental work in [18] has established this connection, and it is therefore reasonable to expect that the QFI will play a role in examining questions of thermalization as well.

The QFI has long been known as a monotonic multipartite entanglement measure [4,6–8], but only recently has it been connected to the dynamic structure factor which is easily accessed by experimental probes such as neutron scattering [19]. This has led to the studies of the QFI and multipartite entanglement in the Kitaev chain [16], quantum Ising

[*]lambej3@mcmaster.ca
[†]sorensen@mcmaster.ca

chain [19], XY spin chain [20], XXZ spin chain [21], and Lipkin-Meshkov-Glick model [22,23]. In order to access the QFI these studies all rely on the exact solvability of the models considered and from a numerical perspective, accessing the Fisher information can be challenging in particular at finite temperature for realistic nonintegrable quantum many-body models. Experimental efforts have also yielded results in estimating the entanglement through the QFI using collections of local measurements, which circumvent the need for full knowledge of the dynamic structure factor [24]. Here we show that a simple estimate of the QFI, F_Q^{SMA}, can be obtained by using the single-mode approximation (SMA) which allows the QFI to be calculated directly from the equal-time structure factor. The quantum variance (QV) has been established as a lower and upper bound for F_Q, $4\langle\delta^2\hat{O}\rangle_Q \leqslant F_Q \leqslant 12\langle\delta^2\hat{O}\rangle_Q$ [25], and at the same time a different upper bound is given by the full variance $F_Q \leqslant 4\langle\delta^2\hat{O}\rangle$ [6]. This then serves as a rigorous check on the validity of the SMA calculations.

We focus on the $S = 1$ antiferromagnetic (AFM) Heisenberg model with uniaxial anisotropy,

$$\hat{H} = J \sum_i \left[\mathbf{S}_i \cdot \mathbf{S}_{i+1} + D\left(S_i^z\right)^2 \right], \qquad (1)$$

where D is the uniaxial anisotropy and we shall take $J = 1$ throughout. At $D = 0$ this model displays the celebrated Haldane gap at $k = \pi$ of $\Delta \sim 0.41J$ and it is quite well established [26,27] that the single-mode approximation works very well around $k = \pi$ for moderate values of D. We perform stochastic series expansion [28–30] (SSE) quantum Monte Carlo simulations to evaluate low-temperature equal-time correlations, from which F_Q^{SMA} is obtained, as well as finite temperature calculations to determine the quantum and full variance. This demonstrates the presence of significant multipartite entanglement even at the isotropic point $D = 0$.

The layout of this paper is as follows. In Sec. II we introduce some of the key properties of the QFI and QV (Sec. II A). We then introduce the single-mode approximation (Sec. II B) and its application to the $S = 1$ AFM Heisenberg model. Then in Sec. III we present SSE results for the system QV and the QFI at the isotropic point as well as for a range of values $D < 0$ toward the quantum critical point before turning to our conclusions in Sec. IV.

II. TECHNIQUES

A. QFI and QV

The quantum Fisher information is one possible generalization of the classical Fisher information, which quantifies the distinguishability of a family of distributions parametrized by one (or possibly several) parameters θ [31,32]. The quantum generalization of this quantifies the distinguishability of a family of quantum states defined by

$$\rho(\theta) = e^{-i\theta\hat{O}}\rho e^{i\theta\hat{O}}, \qquad (2)$$

where $\hat{O} = \sum_r \hat{O}_r^\alpha$ is a sum over local operators. In particular, the QFI can be thought of as the statistical speed related to the rate of change of the Bures distance, which is a metric on the space of density matrices [33]. For a density matrix that in its

eigenbasis is given by

$$\rho = \sum_\lambda p_\lambda |\lambda\rangle\langle\lambda|, \qquad (3)$$

the QFI is given by

$$F_Q = 2 \sum_{\lambda,\lambda'} \frac{(p_\lambda - p_{\lambda'})^2}{p_\lambda + p_{\lambda'}} |\langle\lambda'|\hat{O}|\lambda\rangle|^2. \qquad (4)$$

The relationship between the QFI and the multipartite entanglement has been well established in [4–8]. In particular, for a QFI density:

$$f_Q \equiv F_Q/N > m, \qquad (5)$$

where m is a divisor of N, the system is $(m + 1)$-partite entangled. The QFI thus increases monotonically with the entanglement. One of the most appealing features of the QFI is that it is defined for mixed states, allowing one to determine the entanglement content of a state at finite temperature. Recent work [19] has connected the QFI density to the dynamic structure factor,

$$f_Q(k) = \frac{2}{N^d \pi} \int_{-\infty}^{\infty} d\omega \, \tanh^2\left(\frac{\omega}{2T}\right) S(\omega, k). \qquad (6)$$

The dynamic structure factor is routinely measured in inelastic neutron-scattering experiments and thus provides a highly accessible measure of the multipartite entanglement of a system. In the zero-temperature limit the QFI Eq. (4) reduces to the variance of the operator $\hat{O}$,

$$F_Q = 4(\langle\hat{O}^2\rangle - \langle\hat{O}\rangle^2). \qquad (7)$$

Another experimentally accessible entanglement monotone is the quantum variance [25]. The idea is that at finite temperature both thermal and quantum fluctuations contribute to the variance,

$$\langle\delta^2\hat{O}\rangle \equiv \langle\hat{O}^2\rangle - \langle\hat{O}\rangle^2, \qquad (8)$$

so that we may write

$$\langle\delta^2\hat{O}\rangle = \langle\delta^2\hat{O}\rangle_Q + \langle\delta^2\hat{O}\rangle_T, \qquad (9)$$

with the quantum fluctuations being some indicator of the extent to which a state may be entangled. In order to isolate the quantum component of the fluctuations we may use the fact that the thermal component of the fluctuations is simply given by the susceptibility. We therefore have

$$\langle\delta^2\hat{O}\rangle_Q = \langle\delta^2\hat{O}\rangle - \chi_{\hat{O}}k_B T. \qquad (10)$$

It can be shown that the QV imposes both an upper and lower bound on the QFI [25,34],

$$4\langle\delta^2\hat{O}\rangle_Q \leqslant F_Q \leqslant 12\langle\delta^2\hat{O}\rangle_Q. \qquad (11)$$

Additionally we can see that the total variance of the operator must be an upper bound to the QFI [16]. In Sec. III we compute these quantities and use them to assess the regime of validity of the single-mode approximated QFI. Both the QFI [19] and the QV [25] are thought to take a universal form at the quantum critical point. The exact scaling behavior of these quantities will ultimately be inherited from the operator in terms of which they are defined.

The work in the Supplemental Material of [19] derives the scaling exponents for the QFI density at both zero and finite temperature. We summarize their results here for convenience. For a review of scaling theory one can refer to [35]. Consider a rescaling of the lattice by an amount λ. The operator $\hat{O}$ will then rescale by some amount $\lambda^{-\Delta_\alpha}$. The QFI density will therefore scale as $\lambda^{d-2\Delta_\alpha}$. Thus, we can identify $\Delta_Q = d - 2\Delta_\alpha$ as the scaling dimension for the QFI density. This result holds in the finite temperature case as well. In order to demonstrate this we recall that the temperature and frequency both scale with the dynamical critical exponent z. By examining Eq. (6), we see that the argument of the hyperbolic tangent function is thus scale invariant. That leaves us with the scaling of the dynamical structure factor which scales in the same way as the correlation function, and thus the finite temperature QFI will also scale as $\Delta_Q = d - 2\Delta_\alpha$. For large but finite systems at low but nonzero temperatures we then expect [19]

$$f_Q(T, L) = \lambda^{\Delta_Q} h(\lambda^z T, \lambda/L), \quad (12)$$

where L is the linear size of the system. If simulations are performed at low enough temperatures that the scaling with T can be neglected, it then follows from finite-size scaling that

$$f_Q(L) \sim L^{\Delta_Q}. \quad (13)$$

B. The single-mode approximation

We consider the first-principles definition of the structure factor for the spectrum of the Hermitian operator $\hat{O}$ [36]

$$S(\omega, k) = 2\pi \sum_{\lambda, \lambda'} p_\lambda |\langle \lambda' | \hat{O} | \lambda \rangle|^2 \delta(\omega + E_\lambda - E_{\lambda'}), \quad (14)$$

where $p_\lambda = e^{\beta E_\lambda}/\mathcal{Z}$. The structure factor is a function of k through the definition of the $\hat{O}$. In the limit of $T \to 0$ it can be shown that Eq. (14) takes on the simpler form:

$$S(\omega, k) = \sum_{i, \lambda'} |\langle \lambda' | \hat{O} | 0 \rangle_i|^2 \delta(\omega + E_0 - E_{\lambda'}). \quad (15)$$

Here $|0\rangle$ is intended to represent the ground state. In general, the ground state may be degenerate. The summation index i includes all states having the ground-state energy E_0. The content of the single-mode approximation is twofold. First we assume that only the first two energy levels are substantially populated. Second, we assume that transitions from the ground states to states at energies above the first excited state have negligible matrix elements compared with transitions from the ground-state manifold to the first excited state. That is to say,

$$S(\omega, k) = S_0(k)\delta(\omega - \omega_k^{(01)}) + \tilde{S}(k, \omega), \quad (16)$$

where $|S_0(k)| \gg |\int_{-\infty}^{\infty} \tilde{S}(\omega, k)d\omega|$, and $\omega_k^{(01)} := E_1 - E_0$. In other words, the bulk of the spectral weight is on the transition between the ground state and the first excited state. The $\tilde{S}(\omega, k)$ represents the spectral weight coming from states above the first excited state. Details of this approximation are derived in the Appendix.

In order to employ the single-mode approximation we need some way to determine the gap, $\omega_k^{(01)}$ (we henceforth drop the superscript and allow ω_k to denote the dispersion for the

first excited state). It is clear that due to energy conservation $\text{supp}(\tilde{S}) = \{\omega : \omega_k < \omega_c < \omega\}$, where ω_c denotes the bottom of the continuous portion of the energy spectrum. In order to determine ω_k we multiply Eq. (16) by ω and integrate over all frequencies:

$$\frac{1}{\omega_k} \int_{-\infty}^{\infty} d\omega\, \omega S(\omega, k) = S_0(k) + \frac{1}{\omega_k} \int_{-\infty}^{\infty} d\omega\, \omega \tilde{S}(\omega, k). \quad (17)$$

In order to deal with the $\tilde{S}$, we note that

$$\frac{1}{\omega_k} \int_{-\infty}^{\infty} d\omega\, \omega \tilde{S}(\omega, k) \geqslant \int_{-\infty}^{\infty} d\omega\, \tilde{S}(\omega, k). \quad (18)$$

This assertion is made valid by the positive semidefinite nature of $\tilde{S}$. By substituting this inequality into Eq. (17) we see that the left-hand side is, by definition, the equal-time structure factor $S(k)$, giving

$$\frac{1}{S(k)} \int_{-\infty}^{\infty} d\omega\, \omega S(\omega, k) \geqslant \omega_k, \quad (19)$$

with

$$S^{\alpha\alpha}(k) \equiv \int S^{\alpha\alpha}(k, \omega)d\omega = \sum_r e^{-ikr} \langle S^\alpha(r) S^\alpha(0) \rangle. \quad (20)$$

We may use the following sum rule [37]:

$$\int_{-\infty}^{\infty} d\omega\, \omega S(\omega, k) = \pi \langle [\hat{O}^\dagger, [H, \hat{O}]] \rangle, \quad (21)$$

which applies to structure factors defined in terms of any operator, to evaluate this expression for the spin structure factor, which leaves the bound on ω_k as

$$\omega_k \leqslant \omega_{\text{SMA}}(k) := \pi \frac{\langle [\hat{O}^\dagger, [H, \hat{O}]] \rangle}{S(k)}, \quad (22)$$

where ω_{SMA} denotes the single-mode approximated dispersion. Here, $S(k)$ along with the different components of the commutator can be estimated relatively easily using quantum Monte Carlo methods from which $\omega_{\text{SMA}}(k)$ can then be obtained. Results are shown in Fig. 1(a) for the $S(k)$ from Fourier transforms of the ground-state correlation functions obtained from quantum Monte Carlo calculations. Figure 1(c) shows the resulting $\omega_{\text{SMA}}(k)$.

C. The stochastic series expansion

The SSE framework is by now ubiquitous in condensed-matter theory. We here summarize only the specifics of what we measured, referring the reader to the literature for details on the SSE framework [28,29,38,39]. Static correlation functions are easily measured within the SSE by averaging the static correlation function over a number of configurations. More difficult is the measurement of quantities in imaginary time. For the case of the QV, we recall that the susceptibility in Eq. (10) is given by

$$\chi = \int_0^\beta d\tau \langle \hat{O}(\tau) \hat{O}(0) \rangle. \quad (23)$$

Following the prescription of [38] which involves expanding the imaginary time correlation function in the SSE framework
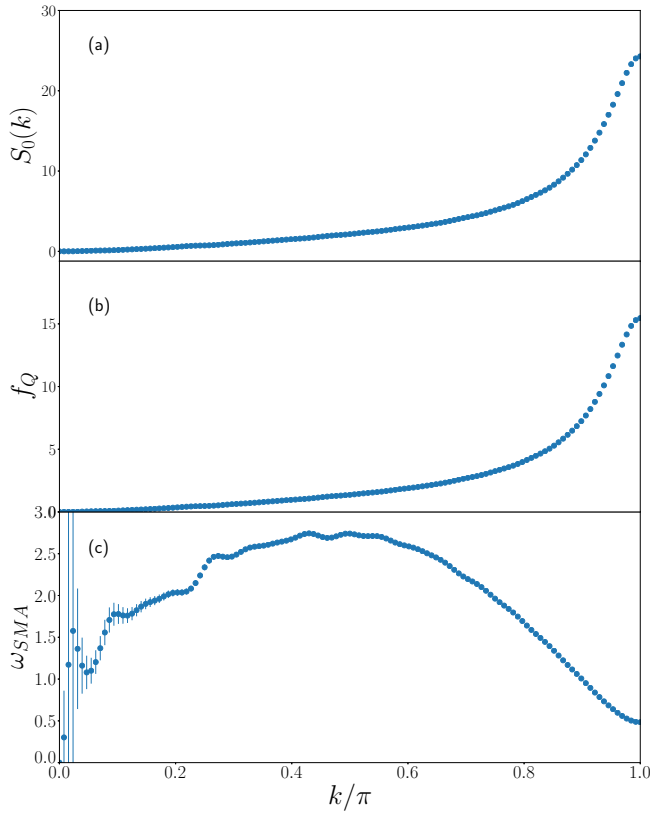
FIG. 1. (a) The equal-time structure factor for the isotropic $S = 1$ AFM model with $N = 256$, $\beta = 400$, exhibiting at peak at $k = \pi$. (b) The QFI density in the first Brillouin zone approaching zero at $k = 0$, and exhibiting a peak at $k = \pi$. (c) ω_k as obtained from the single-mode approximation. The characteristic gap of $0.41J$ at $k = \pi$ is clearly visible.

and exactly computing the integral, we arrive at

$$\chi = \left\langle \frac{\beta}{M(M+1)} \left(\sum_{p=0}^{M-1} o(p) \right)^2 + \frac{\beta}{(M+1)^2} \sum_{p=0}^{n} [o(p)]^2 \right\rangle, \tag{24}$$

where M is the expansion order of the configuration being sampled, and p is the propagation index within that expansion order. The total variance may also be measured directly from the SSE. Once the correlation functions are computed the appropriate transform may be applied to extract $S(k)$.

III. RESULTS

We now turn to a discussion of our results for the QFI and multipartite entanglement in the $S = 1$ AFM Heisenberg model with uniaxial anisotropy,

$$\hat{H} = J \sum_i \left(\mathbf{S}_i \cdot \mathbf{S}_{i+1} + D \left(S_i^z \right)^2 \right). \tag{25}$$

This model has several appealing features to investigate multipartite entanglement. First, it possesses a symmetry-protected topological (SPT) phase with a gapped ground state in the isotropic region, with $\Delta \approx 0.41J$ [40,41]. This phase is characterized by the breaking of a hidden $\mathbb{Z}_2 \times \mathbb{Z}_2$ symmetry

which establishes a long-range string order [42]. Second, the uniaxial anisotropy can drive two quantum phase transitions with critical points falling into two different universality classes. The phase diagram of this model has been extensively investigated in [43–45]. The first transition is from the SPT Haldane phase to a disordered phase with quasi-Néel ordering ($D_C^{HN} \approx -0.31$). The second transition is to a phase which is often called the "large-D phase" ($D_C^{HL} \approx 0.98$). This latter phase is essentially "empty" as the large uniaxial anisotropy forces each spin to have zero S^z projection. The Haldane-Néel transition is in the universality class of the two-dimensional Ising model, while the Haldane-empty transition is in the Gaussian universality class. The excitation spectrum exactly at the isotropic point consists of a triplet state. This degeneracy is lifted away from the isotropic point into a heavier magnon with energy $\omega_k^{(\|)}$ and a lighter doublet with $\omega_k^{(\perp)}$. This notation is meant to evoke the fact that the heavier magnon is in the direction parallel to the uniaxial anisotropy, while the doublet corresponds to the transverse excitations. Most importantly, in a sizable region around $k = \pi$, as well as for $D \neq 0$, the dynamical structure factor is well approximated by a single mode.

We use SSE [28,30,39] techniques to numerically study the QFI within the single-mode approximation. All of the SSE simulations used in this section use on the order of 10^6 Monte Carlo sweeps. The data for each observable is binned into groups of 1000 with the error bars estimated by taking the average variance over the bins.

In order to examine the quantum Fisher information we consider the operator, $S^z(\mathbf{k}) \equiv \hat{O} = \sum_r e^{ikr} \hat{S}_r^z$. The equal-time structure factor for this operator corresponds to the spectrum of spontaneous fluctuations in the longitudinal channel. Using Eq. (22) we may compute the bound on the dispersion for the heavy magnon to be [26]

$$\omega_{\text{SMA}} = \frac{J \left(C_{xx}^{r,r+1} + C_{yy}^{r,r+1} \right) [1 - \cos(k)]}{S_0(k)}, \tag{26}$$

where $C_{\alpha\beta}^{ij} := \langle \hat{S}_i^\alpha \hat{S}_j^\beta \rangle$. For the case of periodic boundary conditions the ground state is not degenerate. We are here concerned with the singlet heavy magnon state. In this case $\eta_0 = \eta_1 = 1$ and thus, as per equation the leading thermal correction does not effect the QFI (see the Appendix for details). Since the single-mode approximation assumes these contributions to be small we ignore these thermal corrections. We may now apply the single-mode approximation to compute the QFI density,

$$f_Q(k) = 4 \tanh^2 \left(\frac{\omega_k}{2T} \right) S_0(k) + \int_{-\infty}^{\infty} d\omega \tanh^2 \left(\frac{\omega}{2T} \right) \tilde{S}(\omega, k), \tag{27}$$

where we shall neglect the last term arising from the continuum contribution. Since this last term corresponds to a positive contribution we would expect to obtain a lower bound on the QFI. We argue, however, that the dominant effect, particularly near the isotropic point, will come from the inequality, $\omega \leqslant \omega_{\text{SMA}}$, Eq. (22). Hence, we believe that an overestimation of the QFI density is the more likely scenario. However, we expect this approximation to be rather good at low temperatures close to the isotropic point, $D = 0$, where

we then obtain the estimate for f_Q,

$$f_Q^{\text{SMA}}(k) \sim 4 \tanh^2 \left(\frac{\omega_{\text{SMA}}}{2T} \right) S_0(k). \qquad (28)$$

We also note that the main T dependence of $f_Q^{\text{SMA}}(k)$ is now through the argument of the tanh. Up to this point Eq. (28) is completely model independent, relying only on ones ability to estimate the single mode. As per the results of Sec. II B, this may be said of any model with a gapped excitation spectrum. Near the critical point it is expected that the continuum will contribute more significantly to the behavior of the system especially at nonzero temperature, since the excitation gap closes. At the isotropic point the energy spectrum is gapped (0.41J). This means that the physics is dominated by the ground-state behavior until the temperature is raised sufficiently to excite higher energy states. This occurs when the temperature is roughly half the gap (0.2J). Because of this gap, the single-mode approximation is considerably more reliable at the isotropic point than at the critical point. With antiferromagnetic exchange, the equal-time structure factor peaks at the $k = \pi$ mode [Fig. 1(a)]. Thus the quantum Fisher information is maximal at the edge of the first Brillouin zone as shown in Fig. 1(b) where $f_Q^{\text{SMA}}(k)$ is shown throughout the Brillouin zone. This corresponds to parametrizing the path through the space of density matrices using the staggered magnetization. At $k = 0$, $\hat{O}$ becomes the total magnetization which commutes with the Hamiltonian and thus cannot detect entanglement. As we approach $k = 0$ the single-mode approximation also becomes invalid since it is known that the well-defined single mode present around $k = \pi$ merges into the continuum. Fortunately the behavior of the single-mode approximation remains well controlled at the edge of the Brillouin zone where the QFI density detected by momentum space magnetization is maximal. In the following we therefore exclusively focus on $k = \pi$.

Let us first consider the finite temperature behavior of the entanglement at the isotropic point, $D = 0$. Using the QV we can make use of the established upper and lower bound on the QFI density. Combining this with Eq. (28) we then obtain

$$4\langle \delta^2 \hat{O} \rangle_Q \leqslant F_Q \sim F_Q^{\text{SMA}} \leqslant 12\langle \delta^2 \hat{O} \rangle_Q. \qquad (29)$$

On the other hand, the total variance is also an upper bound [6] on f_Q: $f_Q \leqslant 4\langle \delta^2 \hat{O} \rangle / N$, where $\langle \delta^2 \hat{O} \rangle$ refers to the total variance, Eq. (8). In Fig. 2 are shown results for $f_Q^{\text{SMA}}(k = \pi)$ for a range of temperatures. In this regime the single-mode approximation should work quite well up until approximately half the gap. We see that, while the approximated QFI satisfies the upper bound given by the full variance, $\langle \delta^2 \hat{O} \rangle$, for all temperatures up to the gap, f_Q^{SMA} breaks the upper bound given by the quantum variance at a temperature of approximately 0.275. We see that up until this point the approximated QFI density predicts the presence of multipartite entanglement well into this regime. If we use the quantum variance as a lower bound on $f_Q(k)$, then it predicts multipartite entanglement to temperatures approaching the gap. In Fig. 2 the shaded green region indicates the threshold to be exceeded for bipartite to be present and we note that both estimates of
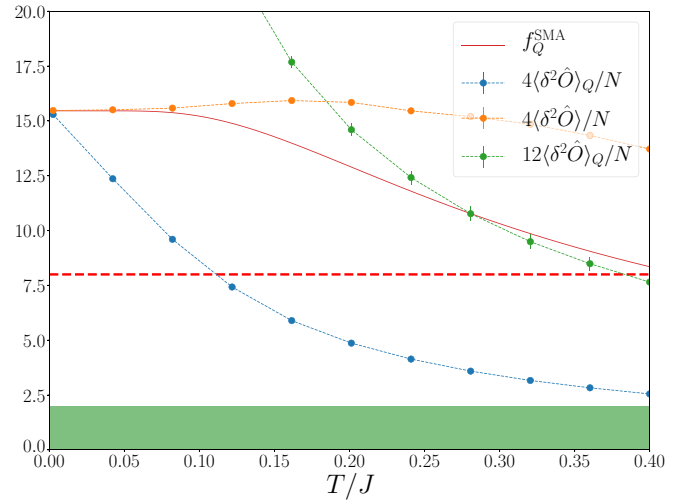

FIG. 2. Finite temperature behavior of the QFI density, $f_Q(k = \pi)$ and the quantum variance for temperatures up to the Haldane gap at the isotropic point, $D = 0$, for $N = 256$. f_Q^{SMA} is obtained from simulations at $\beta = 400$. Upper and lower bounds for f_Q given by $4\langle \delta^2 \hat{O} \rangle_Q / N$ (blue) and $12\langle \delta^2 \hat{O} \rangle_Q / N$ (green) are shown along with the upper bound defined by the full variance, $4\langle \delta^2 \hat{O} \rangle / N$. The green shaded region indicates the level that the f_Q has to exceed to indicate the presence of *more than* bipartite entanglement. The dashed red line indicates the threshold for (8+1)-partite entanglement. Below that line and above the green region the system would be (4+1)-partite entangled.

$f_Q(k = \pi)$ indicate the presence of bipartite entanglement up to temperatures close to the gap.

We may now ask how the ground-state QFI density will behave as we approach the quantum critical point. Figure 3 shows the approximated QFI density indicated by the color intensity for a range of temperatures and D values for a system size of 256 and $\beta = 400$ with periodic boundary conditions. We see that the QFI density is divergent at the quantum critical point, as expected from the behavior of $\hat{O}$. Figure 4 clearly shows the QFI density predicted by the single-mode approximation decays rapidly above the critical point, as the gap has now effectively closed. In this case the hard upper bounds given by the quantum variance are violated at relatively low temperatures. This is not surprising, as we expect the SMA to function only at the very lowest temperatures. Nonetheless, the approximated QFI remains below the bound given by the full variance. We see in this case that there is still persistent multipartite entanglement at finite temperatures above the quantum critical point.

The divergence of the entanglement at the critical point is seen by examining the QFI density for various system sizes. Figure 5 demonstrates the divergent scaling of both the QFI and the QV. Due to the fact that the Haldane-Néel transition is in the Ising universality class we can compute theoretically what the finite size scaling of the QFI density at the critical point must be. At low enough temperatures this is for finite systems given by Eq. (13). For the Ising universality class the critical exponent for the staggered magnetization is given by $\Delta_\alpha = 1/8$. This is confirmed in [44] using cluster expansion methods. This should give a QFI density scaling of $\Delta_Q = 3/4$. By examining even system sizes between $N = 64$ and
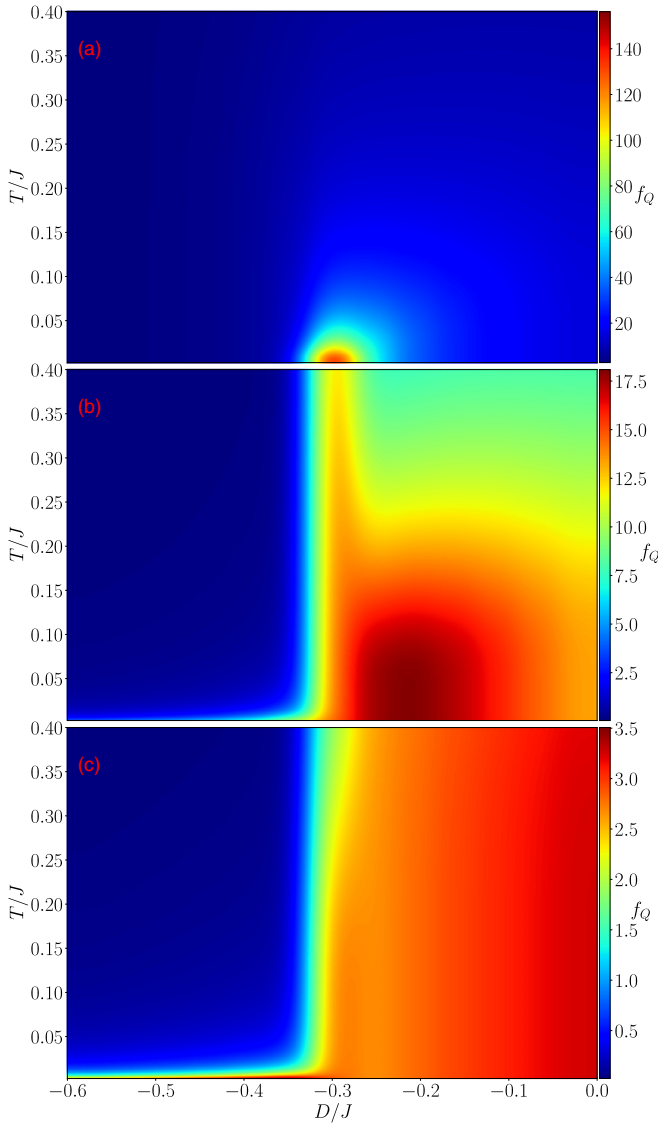
FIG. 3. QFI density detected for $\hat{O}(k) = \sum_r e^{ikr} S_r^z$ around the phase transition from the SPT Haldane phase to the disordered quasi-Néel phase for $N = 256$ for (a) $k = \pi$, (b) $k = 126\pi/128$, and (c) $k = 3\pi/4$. Obtained from SSE results ($\beta = 400$) and periodic boundary conditions. We note the diverging QFI density at the critical point, $D = -0.31$. In panel (c) we note that there appears to be persistent three-partite entanglement up to temperature on the order of the Haldane gap. Panel (c) shows the clear distinction in entanglement structure between the SPT phase for $D > -0.31$ and the disordered phase.

$N = 128$ at a $\beta = 400$ at a value of $D_C^{HN} = -0.31$ we estimate a QFI density scaling of $\Delta_Q = 0.7269(1)$. The error quoted here is associated with the quality of the linear regression. It does not account for systematic errors in the measurement of the QFI density. In order to estimate these systematic errors we examine subsets of four points and determine the maximum and minimum slopes that could be inferred from such four-point subset of the data. Using this we estimate a deviation of at least ± 0.06. Thus the estimated scaling is $\Delta_Q = 0.73 \pm 0.06$. This estimate is consistent with the Ising universality class predicted for this transition.
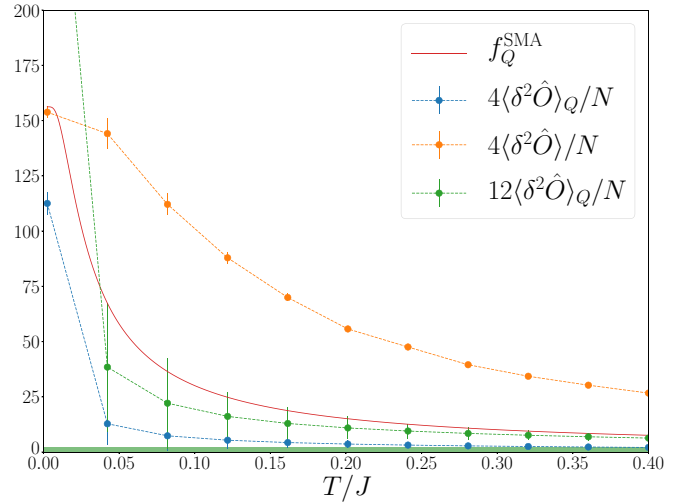

FIG. 4. Finite temperature QFI density and QV above the critical point for $N = 256$. f_Q^{SMA} is obtained from simulations at $\beta = 400$. Upper and lower bounds for f_Q given by $4\langle \delta^2 \hat{O} \rangle_Q / N$ (blue) and $12\langle \delta^2 \hat{O} \rangle_Q / N$ (green), are shown along with the upper bound defined by the full variance, $4\langle \delta^2 \hat{O} \rangle / N$. The green shaded region indicates the threshold f_Q has to exceed for bipartite entanglement to be present.

IV. CONCLUSIONS

Using the single-mode approximation we have shown that it is possible to obtain a quite simple estimate of the QFI density that should yield reliable results at temperatures well below the gap. We studied the $S = 1$ antiferromagnetic spin chain with uniaxial anisotropy within this approximation. The approximation yields results that are within rigorous upper and lower bounds at low temperatures where we expect the SMA to be a reasonable approximation. Clear signatures of
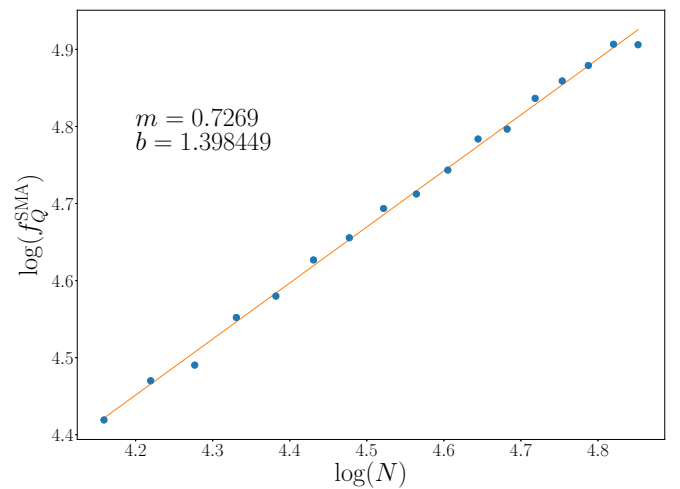

FIG. 5. Finite size scaling of the QFI density with system size for even system sizes between $N = 64$ and $N = 128$. Scaling was performed at $D = D_C = -0.31$ at $\beta = 400$ small enough that the system size would be the relevant perturbation to the scaling. The critical exponent with error due to the fit is found to be $\Delta_Q = 0.7269(1)$ with purely statistical error estimate.

multipartite entanglement were found at the isotropic point, $D = 0$, with the QFI density diverging when approaching the quantum critical point. When combined with the QV, the single-mode approximated QFI allows one to place both upper and lower bounds on the finite temperature entanglement of gapped systems. More precise techniques for calculating the QFI density at finite temperatures in strongly correlated systems would clearly be very desirable. Alternatively, sharper lower or upper bounds on the QFI density than we have discussed here would be very valuable.

We also note that the QFI has been linked to the canonical energy in gravitational physics [46] and can be expressed in terms of the relative entropy [47], developments which could potentially be exploited for more efficient numerical calculations of the QFI.

APPENDIX: DETAILS OF THE SINGLE-MODE APPROXIMATION

We herein consider the details of the SMA and its leading order thermal corrections. Our aim is to show explicitly how one arrives at Eq. (16), and how the finite temperature corrections to this equation may be accounted for. Recall the definition of the structure factor,

$$S(\omega, k) = 2\pi \sum_{\lambda, \lambda'} p_y |\langle \lambda' | \hat{O} | \lambda \rangle|^2 \delta(\omega + E_\lambda - E_{\lambda'}). \quad \text{(A1)}$$

In the case where the system is in thermal equilibrium with a bath of inverse temperature β, the probabilities p_λ are drawn from a Gibbs ensemble, $\hat{\rho} = \exp{-\beta \hat{H}}/\mathcal{Z}$, where $\mathcal{Z}$ is the partition function, $\mathcal{Z} = \text{Tr} \exp{-\beta \hat{H}}$. For compactness, we denote the product of the matrix element amplitude and the delta function $\Gamma_{\lambda, \lambda'} \equiv |\langle \lambda' | \hat{O} | \lambda \rangle|^2 \delta(\omega + E_\lambda - E_{\lambda'})$. In the following derivation we identify E_0 as the ground-state energy of the system, and $|0_i\rangle$ as the set of states in the ground-state

manifold, with η_λ being the number of states in the manifold with energy E_λ. Further, we denote the difference between two energy levels, λ and λ' as $\omega_{\lambda\lambda'} \equiv E_\lambda - E_{\lambda'}$. Let us expand Eq. (A1), and manipulate it so as to more easily take the zero temperature limit,

$$
\begin{aligned}
S(\omega, k) &= 2\pi \frac{\sum_{\lambda, \lambda'} e^{-\beta E_\lambda} \Gamma_{\lambda, \lambda'}}{\sum_\lambda \eta_\lambda e^{-\beta E_\lambda}} \\
&= 2\pi \frac{e^{-\beta E_0} \left(\sum_{i, \lambda'} \Gamma_{0_i, \lambda'} + \sum_{\lambda \neq 0_i, \lambda'} e^{-\beta \omega_{\lambda 0}} \Gamma_{\lambda, \lambda'} \right)}{e^{-\beta E_0} \left(\eta_0 + \sum_{\lambda \neq 0_i} \eta_\lambda e^{-\beta \omega_{\lambda 0}} \right)} \\
&= 2\pi \frac{\sum_{i, \lambda'} \Gamma_{0_i, \lambda'} + \sum_{\lambda \neq G_i, \lambda'} e^{-\beta \omega_{\lambda 0}} \Gamma_{\lambda, \lambda'}}{\eta_0 + \sum_{\lambda \neq 0_i} \eta_\lambda e^{-\beta \omega_{\lambda 0}}}. \quad \text{(A2)}
\end{aligned}
$$

We are now in a position to take the zero temperature limit of Eq. (A2). This is equivalent to the limit where β goes to infinity. Clearly, $\omega_{\lambda 0}$ is strictly positive for the case where $|\lambda\rangle$ is not in the ground-state manifold. Thus when taking the zero temperature limit we find that the only remaining term is

$$S^{T=0}(\omega, k) = \frac{2\pi}{\eta_0} \sum_{i, \lambda'} |\langle 0_i | \hat{O} | \lambda' \rangle|^2 \delta(\omega + E_0 - E_{\lambda'}). \quad \text{(A3)}$$

So far this has been exact. The single-mode approximation consists of assuming that the transition between the ground state and the first excited state constitutes the dominant transition in the system at zero temperature. More explicitly,

$$S^{T=0}(\omega, k) = 2\pi \frac{[S_0(k)\delta(\omega - \omega_{10}) + \tilde{S}(\omega, k)]}{\eta_0}, \quad \text{(A4)}$$

where

$$S_0(k) \equiv \sum_{i, j} |\langle 0_i | \hat{O} | 1_j \rangle|^2, \quad \text{(A5)}$$

where $|1_j\rangle$ is the jth state in the energy manifold of the first excitation energy, and

$$\tilde{S}(\omega, k) \equiv \sum_{i, \lambda'} \Gamma_{0_i, \lambda'}. \quad \text{(A6)}$$

The single-mode approximation is then formally expressed by arguing that $|\langle 0_i | \hat{O} | 1_j \rangle|^2 \gg |\langle 0_i | \hat{O} | \lambda \rangle|^2$, which means that Eq. (A4) becomes

$$S_{\text{SMA}}^{T=0}(\omega, k) \approx 2\pi \frac{\sum_{i, j} |\langle 0_i | \hat{O} | 1_j \rangle|^2 \delta(\omega - \omega_{10})}{\eta_0}. \quad \text{(A7)}$$

At finite temperature it becomes possible for higher energy states to be occupied, and for transitions from these excited states to lower and higher energy states to make contributions to the spectral weight. We can make progress here by including the leading thermal correction and subsequently applying the same single-mode approximation argument. Consider the low-temperature structure factor which includes terms with the Boltzmann weight $\exp{-\beta \omega_{10}}$,

$$S^{T \ll 1}(\omega, k) = 2\pi \frac{\sum_{i, j} |\langle 0_i | \hat{O} | 1_j \rangle|^2 [\delta(\omega - \omega_{10}) + \delta(\omega + \omega_{10}) e^{-\beta \omega_{10}}] + \sum_{i, \lambda} \Gamma_{0_i, \lambda} + \sum_{j, \lambda} e^{-\beta \omega_{\lambda 1}} \Gamma_{1_j, \lambda}}{\eta_0 + \eta_1 e^{-\beta \omega_{10}}}. \quad \text{(A8)}$$

We may now apply the same single-mode approximation to Eq. (A8) as we did the zero temperature, Eq. (A4), which results in

$$S_{\text{SMA}}^{T \ll 1}(\omega, k) = 2\pi \frac{\sum_{i, j} |\langle 0_i | \hat{O} | 1_j \rangle|^2 [\delta(\omega - \omega_{10}) + \delta(\omega + \omega_{10}) e^{-\beta \omega_{10}}]}{\eta_0 + \eta_1 e^{-\beta \omega_{10}}}. \quad \text{(A9)}$$

Substituting the above expression into the definition of the QFI and using the equal-time structure factor, $S(k)$, we are left with the following approximation:

$$f_Q^{\mathrm{SMA}} \approx 4 \tanh^2 \left(\frac{\omega_{10}}{2T} \right) S(k). \tag{A10}$$

The SMA is thought to be valid when a system exhibits a gapped excitation spectrum, at temperatures that are small enough relative to the energy gap that the system is unlikely to be found in an excited state. In the case of the Haldane model this occurs at approximately half the Haldane gap ($0.2J$), as can be seen in the work by Becker *et al.* [48], amongst other works.

[1] D. Petz and C. Sudár, J. Math. Phys. **37**, 2662 (1996).

[2] D. Petz, J. Phys. A: Math. Gen. **35**, 929 (2002).

[3] M. G. A. Paris, Int. J. Quantum. Inf. **07**, 125 (2009).

[4] G. Tóth, Phys. Rev. A **85**, 022322 (2012).

[5] G. Tóth and D. Petz, Phys. Rev. A **87**, 032324 (2013).

[6] G. Tóth and I. Apellaniz, J. Phys. A: Math. Theor. **47**, 424006 (2014).

[7] L. Pezzé and A. Smerzi, Phys. Rev. Lett. **102**, 100401 (2009).

[8] P. Hyllus, W. Laskowski, R. Krischek, C. Schwemmer, W. Wieczorek, H. Weinfurter, L. Pezzé, and A. Smerzi, Phys. Rev. A **85**, 022321 (2012).

[9] J. Eisert, M. Cramer, and M. B. Plenio, Rev. Mod. Phys. **82**, 277 (2010).

[10] N. Laflorencie, Phys. Rep. **646**, 1 (2016).

[11] M. Headrick, Phys. Rev. D **82**, 126010 (2010).

[12] R. Horodecki, P. Horodecki, M. Horodecki, and K. Horodecki, Rev. Mod. Phys. **81**, 865 (2009).

[13] V. Vedral, M. B. Plenio, M. A. Rippin, and P. L. Knight, Phys. Rev. Lett. **78**, 2275 (1997).

[14] L. Amico, R. Fazio, A. Osterloh, and V. Vedral, Rev. Mod. Phys. **80**, 517 (2008).

[15] M. B. Plenio and S. Virmani, Quant. Inf. Comput. **7**, 1 (2007).

[16] L. Pezzè, M. Gabbrielli, L. Lepori, and A. Smerzi, Phys. Rev. Lett. **119**, 250401 (2017).

[17] A. Rivas, S. F. Huelga, and M. B. Plenio, Rep. Prog. Phys. **77**, 094001 (2014).

[18] A. M. Kaufman, M. E. Tai, A. Lukin, M. Rispoli, R. Schittko, P. M. Preiss, and M. Greiner, Science **353**, 794 (2016).

[19] P. Hauke, L. Tagliacozzo, and P. Zoller, Nat. Phys. **12**, 778 (2016).

[20] W.-F. Liu, J. Ma, and X. Wang, J. Phys. A: Math. Theor. **46**, 045302 (2013).

[21] Q. Zheng, Y. Yao, and X.-W. Xu, Commun. Theor. Phys. **63**, 279 (2015).

[22] S.-S. Li, H.-G. Yi, and R.-H. Chen, Int. J. Theor. Phys. **52**, 1175 (2013).

[23] J. Ma and X. Wang, Phys. Rev. A **80**, 012318 (2009).

[24] C. Zhang, B. Yadin, Z.-B. Hou, H. Cao, B.-H. Liu, Y.-F. Huang, R. Maity, V. Vedral, C.-F. Li, G.-C. Guo *et al.*, Phys. Rev. A **96**, 042327 (2017).

[25] I. Frérot and T. Roscilde, Phys. Rev. B **94**, 075121 (2016).

[26] E. S. Sørensen and I. Affleck, Phys. Rev. B **49**, 15771 (1994).

[27] O. Golinelli, T. Jolicœur, and E. Sørensen, Eur. Phys. J. B **11**, 199 (1999).

[28] A. W. Sandvik and J. Kurkijärvi, Phys. Rev. B **43**, 5950 (1991).

[29] A. W. Sandvik, Phys. Rev. B **57**, 10287 (1998).

[30] O. F. Syljuåsen and A. W. Sandvik, Phys. Rev. E **66**, 046701 (2002).

[31] W. K. Wootters, Phys. Rev. D **23**, 357 (1981).

[32] S. L. Braunstein and C. M. Caves, Phys. Rev. Lett. **72**, 3439 (1994).

[33] M. Gessner and A. Smerzi, Phys. Rev. A **97**, 022109 (2018).

[34] I. Frérot and T. Roscilde, arXiv:1805.03140.

[35] J. Cardy, *Scaling and Renormalization in Statistical Physics* (Cambridge University Press, Cambridge, UK, 1996), Vol. 5.

[36] S. Lovesey, *Condensed Matter Physics: Dynamic Correlations*, Frontiers in Physics (Benjamin Cummings, San Francisco, 1980).

[37] P. Hohenberg and W. Brinkman, Phys. Rev. B **10**, 128 (1974).

[38] A. Dorneich and M. Troyer, Phys. Rev. E **64**, 066701 (2001).

[39] A. W. Sandvik, Phys. Rev. B **59**, R14157 (1999).

[40] F. D. M. Haldane, Phys. Rev. Lett. **50**, 1153 (1983).

[41] I. Affleck, Phys. Rev. B **41**, 6697 (1990).

[42] T. Kennedy and H. Tasaki, Phys. Rev. B **45**, 304 (1992).

[43] Z. Zhang, K. Wierschem, I. Yap, Y. Kato, C. D. Batista, and P. Sengupta, Phys. Rev. B **87**, 174405 (2013).

[44] A. F. Albuquerque, C. J. Hamer, and J. Oitmaa, Phys. Rev. B **79**, 054412 (2009).

[45] W. Chen, K. Hida, and B. C. Sanctuary, Phys. Rev. B **67**, 104401 (2003).

[46] N. Lashkari and M. Van Raamsdonk, J. High Energy Phys. 04 (2016) 153.

[47] M. van Raamsdonk, *New Frontiers in Fields and Strings: TASI 2015 Proceedings of the 2015 Theoretical Advanced Study Institute in Elementary Particle Physics* (World Scientific, 2017), pp. 297–351.

[48] J. Becker, T. Köhler, A. C. Tiegel, S. R. Manmana, S. Wessel, and A. Honecker, Phys. Rev. B **96**, 060403 (2017).

Chapter 3

The QFI at a Topological Transition

Revealing divergent length scales using quantum Fisher information in the Kitaev honeycomb model

James Lambert ⬤ * and Erik S. Sørensen†

Department of Physics & Astronomy, McMaster University, 1280 Main St. W., Hamilton, Ontario L8S 4M1, Canada

We compute the quantum Fisher information (QFI) associated with two different local operators in the ground state of the Kitaev honeycomb model, and find divergent behavior in the second derivatives of these quantities with respect to the driving parameter at the quantum phase transition between the gapped and gapless phases for both fully antiferromagnetic and fully ferromagnetic exchange couplings, thus demonstrating that the second derivative a locally defined, experimentally accessible, QFI can detect topological quantum phase transitions. The QFI associated with a local magnetization operator behaves differently from that associated with a local bond operator depending on whether the critical point is approached from the gapped or gapless side. We show how the behavior of the second derivative of the QFI at the critical point can be understood in terms of the diverging length scales associated to the two and four point correlators of the Majorana degrees of freedom. We present critical exponents associated with the divergences of these length scales.

I. INTRODUCTION

A. Overview

The quantum Fisher information (QFI) $\mathcal{F}$ arises naturally in quantum metrology [1–6]. Given a general state $\rho(\theta)$ where θ is some parameter, the QFI bounds the precision with which θ may be extracted in *anyM* measurements through the Cramér-Rao bound, $\text{Var}_{\hat{\rho}}(\theta_i) \geqslant 1/\sqrt{M\mathcal{F}}$. In other words, the QFI quantifies the extent to which a parameterized state $\rho(\theta)$ may be distinguished from a neighboring state $\rho(\theta + d\theta)$. By quantifying the distinguishability of neighboring states, the QFI furnishes a natural notion of distance on the Hilbert space, with more easily distinguishable states separated by a greater distance. Formally, the QFI quantifies the local change in the Bures distance under the aforementioned parameterization [7–10]. This geometrical interpretation of the QFI expands its scope of application to probing the physics of condensed matter phases and phase transitions [11–17]. The QFI also exhibits interesting behavior during a quantum quench in spin chain systems [18]. In fact, a special case of the QFI is already ubiquitous in theoretical studies of condensed matter systems. The fidelity susceptibility (FS) [19] is directly proportional to the QFI [20] for an appropriate parameterization. In particular, one often considers parametrizations that have been generated unitarily (though this is not the only choice) by a Hermitian operator $\hat{O}$ according to $\rho(\theta) = e^{i\theta\hat{O}}\rho e^{-i\theta\hat{O}}$ and we will restrict ourselves to this case here. The operator $\hat{O}$ is usually expressed as a sum over suboperators $\hat{O}^\alpha$,

$$\hat{O} = \sum_r \hat{O}_r^{\alpha_r}. \tag{1}$$

A *local* operator is one for which all $\hat{O}_r^{\alpha_r}$ depend on a contiguous sublattice that is small relative to the total lattice. One may also consider *nonlocal* parametrizations, such as the string operators considered in Ref. [21]. Nonlocal parameterizations reveal remarkable behavior in topological phases as demonstrated in Ref. [21], where a characteristic, superextensive scaling of the nonlocal QFI is demonstrated in the topologically nontrivial phases of the Kitaev wire.

In a many-body state containing N degrees of freedom, the QFI density $F = \mathcal{F}/N$ quantifies the degree of multipartite entanglement when the state ρ is projected into the eigenbasis of the operator $\hat{O}$ that generates the parametrization. For $F > m$ where $m|N$, we say the state is $(m + 1)$ partite entangled [4,22,23]. Specifically, for the case of pure states ψ and unitary parametrizations, the QFI is proportional to the variance of the generator [7]

$$\mathcal{F} = 4\text{Var}_\psi(\hat{O}). \tag{2}$$

While one could perform an interesting study looking only at the variances, we prefer to work within the context of the QFI because it continues to be well defined at finite temperature. This link allows the critical properties of the ground state to be inferred from the thermal scaling of the QFI [12,24]. While we do not consider finite temperature behavior in this study, the connection offers a path forward for future work. Recently, it was shown that the QFI can be detected experimentally in inelastic scattering measurements [12]. Thus working within the context of the a locally defined QFI also allows for connection with experiment. This contributes to a growing body of research on experimental approaches to extract multipartite entanglement [25–27]. We emphasize that we do not detect genuine multipartite entanglement in this study, but mention the connection for completeness.

Given that the QFI is defined at finite temperature and that the zero temperature QFI is proportional to the variance,

---

*lambej3@mcmaster.ca
†sorensen@mcmaster.ca

one might ask, what is the generalization of the notion of variance to the finite temperature case? By imagining that the variance of an observable contains a quantum contribution and a thermal contribution, quantum variances (QV) may be defined which are proportional to an upper and lower bounds of the QFI [28]. The QFI at zero temperature can be viewed as the zero-temperature limit of the quantum contribution to the variance (the thermal contribution being zero at zero temperature).

The QFI has now been studied in a wide range of models [12–16]. Of particular interest for our purposes is the work done on the Kitaev wire in Ref. [21], where the first derivative of the QFI associated with a local generator was shown to exhibit a divergence at the topological phase transition of that model, and where the topologically nontrivial phase exhibits superextensive scaling of the QFI associated with a nonlocal generator.

Quantum spin liquids (QSL) are characterized by a lack of any form of long-range magnetic order down to zero temperature [29]. Such phases are thought to exhibit instead subtle forms of quantum ordering, along with topologically nontrivial anyonic excitations [30]. In so far as these phases are characterized by a lack of order, their detection in experiment presents a substantial challenge. In this work we examine the behavior of the QFI in the Kitaev honeycomb model (KHM) [31], which presents two spin liquid phases (one gapped and one gapless), induced by exchange coupling anisotropy.

The KHM has been studied from an information theoretic perspective before, with studies examining the Jensen-Shannon divergence [32] and the mutual information [33]. Of particular interest is the Fidelity susceptibility, which was studied in Ref. [17] and the study of the Bures distance in Ref. [34]. In the case of an n parameter estimation scenario (or an n-dimensional unitary parametrization), the Bures distance is locally equivalent to the QFI Matrix which is a Riemannian metric on the Hilbert space [7]. The Fidelity susceptibility is recovered by examining the particular parametrization of the Hilbert space corresponding to the driving operator of the phase transition. The physics of the KHM have also been studied using SU(2) parton approaches [35]. Details of the dynamical response of the model in the presence of magnetic fields may be found in Ref. [36].

For the remainder of this section we introduce the KHM and explain its key features. In Sec. II we discuss the relationship between the scaling of the second derivative of the QFI density (hereafter called the QFI *susceptibility*) $\partial_u^2 F$, where u drives the phase transition and the correlation functions of the generator. In Sec. III we analyze the behavior of these quantities for the *magnetization* operator $\sum_j S_j^\alpha$ (where j represents both a unit cell position and sublattice index), in Sec. III A and the *bond* $\sum_r S_{r,A}^\alpha S_{r,B}^\alpha$, where r indicates a unit cell in Sec. III B. Finally, we conclude our discussion in Sec. IV, where we discuss the relevance of this work to studies of the geometric phase.

B. Kitaev honeycomb model

The Kitaev honeycomb model (KHM) is given by

$$H = \sum_{\langle j,k \rangle} K^{\gamma_{j,k}} S_j^{\gamma_{j,k}} S_k^{\gamma_{j,k}}, \tag{3}$$

where the sum is over nearest-neighbor bonds and $\gamma \in \{x, y, z\}$ denotes a bond-dependent Ising exchange. If the exchange couplings are sufficiently isotropic ($|K^\gamma| \leqslant |K^\alpha| + |K^\beta|$, for all choices of $\alpha, \beta, \gamma \in \{x, y, z\}$), the spectrum is gapless. In the regime where one exchange coupling is dominant (the opposite inequality), the model is gapped. This phase transition between two topologically different spin liquid phases presents no local order parameter. It is instead associated with a subtle kind of symmetry breaking to do with the structure of the gauge fields themselves [31]. On the gapped side of the transition, the model is mapped onto the lattice gauge Ising model [37], with alternative rows of hexagon plaquettes becoming associated with one of the two excitations in that model (conventionally called e and m excitations). In both phases, the spin-spin correlation functions are identically zero beyond nearest neighbor. The model also possesses an extensive number of conserved charges defined by the plaquette operators.

Remarkably, the KHM is analytically solvable [31]. By mapping each spin operator into the space of four Majorana fermions $\{c, b^x, b^y, b^z\}$ via

$$S_j^\gamma = \tfrac{1}{4} i c_j b_j^\gamma,$$

an extensive number of conserved charges can be constructed, given by $u_{j,k} = i b_j^{\gamma_{j,k}} b_k^{\gamma_{j,k}}$. These operators take eigenvalues ± 1. Using the above mapping, the KHM becomes

$$H = \frac{i}{4} \sum_{jk} K^{\gamma_{j,k}} u_{jk} c_j c_k. \tag{4}$$

Since the $u_{j,k}$ commute with the Hamiltonian, we may fix a particular configuration of eigenvalues on each bond, and the problem is reduced to free Majoranas hopping in the gauge fields. The lowest-energy configuration will be the flux free configuration, as follows from Lieb's theorem [38]. We therefore choose to work in the configuration where all $u_{i,j}$ have eigenvalue $+1$ (hereafter referred to as the standard gauge). Once we fix a gauge configuration, the model is a simple hopping Hamiltonian, which may be diagonalized by Fourier transforming and then performing a Bogoliubov rotation, where the mixing angle is defined implicitly via

$$\tan(2\theta_q) = \frac{\epsilon_q}{\Delta_q}, \tag{5}$$

where

$$\epsilon_q = K^\alpha \cos(q_x) + K^\beta \cos(q_y) + K^\gamma, \tag{6a}$$

$$\Delta_q = K^\alpha \sin(q_y) + K^\beta \sin(q_y), \tag{6b}$$

where $\alpha, \beta, \gamma \in \{x, y, z\}$ depending on the choice of which bond acts as the unit cell. Here $q_x = \mathbf{a} \cdot \mathbf{q}$ and $q_y = \mathbf{a} \cdot \mathbf{q}$ where $\mathbf{a}_1$ and $\mathbf{a}_2$ are any choice of translation vectors on the principle lattice and $q = \frac{n}{L_x} \mathbf{b}_1 + \frac{m}{L_y} \mathbf{b}_2$, with L_x and L_y the side length of the lattice, is a general vector in the reciprocal space.

We note that the true, physical ground state, must be the symmetrized product over all physically equivalent choices of the gauge fields (i.e., all choice of the gauge fields resulting in zero flux). Following arguments described in Ref. [39], the operators we consider are not dependent on projection into the physical subspace at large system sizes. Details of the solution to the Kitaev model are provided in Appendix B1.

II. QFI SUSCEPTIBILITY AND DIVERGING LENGTH SCALES

To interpret the divergences at the critical point, consider a generator, $\hat{O} = \sum_r \hat{O}_r$ where the generators are given by a sum over local products of spins $\hat{\mathcal{S}}_r = \prod_{j \in \Lambda_r} S^{\alpha_j}_{r+\ell_j}$, where Λ_r is some local, contiguous sublattice. The associated QFI density in a pure state is given by

$$F\{\hat{O}\} = \frac{1}{N} \sum_{r_1, r_2} \langle \mathcal{S}_{r_1} \mathcal{S}_{r_2} \rangle - \langle \mathcal{S}_{r_1} \rangle \langle \mathcal{S}_{r_2} \rangle. \tag{7}$$

Through Kitaev's mapping, we may decompose our spin blocks into a component operating on the flux sector $\mathcal{B}_r = \prod_{j \in \Lambda_r} b^{\alpha_j}_{r+\ell_j}$ and a component operating on the matter sector $\mathcal{C}_r = \prod_{j \in \Lambda_r} c_{r+\ell_j}$,

$$F\{\hat{O}\} = \frac{1}{N} \sum_{r_1, r_2} \langle \mathcal{B}_{r_1} \mathcal{B}_{r_2} \rangle \langle \mathcal{C}_{r_1} \mathcal{C}_{r_2} \rangle - \langle \mathcal{B}_{r_1} \rangle \langle \mathcal{B}_{r_2} \rangle \langle \mathcal{C}_{r_1} \rangle \langle \mathcal{C}_{r_2} \rangle. \tag{8}$$

Now there are three possible values for the flux sector expectation values. If $\mathcal{B}_r$ is diagonal in the gauge sector, then the contribution from the gauge sector factorizes and gives an overall prefactor of ± 1. If $\mathcal{B}_r$ is strictly off-diagonal, but $\mathcal{B}_{r_1} \mathcal{B}_{r_2}$ has diagonal entries, then the situation is the same. Finally, it may be the case that $\mathcal{B}_{r_1} \mathcal{B}_{r_2}$ has nonzero diagonal elements only for certain separations. Regardless of which scenario is realized, the contribution to the QFI from the flux sector will be independent of u since the gauge fields commute at all points in the phase diagram. The QFI is then given by a sum over the correlation functions in the matter sector Majorana fermions with some prefactor (which might be ± 1 or 0 as a function of the separation), determined by the situation above. We adopt the standard ansatz for the matter sector correlations

$$\langle \mathcal{C}_{r_1} \mathcal{C}_{r_2} \rangle = \Xi(r, u) r^{-a} e^{-\frac{r}{\xi(u)}}, \tag{9}$$

where a is determined by the phase and does not depend explicitly on u, and $\xi(u)$ is a length scale associated with correlations between the Majorana operators which depends on the position in the phase diagram.

Taking the assumption that, near the critical point,

$$\xi(u) \sim |u - u_c|^{-\nu} \tag{10}$$

one can show that the second derivative of the QFI density must diverge at the critical point like

$$\partial_u^2 F\{\hat{O}\} \sim |u - u_c|^{\nu-2}. \tag{11}$$

Therefore $\Delta_{\hat{O}} = \nu - 2$. The QFI and, by extension, the QFI susceptibility, are, in principle, experimentally accessible probes. In particular for the case of local generator such as the total magnetization operator. The QFI can there be used to extract experimentally the scaling of the correlation length associated with the matter sector of the KHM. This analysis is similar to the analysis performed in the supplementary materials of [12], where the authors examined the effects of coarse-graining transformation on the QFI to arrive a scaling hypothesis for the near field and finite temperature regimes.

In practice, experimentally relevant models will not be amenable to the above treatment, as the KHM acquires additional terms in real materials that break the integrability of Kitaev's original solution (e.g., Heisenberg terms and symmetric off-diagonal terms) [40]. In these cases the analysis may instead be applied to the correlation length of the spin degrees of freedom directly, and divergences in the QFI susceptibility may still be linked to the critical exponent for the divergence of a correlation length.

III. QFI SUSCEPTIBILITY FOR MAGNETIZATION AND BOND OPERATORS

Motivated by the results of the authors of Ref. [21], we compute the QFI associated with two local operators and examine the second derivatives of those operators with respect to the driving parameter of the phases transition. In both cases the second derivative of the QFI is found to diverge. We term this the QFI *susceptibility*.

Throughout this section we consider a path through the space of exchange couplings parameterized by u,

$$K^z = 1 + u, \tag{12a}$$

$$K^x = 1, \tag{12b}$$

$$K^y = 1. \tag{12c}$$

For this parametrization, $u_c = 1$ represents the critical point between the gapless phase ($u < 1$) and the gapped phase ($u > 1$). The ground state of the KHM is a function of u and is hereafter denoted as $\psi_0(u)$. We consider the case of fully ferromagnetic and fully antiferromagnetic exchange couplings for both parametrizations (in which case $K^\gamma \to -K^\gamma$). Unless otherwise noted, calculations are carried out for $L_x = L_y = 10^4$ with periodic boundary conditions in a rhombic geometry.

A. Magnetization operator

First we examine the QFI in the Kitaev honeycomb as generated by the magnetization operator

$$\hat{O}^\alpha_M = \sum_r \left(S^\alpha_{r,A} + S^\alpha_{r,B} \right), \tag{13}$$

here $\alpha \in \{x, y, z\}$, r denotes a unit cell in the two site basis, and A, B denotes the sublattice. The corresponding QFI is given by

$$F_{M,\alpha}(u) \equiv F\{\hat{O}^\alpha_M; \psi_0(u)\} = 4\text{Var}_{\psi_0}\left(O^\alpha_M\right) \tag{14}$$

$$= 1 - \frac{1}{N} \sum_q \cos(2\theta_q) \tag{15}$$

with $\psi_0(u)$ defined at the start of this section.

Figure 1 shows this quantity plotted along the path defined by Eq. (12c) for the fully antiferromagnetic [Fig. 1(a)] and ferromagnetic [Fig. 1(b)] cases, respectively. In the AFM case the ground state possesses $F_{M,\alpha} > 1$ for each spin component. This is indicative of at least bipartite entanglement. In a pure state any nonzero QFI is indicative of the presence of quantum correlations. Nonetheless, the QFI in the fully ferromagnetic case is insufficient to witness even bipartite entanglement, indicating that quantum correlations are reduced for the FM coupling.

The absolute values of the derivatives of $F_{M,\alpha}$ will be the same in the AFM and FM cases. This can be seen by
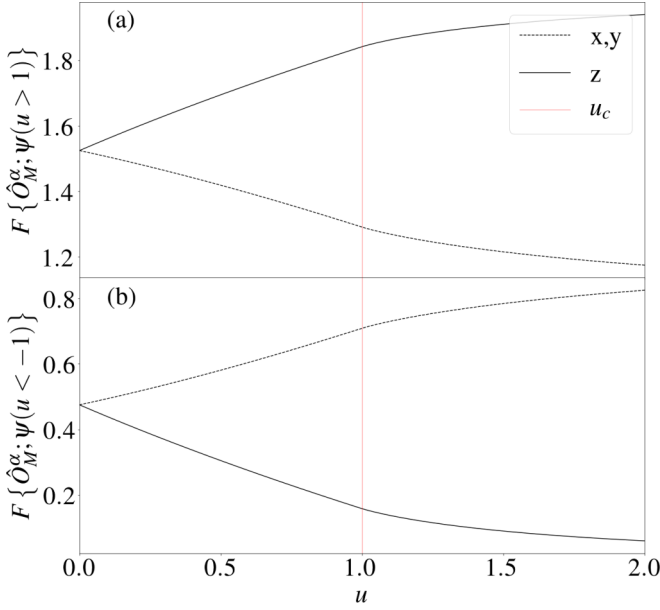
FIG. 1. QFI for Magnetization operator with fully (a) antiferro and (b) ferro magnetic exchange couplings. The red vertical line marks the critical value of u. Results are for $L_x = L_y = 10^4$ with a u spacing of $\sim 10^{-3}$.

considering the fact that the functional dependence of $F_{M,\alpha}$ on the driving parameter u enters through the nearest-neighbor correlation functions, which are the same in both cases up to a negative sign.

The first and second derivatives of the QFI are given in Fig. 2. We observe that the QFI susceptibility associated with the magnetization operator exhibits a power-law divergence
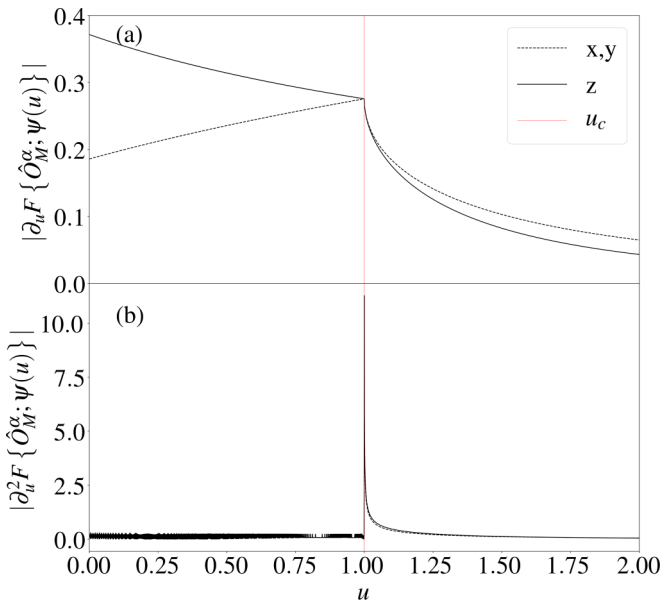

FIG. 2. (a) First and (b) second derivatives of the QFI generated by the magnetization operator. The results are the same in both the ferro and antiferro magnetic cases. Results for $L_x = L_y = 10^4$ with a u spacing $\sim 10^{-3}$. The red line denotes the position of the critical point.
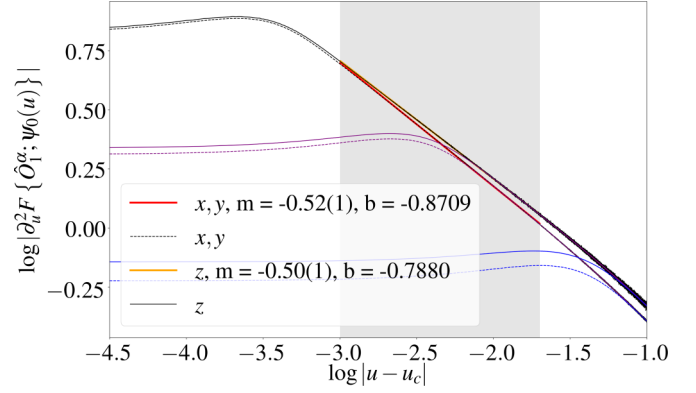

FIG. 3. Log-log plot of the second derivative of the QFI with respect to the magnetization operator and the distance to the critical point from the gapped side ($u > 1$). Results for $L_x = L_y = 10^4$ with a linear $\triangle u \sim 10^{-5}$. The purple and blue curves correspond to system sizes $L_x = L_y = 10^3$ and $L_x = L_y = 10^2$, respectively, and demonstrate that the plateau is a finite-size effect. This regime appears to be valid for approximately the interval $10^{-1.7} > u > 10^{-3.0}$.

when approaching the critical point from the gapped side. When approaching the critical point from the gapless side the transition appears first order. The behavior of the transition from the gapped side can be understood in light of the analysis in Sec. II. Using the scaling hypothesis

$$\partial_u^2 F_{M,\alpha}(u) \sim |u - u_c|^{\Delta_{M,\alpha}}, \qquad (16)$$

we extract the following critical exponents for the second derivative of the QFI for each spin component of the magnetization operator

$$\Delta_{M,x} = \Delta_{M,y} \approx -0.52(1), \qquad (17a)$$

$$\Delta_{M,z} \approx -0.50(1), \qquad (17b)$$

and can be seen in Fig. 3 over a region from $10^{-1.7} > u > 10^{-3.0}$. At this point finite, finite-size effects enter, and the scaling ansatz is no longer valid. This leads to plateaus in the QFI susceptibility which occur closer to the critical point for larger system sizes as seen from the data in Figs. 3 and 5.

B. Bond correlation operator

We now turn to the QFI as parameterized by the bond correlation operator

$$\hat{O}_B^\alpha = \sum_r S_{r,A}^\alpha S_{r,B}^\alpha, \qquad (18)$$

with the corresponding QFI density given by

$$F_{B,\alpha} = \frac{1}{2N} \sum_q \sin^2(2\theta_q). \qquad (19)$$

In this case the AFM and FM cases are identical. We repeat the same analysis as for the magnetization operator as shown in Figs. 4 and 5. The QFI associated with the bond operator along the x and y components converges to a constant value immediately following the phase transition, while the QFI associated with the z component bond operator falls towards zero. This behavior can be understood by the fact that the
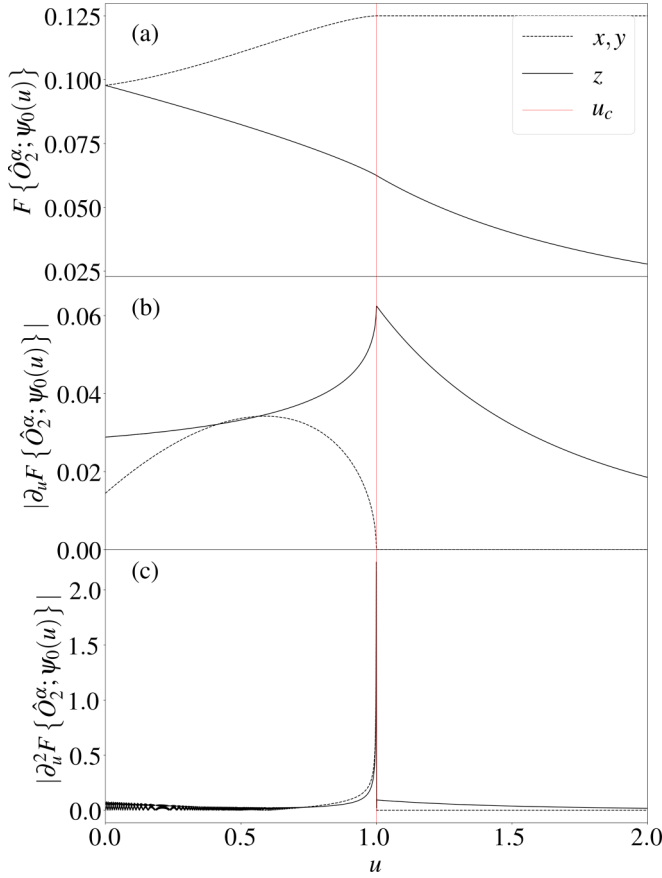
FIG. 4. QFI associated with the (a) bond correlation operator with (b) first and (c) second derivatives. The critical point is marked with a solid vertical red line. The second derivatives diverge, this time approaching the critical point from the left (the gapless phase).

Hamiltonian in the gapped phase is dominated by the Ising exchange on the z bonds. Consequently, the commutator between the Hamiltonian and the bond operator approaches zero in the limit of $u \to \infty$.
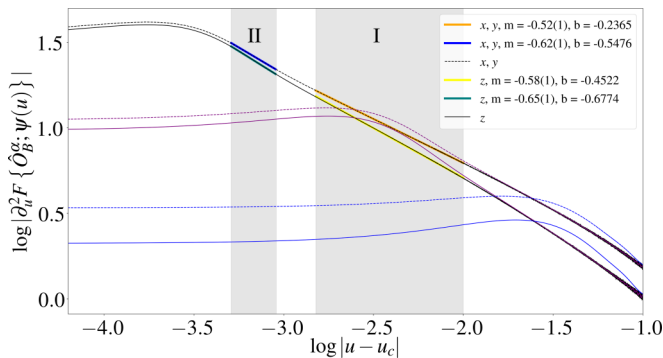

FIG. 5. Log-log plot of the second derivative of the QFI associated with the bond operator versus the distance from the critical point from the gapless phase ($u < 1$). Results are the black curve are for $L_x = L_y = 10^4$ with a line $\Delta u \sim 10^{-5}$. The purple and blue curves correspond to square geometries of size $L_x = L_y = 10^3$ and $L_x = L_y = 10^2$, respectively. The shaded regions (I) and (II) correspond to two regimes where we see linear scaling. The first region is valid for approximately the interval $10^{-1.9} > u > 10^{-2.8}$, while the second regime span approximately $10^{-3.0} > u > 10^{-3.3}$.

Assuming the same scaling ansatz as for the second derivative $F_{M,\alpha}$ we find a crossover between two scaling regimes. The first regime is given by the critical exponents

$$\Delta_{B,x}^{(I)} = \Delta_{B,y}^{(I)} \approx -0.52(1), \tag{20a}$$

$$\Delta_{B,z}^{(I)} \approx -0.58(1), \tag{20b}$$

which appears valid on the interval $10^{-1.9} > u > 10^{-2.8}$ and a second regime characterized by the exponents

$$\Delta_{B,x}^{(II)} = \Delta_{B,y}^{(II)} \approx -0.62(1), \tag{21a}$$

$$\Delta_{B,z}^{(II)} \approx -0.65(1), \tag{21b}$$

which appears to be valid on the interval $10^{-3.0} > u > 10^{-3.3}$. While the magnetization operator exhibits a divergence when approaching the critical point from the gapped phase, the bond operator exhibits a divergence approaching the critical point from the gapless phase.

The oscillatory behavior on the gapless side of the transitions for both QFI's is related to divergences in the QFI susceptibility due to points where the denominator of the integrand goes to zero. In the gapped phase these points are necessarily absent.

C. Diverging length scales

Using the results of the previous section we can determine the scaling of the divergence in the correlation length for $\langle c_{r_1,A} c_{r_2,B} \rangle$ (using the divergence in the magnetization operator), and for $\langle c_{r_1,A} c_{r_1,B} c_{r_2,A} c_{r_2,B} \rangle$.

In light of Eq. (11), we can now understand that the QFI susceptibility associated with the magnetization operator diverges from the gapped side due specifically to the divergence in that correlation function of the matter sector Majorana's. On the gapless side of the transition, the correlation function for the matter sector Majorana's is critical, and consequently the second derivative of Eq. (9) is given specifically by $\Xi(r, u)$ and contains no divergence.

Using Eq. (11), we may extract the scaling exponents for the correlation length of the matter sector correlation functions in the x and y, and z channels for $\partial_u^2 F_{M,\alpha}$,

$$\nu_{M,x} = \nu_{M,y} \approx 1.48(1), \tag{22a}$$

$$\nu_{M,z} \approx 1.50(1), \tag{22b}$$

and for the two scaling regimes of $\partial_u^2 F_{B,\alpha}$ for $u < u_c$. The first given by

$$\nu_{B,x}^{(I)} = \nu_{B,y}^{(I)} \approx 1.48(1), \tag{23a}$$

$$\nu_{B,z}^{(I)} \approx 1.42(1), \tag{23b}$$

and the second by

$$\nu_{B,x}^{(II)} = \nu_{B,y}^{(II)} \approx 1.38(1), \tag{24a}$$

$$\nu_{B,z}^{(II)} \approx 1.35(1). \tag{24b}$$

IV. CONCLUSION

We examined the QFI for the bond and magnetization operators in both the gapped and gapless phases of the KHM

and at the transition between these two phases for fully ferromagnetic and fully antiferromagnetic couplings. The second derivative of the QFI with respect to the magnetization operator is shown to diverge when approaching the phase transition from the gapped side like at a second order transition, while the QFI susceptibility approaching the critical point from the gapless side appears first order. Conversely, we find that the QFI susceptibility associated with the bond operator diverges like a second-order transition when approaching the critical point from the gapless side, and like a first-order transition when approaching the critical point from the gapped side.

In both cases, the divergences in the QFI susceptibility can be associated to diverging length scales in the two point correlators of the local generators of the QFI. For the particular case of the KHM, these divergences can be linked to diverging length scales in the matter sector Majorana's, even when the physical spin-spin correlation functions are truncated (as in the case of the two point correlation function). The implication is that the presence of the topological phase transition between the gapped and gapless phases may be detected experimentally at low temperatures.

There has been related work examining the Geometric phase associated with a twist operator acting on both sites [41]. We note that the critical exponents presented in Eq. (21b) for scaling regime (II) of the bond operators are within the margin of error of those in Ref. [41]. Geometrically, the QFI that we compute with respect to the bond operator is the diagonal component of the quantum geometric tensor [42]. The imaginary component of this tensor corresponds to the Berry curvature, while the real component corresponds to the notion of distance induced by the distinguishability of states. In Ref. [43], the connection between these two components of metric was discussed. The implication is that the geometry detected by the Berry phase is intimately related to the geometry of distinguishability, opening the prospect of experimentally measuring the Berry phase in condensed matter systems. Extracting the full quantum metric tensor has recently been achieved in cold atom systems [44].

The QFI associated with the magnetization operator in the fully antiferromagnetic phase is shown to be greater than for the fully ferromagnetic phase, as one would expect from the tendency of the antiferromagnetic coupling to produce spin singlets on the bonds. In the gapped phase defined by large K^γ coupling, the QFI associated with the bond operator converges to a constant value for the QFI generated by the transverse spin components (specifically the x and y components in our analysis).

It is shown in Ref. [20] that the QFI is proportional to the FS if the operator parametrizing the QFI is the same as the operator that generates the change in parameter for the ground state. This implies that the QFI for the bond operator from the gapless side of the transition is proportional the FS calculated in Ref. [17], however, we do not find this to be the case. This may be due to the fact that the ground state used in Ref. [17] differs from that used by Kitaev in Ref. [31], which is the one we employ here. Understanding the details of the connection between the QFI and the fidelity susceptibility warrants further investigation. We also note that the definition of the QFI may not be unique when a Hamiltonian possesses a degenerate ground-state manifold. In particular, one can

imagine a situation where the generator of the QFI lifts the degeneracy of this manifold, affecting the results. While in our calculation this ambiguity is not present in the gapped phase, it may affect the results in the gapless phase.

Future research is warranted to examine the behavior of the QFI at finite temperatures around the critical point, where the ground-state scaling will be modified by finite-temperature effects. The connection between the finite-temperature scaling and the length scale of the Majorana fermions in this case may offer insight into the details of candidate Kitaev spin liquid phases in materials where the pure Kitaev Hamiltonian is modifed by material relevant terms [40].

APPENDIX A: SCALING BEHAVIOR OF QFI SUSCEPTIBILITY

Let us work specifically on the case of pure states and unitary QFI. The generator of the QFI is most generally given by

$$\hat{O} = \sum_r \hat{O}_r, \tag{A1}$$

where $\hat{O}_r$ is an operator associated with the site located at r. We assume that r is contiguous and local, that is, it encompasses a finite number of degrees of freedom all lying within a distance ℓ from the site r. We consider a state ψ that depends on some parameter u that drives a phase transition at a value $u_c = 1$,

$$f\{\hat{O}, \psi(u)\} = \frac{1}{N} \sum_{r_1, r_2} \langle \hat{O}_{r_1} \hat{O}_{r_2} \rangle_\psi - \langle \hat{O}_{r_1} \rangle_\psi \langle \hat{O}_{r_2} \rangle_\psi$$

$$= \frac{1}{N} \sum_{r_1, r_2} C_{r_1, r_2}(u). \tag{A2}$$

Let us assume that the model is translation invariant and define $r := |r_1 - r_2|$. In general, we may assume that the connected correlation functions can be fit to the following form:

$$C_r(u) = \Xi(r, u) r^{-a} e^{-\frac{r}{\xi(u)}}, \tag{A3}$$

where a depends on the phase (i.e., is assumed independent of the driving parameter), and ξ is the correlation length, taken to be a function of the parameter u (we hereafter drop the explicit dependence). The function $\Xi(r, u)$ is assumed to be a smooth function of r and of the parameter u within a particular phase (though not necessarily smooth at the phase boundary). The divergence in the second derivative of the QFI must emerge from a divergence in the two point correlation functions. We therefore consider the second derivative of Eq. (9)

$$\partial_u^2 C_r(u) = \partial_u \left(\Xi(r, u) r^{1-a} \xi^{-2} \partial_u \xi e^{-\frac{r}{\xi}} + \partial_u \Xi(r, u) r^{-a} e^{-\frac{r}{\xi}} \right)$$

$$= -2 r^{1-a} \Xi(r, u) \xi^{-3} (\partial_u \xi)^2 e^{-\frac{r}{\xi}}$$

$$+ r^{1-a} \Xi(r, u) \xi^{-2} \partial_u^2 \xi e^{-\frac{r}{\xi}}$$

$$+ r^{2-a} \Xi(r, u) \xi^{-4} (\partial_u \xi)^2 e^{-\frac{r}{\xi}} + \partial_u^2 \Xi(r, u) r^{-a} e^{-\frac{r}{\xi}}$$

$$+ \partial_u \Xi(r, u) r^{1-a} \xi^{-2} \partial_u \xi e^{-\frac{r}{\xi}}. \tag{A4}$$

Naively, the correlation length is expected to diverge at the critical point. Let $\tilde{u} = |u - u_c|$ be the distance from the critical

point. Then the correlation length goes as

$$\xi \sim \tilde{u}^{-\nu}. \tag{A5}$$

This ansatz may be used to infer the scaling relations for the derivatives of the correlation length

$$\partial_u \xi \sim -\nu \tilde{u}^{-(\nu+1)}, \tag{A6a}$$

$$\partial_u^2 \xi \sim \nu(\nu+1)\tilde{u}^{-(\nu+2)}. \tag{A6b}$$

Substituting this into Eq. (A4) gives

$$\begin{aligned}
\partial_u^2 C_r(u) = & -2\Xi(r,u)r^{1-a}\tilde{u}^{3\nu}\nu^2\tilde{u}^{-2(\nu+1)}e^{-\frac{r}{\xi}} \\
& + \Xi(r,u)r^{1-a}\tilde{u}^{2\nu}\nu(\nu+1)\tilde{u}^{-(\nu+1)}e^{-\frac{r}{\xi}} \\
& + \Xi(r,u)r^{2-a}\tilde{u}^{4\nu}\nu^2\tilde{u}^{-2(\nu+1)}e^{-\frac{r}{\xi}} \\
& + \partial_u^2\Xi(r,u)r^{-a}e^{-\frac{r}{\xi}} + \partial_u\Xi(r,u)r^{1-a}\tilde{u}^{2\nu}(-\nu) \\
& \times \tilde{u}^{-(\nu+1)}e^{-\frac{r}{\xi}} \\
= & e^{-\frac{r}{\xi}}(-2\Xi(r,u)r^{1-a}\tilde{u}^{\nu-2}\nu^2 + \Xi(r,u)r^{1-a}\tilde{u}^{\nu-2} \\
& \times \nu(\nu+1) + \Xi(r,u)r^{2-a}\tilde{u}^{2\nu-2} + \partial_u^2\Xi(r,u)r^{-a} \\
& - \nu\partial_u\Xi(r,u)r^{1-a}\tilde{u}^{\nu-2}). \tag{A7}
\end{aligned}$$

We can now pull out the divergence associated with the proximity to the critical point

$$\begin{aligned}
\partial_u^2 C_r(u) = & \tilde{u}^{\nu-2}e^{-\frac{r}{\xi}}(-2\Xi(r,u)r^{1-a}\nu^2 + \Xi(r,u)r^{1-a}\nu(\nu+1) \\
& + \Xi(r,u)r^{2-a}\tilde{u}^\nu + \tilde{u}^{2-\nu}\partial_u^2\Xi(r,u)r^{-a} \\
& - \nu\partial_u\Xi(r,u)r^{1-a}). \tag{A8}
\end{aligned}$$

The scaling behavior of the QFI susceptibility is thus given by

$$\partial_u^2 f\{\hat{O},\psi\} = \tilde{u}^{\nu-2}\zeta(r,u). \tag{A9}$$

We define $\Delta_{\hat{O}} = \nu - 2$ as the scaling of the QFI with proximity to the critical point. The y-intercept on the log-log plot will be given by the nonuniversal function $\zeta(r,u)$.

APPENDIX B: CALCULATING VARIANCES

1. Solution of the Kitaev model

We adopt the approach of Refs. [39,45], where the Majorana degrees of freedom are recombined into Dirac fermions, with three *bond* fermions

$$b_{r,A}^\gamma = \frac{1}{2}\left(\beta_r^\gamma + \left(\beta_r^\gamma\right)^\dagger\right), \tag{B1a}$$

$$b_{r,B}^\gamma = \frac{1}{2i}\left(\beta_r^\gamma - \left(\beta_r^\gamma\right)^\dagger\right), \tag{B1b}$$

and one *matter* fermion

$$c_{r,A} = \tfrac{1}{2}(f_r + f_r^\dagger), \tag{B2a}$$

$$c_{r,B} = \tfrac{1}{2}(f_r - f_r^\dagger). \tag{B2b}$$

The bond fermions are not present in the Hamiltonian since we simply replace the bond operators with the eigenvalues of the standard gauge configuration

$(u_{j,k} = 1)$. The resulting Hamiltonian is quadratic in the matter fermions and translation invariant. It can be diagonalized first by mapping each matter fermion to momentum space, $f_r = \frac{1}{\sqrt{N}}\sum_q e^{iq\cdot r}f_q$, and then applying the Bogoliubov rotation, $f_q = \cos(\theta_q)a_q + i\sin(\theta_q)a_{-q}^\dagger$, where θ_q is defined by

$$\tan(2\theta_q) = \frac{K^x\cos(q_x) + K^y\cos(q_y) + K^z}{K^x\sin(q_x) + K^y\sin(q_y)}. \tag{B3}$$

2. Magnetization operator

Begin with

$$\hat{O}_{\text{Mag}}^\alpha = \sum_r \hat{S}_r^\alpha. \tag{B4}$$

The variance is given generally by

$$\langle(\Delta\hat{O})^2\rangle = \langle O^2\rangle - \langle O\rangle^2, \tag{B5}$$

which, for the magnetization operator, gives

$$\left\langle\left(\Delta\hat{O}_{\text{Mag}}^\alpha\right)^2\right\rangle = \sum_{r_1,r_2}\langle\hat{S}_{r_1}^\alpha\hat{S}_{r_2}^\alpha\rangle. \tag{B6}$$

Using translation invariance and converting the Majorana representation, this expression can be given as

$$\left\langle\left(\Delta\hat{O}_{\text{Mag}}^\alpha\right)^2\right\rangle = N\sum_r\langle\hat{S}_0^\alpha\hat{S}_r^\alpha\rangle. \tag{B7}$$

In the Kitaev model, the two-point correlator is zero for all values of r except nearest neighbors. Thus the sum above can be reduced to

$$\left\langle\left(\Delta\hat{O}_{\text{Mag}}^\alpha\right)^2\right\rangle = N\left(\tfrac{1}{4} + \langle\hat{S}_{0,A}^\alpha\hat{S}_{0,B}^\alpha\rangle\right). \tag{B8}$$

Thus we only need to calculate the nearest-neighbor correlation function

$$\begin{aligned}
\langle\hat{S}_{0,A}^\alpha\hat{S}_{0,B}^\alpha\rangle &= \frac{1}{4}\langle\sigma_{0,A}^\alpha\sigma_{0,B}^\alpha\rangle \\
&= \frac{1}{4}\langle(ib_{0,A}^\alpha c_{0,A})(ib_{0,B}^\alpha c_{0,B})\rangle \\
&= \frac{1}{4}\langle\mathcal{F}|b_{0,A}^\alpha b_{0,B}^\alpha|\mathcal{F}\rangle\langle\mathcal{M}|c_{0,A}c_{0,B}|\mathcal{M}\rangle \\
&= \frac{1}{4}\langle\mathcal{F}|(-i)(2\hat{n}_0^{\beta^\alpha}-1)|\mathcal{F}\rangle\langle\mathcal{M}|(-i)(2\hat{n}_0^f-1)|\mathcal{F}\rangle \\
&= -\frac{1}{4}(2\langle\hat{n}_0^f\rangle-1) \\
&= -\frac{1}{4}\left(2\frac{1}{N}\sum_{q_1,q_2}\langle f_{q_1}^\dagger f_{q_2}\rangle-1\right) \\
&= -\frac{1}{4}\left(\frac{2}{N}\sum_q\sin^2(\theta_q)-1\right). \tag{B9}
\end{aligned}$$

The QFI density is four times the variance divided by the system size. Thus

$$f\{\hat{O}^\alpha_{\text{Mag}}\} = 1 + \langle \sigma^\alpha_{0,A} \sigma^\alpha_{0,B} \rangle. \tag{B10}$$

3. Bond operator

$$\text{Var}(\hat{O}^\alpha_{\text{2-Site}}) = \langle (\hat{O}^\alpha_{\text{2-Site}})^2 \rangle - \langle \hat{O}^\alpha_{\text{2-Site}} \rangle^2$$

$$= \sum_{r_1,r_2} \langle \hat{S}^\alpha_{r_1A} \hat{S}^\alpha_{r_1B} \hat{S}^\alpha_{r_2A} \hat{S}^\alpha_{r_2A} \rangle - \left(\sum_r \hat{S}^\alpha_{r_1A} \hat{S}^\alpha_{r_1B} \right)^2$$

$$= \frac{1}{16} \left(\sum_{r_1,r_2} \langle b^\alpha_{r_1A} b^\alpha_{r_1B} b^\alpha_{r_2A} b^\alpha_{r_2B} \rangle \langle c_{r_1A} c_{r_1B} c_{r_2A} c_{r_2B} \rangle \right.$$

$$\left. - \left(\sum_r -\langle b^\alpha_{rA} b^\alpha_{rB} \rangle \langle c_{rA} c_{rB} \rangle \right)^2 \right). \tag{B11}$$

We can compute the flux sector expectation values easily

$$\langle b^\alpha_{r_1A} b^\alpha_{r_1B} b^\alpha_{r_2A} b^\alpha_{r_2B} \rangle = (-i)^2 \langle (\beta_{r_1} + \beta^\dagger_{r_1})(\beta_{r_1} - \beta^\dagger_{r_1})(\beta_{r_2} + \beta^\dagger_{r_2})$$

$$\times (\beta_{r_2} - \beta^\dagger_{r_2}) \rangle$$

$$= -\langle (2n_{r_1} - 1)(2n_{r_2} - 1) \rangle$$

$$= -1, \tag{B12}$$

where the last line follows from the fact that the ground state in the standard flux configuration is defined by $u_r = 2n_r - 1 = 1$. Similarly we find

$$\langle b^\alpha_{rA} b^\alpha_{rB} \rangle = (-i)\langle (2n_r - 1) \rangle$$

$$= (-i). \tag{B13}$$

The variance is therefore

$$\text{Var}(\hat{O}^\alpha_{\text{2-Site}}) = \frac{1}{16} \left(\sum_{r_1,r_2} (-1)\langle c_{r_1A} c_{r_1B} c_{r_2A} c_{r_2B} \rangle - \left(\sum_r (i)\langle c_{rA} c_{rB} \rangle \right)^2 \right)$$

$$= \frac{1}{16} \left(-\sum_{r_1,r_2} \langle c_{r_1A} c_{r_1B} c_{r_2A} c_{r_2B} \rangle + \sum_{r_1,r_2} \langle c_{r_1A} c_{r_1B} \rangle \langle c_{r_2A} c_{r_2B} \rangle \right)$$

$$= \frac{1}{16} \left(\sum_{r_1,r_2} -\langle c_{r_1A} c_{r_1B} \rangle \langle c_{r_2A} c_{r_2B} \rangle + \langle c_{r_1A} c_{r_2A} \rangle \langle c_{r_1B} c_{r_2B} \rangle - \langle c_{r_1A} c_{r_2B} \rangle \langle c_{r_1B} c_{r_2A} \rangle \langle c_{r_1A} c_{r_1B} \rangle \langle c_{r_2A} c_{r_2B} \rangle \right)$$

$$= \frac{1}{16} \left(\sum_{r_1,r_2} \langle c_{r_1A} c_{r_2A} \rangle \langle c_{r_1B} c_{r_2B} \rangle - \langle c_{r_1A} c_{r_2B} \rangle \langle c_{r_1B} c_{r_2A} \rangle \right). \tag{B14}$$

We now need only evaluate the two point correlators above. For the first term we have

$$\langle c_{r_1A} c_{r_2A} \rangle = \frac{1}{N} \sum_{q_1,q_2} e^{iq_1 r_1} e^{iq_2 r_2} \langle (f_{q_1} + f^\dagger_{q_1}) \rangle \langle (f_{q_2} + f^\dagger_{q_2}) \rangle$$

$$= \frac{1}{N} \sum_{q_1,q_2} e^{iq_1 r_1} e^{iq_2 r_2} \langle f_{q_1} f_{q_2} + f_{q_1} f^\dagger_{q_2} + f^\dagger_{q_1} f_{q_2}$$

$$+ f^\dagger_{q_1} f^\dagger_{q_2} \rangle$$

$$= \frac{1}{N} \sum_{q_1,q_2} e^{iq_1 r_1} e^{iq_2 r_2} \langle f_{q_1} f_{q_2} + f^\dagger_{q_1} f^\dagger_{q_2} + \delta_{q_1,q_2} \rangle. \tag{B15}$$

We can see that

$$\langle f_{q_1} f_{q_2} \rangle = i \cos(\theta_{q_1}) \sin(\theta_{q_2}) \langle a_{q_1} a^\dagger_{-q_2} \rangle$$

$$= i \cos(\theta_{q_1}) \sin(\theta_{q_2}) \delta_{q_1,-q_2},$$

$$\langle f^\dagger_{q_1} f^\dagger_{q_2} \rangle = (-i) \cos(\theta_{q_1}) \sin(\theta_{q_2}) \langle a_{-q_1} a^\dagger_{q_2} \rangle$$

$$= (-i) \cos(\theta_{q_1}) \sin(\theta_{q_2}) \delta_{-q_1,q_2}. \tag{B16}$$

Consequently,

$$\langle c_{r_1A} c_{r_2A} \rangle = \frac{1}{N} \sum_{q_1,q_2} e^{iq_1 r_1} e^{iq_2 r_2} \delta_{q_1,q_2}$$

$$= \frac{1}{N} \sum_q e^{iq(r_1 - r_2)} = \delta_{r_1,r_2}. \tag{B17}$$

Similarly we may show that

$$\langle c_{r_1B} c_{r_2B} \rangle = \delta_{r_1,r_2}. \tag{B18}$$

For the second term we begin with

$$\langle c_{r_1 A} c_{r_2 B} \rangle = \frac{1}{N} \sum_{q_1, q_2} e^{iq_1 r_1} e^{iq_2 r_2} (-i) \langle (f_{q_1} + f_{q_1}^\dagger)(f_{q_2} - f_{q_2}^\dagger) \rangle$$

$$= \frac{1}{N} \sum_{q_1, q_2} e^{iq_1 r_1} e^{iq_2 r_2} (-i) \langle f_{q_1} f_{q_2} - f_{q_1} f_{q_2}^\dagger + f_{q_1}^\dagger f_{q_2} - f_{q_1}^\dagger f_{q_2}^\dagger \rangle$$

$$= \frac{(-i)}{N} \sum_{q_1, q_2} e^{iq_1 r_1} e^{iq_2 r_2} \left(\langle f_{q_1} f_{q_2} - f_{q_1}^\dagger f_{q_2}^\dagger + f_{q_1}^\dagger f_{q_2} - f_{q_1} f_{q_2}^\dagger \rangle \right)$$

$$= \frac{(-i)}{N} \sum_{q_1, q_2} e^{iq_1 r_1} e^{iq_2 r_2} \left(\langle f_{q_1} f_{q_2} - f_{q_1}^\dagger f_{q_2}^\dagger \rangle + \langle 2 f_{q_1}^\dagger f_{q_2} - 1 \rangle \right)$$

$$= \frac{(-i)}{N} \sum_{q_1, q_2} e^{iq_1 r_1} e^{iq_2 r_2} \left[i \cos(\theta_{q_1}) \sin(\theta_{q_2})(\delta_{q_1, -q_2} + \delta_{-q_1, q_2}) + 2 \sin(\theta_{q_1}) \sin(\theta_{q_2}) \delta_{q_1, q_2} - 1 \right]$$

$$= \frac{(-i)}{N} \sum_q 2i e^{-iq(r_1 - r_2)} \cos(\theta_q) \sin(\theta_q) + \frac{(-i)}{N} \sum_q [2 \sin^2(\theta_q) - 1]$$

$$= \frac{1}{N} \sum_q e^{-iq(r_1 - r_2)} 2 \cos(\theta_q) \sin(\theta_q) + \frac{i}{N} \sum_q e^{iq(r_1 + r_2)} \cos(2\theta_q)$$

$$= \frac{1}{N} \sum_q e^{-iq(r_1 - r_2)} \sin(2\theta_q) + \frac{i}{N} \sum_q e^{iq(r_1 + r_2)} \cos(2\theta_q). \tag{B19}$$

The final two-point correlator is given by

$$\langle c_{r_1 B} c_{r_2 A} \rangle = \frac{1}{N} \sum_{q_1, q_2} e^{iq_1 r_1} e^{iq_2 r_2} (-i) \langle (f_{q_1} - f_{q_1}^\dagger)(f_{q_2} + f_{q_2}^\dagger) \rangle$$

$$= \frac{(-i)}{N} \sum_{q_1, q_2} e^{iq_1 r_1} e^{iq_2 r_2} \left(\langle f_{q_1} f_{q_2} - f_{q_1}^\dagger f_{q_2}^\dagger \rangle - \langle 2 f_{q_1}^\dagger f_{q_2} - 1 \rangle \right)$$

$$= \frac{(-i)}{N} \sum_{q_1, q_2} e^{iq_1 r_1} e^{iq_2 r_2} \left[i \cos(\theta_{q_1}) \sin(\theta_{q_2})(\delta_{q_1, -q_2} + \delta_{-q_1, q_2}) - [2 \sin(\theta_{q_1}) \sin(\theta_{q_2}) \delta_{q_1, q_2} - 1] \right]$$

$$= \frac{(-i)}{N} \sum_q 2i e^{-iq(r_1 - r_2)} \cos(\theta_q) \sin(\theta_q) - \frac{(-i)}{N} \sum_q e^{iq(r_1 + r_2)} [2 \sin^2(\theta_q) - 1]$$

$$= \frac{1}{N} \sum_q e^{-iq(r_1 - r_2)} \sin(2\theta_q) - \frac{i}{N} \sum_q e^{iq(r_1 + r_2)} \cos(2\theta_q). \tag{B20}$$

The final term is therefore a product of differences

$$\langle c_{r_1 B} c_{r_2 A} \rangle \langle c_{r_1 A} c_{r_2 B} \rangle = \frac{1}{N^2} \sum_{q_1, q_2} \left[e^{-i(q_1 + q_2)(r_1 - r_2)} \sin(2\theta_{q_1}) \sin(2\theta_{q_2}) + e^{i(q_1 + q_2)(r_1 + r_2)} \cos(2\theta_{q_1}) \cos(2\theta_{q_2}) \right]$$

$$= \frac{1}{N^2} \sum_{q_1, q_2} \left[e^{ir_1(q_1 + q_2)} e^{-ir_2(q_1 + q_2)} \sin(2\theta_{q_1}) \sin(2\theta_{q_2}) + e^{ir_1(q_1 + q_2)} e^{ir_2(q_1 + q_2)} \cos(2\theta_{q_1}) \cos(2\theta_{q_2}) \right]. \tag{B21}$$

Under the summation, we may extract the delta functions

$$\sum_{r_1, r_2} \langle c_{r_1 B} c_{r_2 A} \rangle \langle c_{r_1 A} c_{r_2 B} \rangle = \frac{1}{N} \sum_{r_2} \sum_{q_1, q_2} \delta_{q_1, -q_2} e^{-ir_2(q_1 + q_2)} \sin(2\theta_{q_1}) \sin(2\theta_{q_2}) + \delta_{q_1, -q_2} e^{ir_2(q_1 + q_2)} \cos(2\theta_{q_1}) \cos(2\theta_{q_2})$$

$$= \sum_q \cos^2(2\theta_q) - \sin^2(2\theta_q). \tag{B22}$$

We are now ready to return to our original expression for the variance which reads

$$\text{Var}\big(\hat{O}^{\alpha}_{\text{2-Site}}\big) = \frac{1}{16}\left(N - \sum_q [\cos^2(2\theta_q) - \sin^2(2\theta_q)]\right)$$

$$= \frac{1}{16}\sum_q [1 - \cos^2(2\theta_q) + \sin^2(2\theta_q)]$$

$$= \frac{1}{8}\sum_q \sin^2(2\theta_q). \tag{B23}$$

Thus the associated QFI density is

$$\mathcal{F}\big(\hat{O}^{\alpha}_{\text{2-Site}}\big) = 4\frac{\text{Var}\big(\hat{O}^{\alpha}_{\text{2-Site}}\big)}{N} = \frac{1}{2}\frac{1}{N}\sum_q \sin^2(\theta_q), \tag{B24}$$

passing to the continuum limit we find

$$\mathcal{F}\big(\hat{O}^{\alpha}_{\text{2-Site}}\big) = \frac{1}{2}\int_{\text{BZ}} \sin^2(2\theta_q)d^2q. \tag{B25}$$

APPENDIX C: DERIVATIVES OF THE QFI SUSCEPTIBILITY MOMENTUM DENSITY

To gain more insight into the divergence in $F_{M,\alpha}$, we define the QFI *momentum density* for the magnetization operator, $f_{M,\alpha}$ via

$$F_{M,\alpha} = \sum_q \left(\frac{1}{N} - \cos(2\theta_q)\right) = \sum_q f_{M,\alpha}(q;u). \tag{C1}$$

We may explicitly evaluate the first and second derivatives of this quantity for each spin component, giving

$$\partial_u f_{M,x} = \frac{\Delta_x^2 \cos(q_y) - \varepsilon_x \Delta_x \sin(q_y)}{\big(\varepsilon_x^2 + \Delta_x^2\big)^{\frac{3}{2}}}, \tag{C2a}$$

$$\partial_u f_{M,y} = \frac{\Delta_y^2 \cos(q_x) - \varepsilon_y \Delta_y \sin(q_x)}{\big(\varepsilon_y^2 + \Delta_y^2\big)^{\frac{3}{2}}}, \tag{C2b}$$

$$\partial_u f_{M,z} = \frac{\Delta_z^2}{\big(\varepsilon_z^2 + \Delta_z^2\big)^{\frac{3}{2}}}, \tag{C2c}$$

for the first derivatives, and

$$\partial_u^2 f_{M,x} = \frac{-3\varepsilon_x \Delta_x^2 \cos^2(q_y) + \Delta_x\big[3\big(\varepsilon_x^2 - \Delta_x^2\big) + \varepsilon_x + \Delta_x\big]\sin(q_y)\cos(q_y) + \varepsilon_x\big(2\Delta_x^2 - \varepsilon_x^2\big)\sin^2(q_y)}{\big(\varepsilon_x^2 + \Delta_x^2\big)^{\frac{5}{2}}}, \tag{C3a}$$

$$\partial_u^2 f_{M,y} = \frac{-3\varepsilon_y \Delta_y^2 \cos^2(q_x) + \Delta_y\big[3\big(\varepsilon_y^2 - \Delta_y^2\big) + \varepsilon_y + \Delta_y\big]\sin(q_x)\cos(q_x) + \varepsilon_y\big(2\Delta_y^2 - \varepsilon_y^2\big)\sin^2(q_x)}{\big(\varepsilon_y^2 + \Delta_y^2\big)^{\frac{5}{2}}}, \tag{C3b}$$

$$\partial_u^2 f_{M,z} = \frac{-3\varepsilon_z \Delta_z^2}{\big(\varepsilon_z^2 + \Delta_z^2\big)^{\frac{5}{2}}}, \tag{C3c}$$

for the second derivatives. We again compute explicitly the first and second derivatives of the QFI with respect to the driving parameter by rewriting the QFI in terms of an integral over a QFI density

$$F_{B,\alpha} = \int_{\text{BZ}} f_{B,\alpha}(q;u)$$

finding

$$\partial_u f_{B,x} = \frac{\Delta_x \varepsilon_x [\varepsilon_x \sin(q_y) - \Delta_x \cos(q_y)]}{\big(\varepsilon_x^2 + \Delta_x^2\big)^2}, \tag{C4a}$$

$$\partial_u f_{B,y} = \frac{\Delta_y \varepsilon_y [\varepsilon_y \sin(q_x) - \Delta_y \cos(q_x)]}{\big(\varepsilon_y^2 + \Delta_y^2\big)^2}, \tag{C4b}$$

$$\partial_u f_{B,z} = \frac{\Delta_z^2 \varepsilon_z}{\big(\varepsilon_z^2 + \Delta_z^2\big)^2}, \tag{C4c}$$

for the first derivatives and

$$\partial_u^2 f_{B,x} = \frac{[\varepsilon_x \sin(q_y) - \Delta_x \cos(q_y)]\big(\big[\Delta_x^2 - 3\varepsilon_x^2\big]\Delta_x \cos(q_y) + \big(\varepsilon_x^2 - 3\Delta_x^2\big)\varepsilon_x \sin(q_y)\big)}{\big(\varepsilon_x^2 + \Delta_x^2\big)^3}, \tag{C5a}$$

$$\partial_u^2 f_{B,y} = \frac{[\varepsilon_y \sin(q_x) - \Delta_y \cos(q_x)]\big(\big[\Delta_y^2 - 3\varepsilon_y^2\big]\Delta_y \cos(q_x) + \big(\varepsilon_y^2 - 3\Delta_y^2\big)\varepsilon_y \sin(q_x)\big)}{\big(\varepsilon_y^2 + \Delta_y^2\big)^3}, \tag{C5b}$$

$$\partial_u^2 f_{B,z} = \frac{\Delta_z^2\big(\Delta_z^2 - 3\varepsilon_z^2\big)}{\big(\varepsilon_z^2 + \Delta_z^2\big)^3}. \tag{C5c}$$

[1] D. Petz and C. Sudár, J. Math. Phys. **37**, 2662 (1996).

[2] D. Petz, J. Phys. A: Math. Gen. **35**, 929 (2002).

[3] M. G. A. Paris, Int. J. Quantum. Inform. **07**, 125 (2009).

[4] G. Tóth, Phys. Rev. A **85**, 022322 (2012).

[5] G. Tóth and D. Petz, Phys. Rev. A **87**, 032324 (2013).

[6] G. Tóth and I. Apellaniz, J. Phys. A: Math. Theor. **47**, 424006 (2014).

[7] A. S. Holevo, *Statistical Structure of Quantum Theory* (Springer Science & Business Media, New York, 2003), Vol. 67.

[8] I. Bengtsson and K. Życzkowski, *Geometry of Quantum States: An Introduction to Quantum Entanglement* (Cambridge University Press, Cambridge, England, 2017).

[9] W. K. Wootters, Phys. Rev. D **23**, 357 (1981).

[10] S. L. Braunstein and C. M. Caves, Phys. Rev. Lett. **72**, 3439 (1994).

[11] P. Zanardi, P. Giorda, and M. Cozzini, Phys. Rev. Lett. **99**, 100603 (2007).

[12] P. Hauke, L. Tagliacozzo, and P. Zoller, Nat. Phys. **12**, 778 (2016).

[13] W.-F. Liu, J. Ma, and X. Wang, J. Phys. A: Math. Theor. **46**, 045302 (2013).

[14] Q. Zheng, Y. Yao, and X.-W. Xu, Commun. Theor. Phys. **63**, 279 (2015).

[15] J. Ma and X. Wang, Phys. Rev. A **80**, 012318 (2009).

[16] J. Lambert and E. S. Sørensen, Phys. Rev. B **99**, 045117 (2019).

[17] S. Yang, S.-J. Gu, C.-P. Sun, and H.-Q. Lin, Phys. Rev. A **78**, 012304 (2008).

[18] R. Jafari and A. Akbari, Phys. Rev. A **101**, 062105 (2020).

[19] P. Zanardi and N. Paunković, Phys. Rev. E **74**, 031123 (2006).

[20] J. Liu, H.-N. Xiong, F. Song, and X. Wang, Physica A **410**, 167 (2014).

[21] L. Pezze, M. Gabbrielli, L. Lepori, and A. Smerzi, Phys. Rev. Lett. **119**, 250401 (2017).

[22] P. Hyllus, W. Laskowski, R. Krischek, C. Schwemmer, W. Wieczorek, H. Weinfurter, L. Pezzé, and A. Smerzi, Phys. Rev. A **85**, 022321 (2012).

[23] L. Pezzé and A. Smerzi, Phys. Rev. Lett. **102**, 100401 (2009).

[24] M. Gabbrielli, A. Smerzi, and L. Pezzè, Sci. Rep. **8**, 15663 (2018).

[25] M. Cramer, M. B. Plenio, and H. Wunderlich, Phys. Rev. Lett. **106**, 020401 (2011).

[26] P. Krammer, H. Kampermann, D. Bruß, R. A. Bertlmann, L. C. Kwek, and C. Macchiavello, Phys. Rev. Lett. **103**, 100502 (2009).

[27] O. Marty, M. Epping, H. Kampermann, D. Bruß, M. B. Plenio, and M. Cramer, Phys. Rev. B **89**, 125117 (2014).

[28] I. Frérot and T. Roscilde, Phys. Rev. B **94**, 075121 (2016).

[29] L. Savary and L. Balents, Rep. Prog. Phys. **80**, 016502 (2016).

[30] X.-G. Wen, Phys. Rev. B **65**, 165113 (2002).

[31] A. Kitaev, Ann. Phys. (NY) **321**, 2 (2006), January Special Issue.

[32] Q. Chen, G.-Q. Zhang, J.-Q. Cheng, and J.-B. Xu, Quant. Info. Proc. **18**, 8 (2019).

[33] J. Cui, J.-P. Cao, and H. Fan, Phys. Rev. A **82**, 022319 (2010).

[34] D. F. Abasto and P. Zanardi, Phys. Rev. A **79**, 012321 (2009).

[35] F. J. Burnell and C. Nayak, Phys. Rev. B **84**, 125125 (2011).

[36] D. A. S. Kaib, S. M. Winter, and R. Valentí, Phys. Rev. B **100**, 144445 (2019).

[37] M. Kardar, *Statistical Physics of Fields* (Cambridge University Press, Cambridge, England, 2007).

[38] E. H. Lieb, in *Condensed Matter Physics and Exactly Soluble Models* (Springer, New York, 2004), pp. 79–82.

[39] G. Baskaran, S. Mandal, and R. Shankar, Phys. Rev. Lett. **98**, 247201 (2007).

[40] J. G. Rau, E. K.-H. Lee, and H.-Y. Kee, Phys. Rev. Lett. **112**, 077204 (2014).

[41] J. Lian, J.-Q. Liang, and G. Chen, Eur. Phys. J. B **85**, 207 (2012).

[42] J. Provost and G. Vallee, Commun. Math. Phys. **76**, 289 (1980).

[43] G. Palumbo and N. Goldman, Phys. Rev. Lett. **121**, 170401 (2018).

[44] X. Tan, D.-W. Zhang, Z. Yang, J. Chu, Y.-Q. Zhu, D. Li, X. Yang, S. Song, Z. Han, Z. Li, Y. Dong, H.-F. Yu, H. Yan, S.-L. Zhu, and Y. Yu, Phys. Rev. Lett. **122**, 210401 (2019).

[45] J. Knolle, D. L. Kovrizhin, J. T. Chalker, and R. Moessner, Phys. Rev. B **92**, 115127 (2015).

Chapter 4

State Space Curvature and Entanglement

State Space Geometry of the Spin-1 Antiferromagnetic Heisenberg Chain

James Lambert[1, *] and Erik S. Sørensen[1, †]

[1]*Department of Physics & Astronomy, McMaster University 1280 Main St. W., Hamilton ON L8S 4M1, Canada*
(Dated: October 21, 2022)

We study the phase diagram of the spin-1 antiferromagnetic Heisenberg chain with uniaxial anisotropy and applied magnetic field in terms of the genuine multipartite entanglement as witnessed by the mean quantum Fisher information density. By generalizing the manifold studied in [1] to the many body case for spin 1, we connect the state space curvature in the vicinity of the ground state of the Heisenberg chain to the genuine multipartite entanglement. Our analysis demonstrates that the quantum critical points and SPT phase exhibit large positive state space curvature. We further show that the entanglement in the SPT phase is enhanced by the presence of uniaxial anisotropy, and undiminished in the presence of uniform magnetic fields. The magnon condensate phase induced by large fields is shown to emanate from the Gaussian critical point, and exhibits massive multipartite entanglement over a robust region of the parameter space.

I. INTRODUCTION

The degree to which two probability distributions may be distinguished from one another in some fixed set of measurements induces a natural notion of distance on the state space [2]. This notion of distance and the geometrical structure it gives rise to is sometimes termed *information geometry*, with distinguishability being quantified by the Fisher information matrix,

$$F_{\mu\nu}\{p(x|\lambda)\} = \int \frac{1}{p} \frac{\partial p}{\partial \lambda_\mu} \frac{\partial p}{\partial \lambda_\nu} \mathrm{d}x, \qquad (1)$$

where $p(x|\lambda)$ is a probability distribution (which we hereafter refer to as a state) that depends on some parameterization, $\vec{\lambda}$, of the state space. $F_{\mu\nu}$ quantifies how distinguishable the distribution $p(x|\vec{\lambda})$ is from the distribution, $p(x|\lambda + \mathrm{d}\lambda)$ [3]. The quantum generalization holds for both pure [4] and mixed [5] states, and is termed quantum Fisher information (QFI) with the density matrix $\hat{\rho}$ taking the place of $p(x|\lambda)$, and the quantum expectation value replacing the integral. The associated geometrical structure is termed *quantum information geometry* or simply *quantum geometry* (see [6] for a complete introduction to the subject). In this work we are specifically interested in the case of pure states of spin-S with unitary parameterizations, for which the QFI matrix is proportional to the connected covariance [7],

$$Q_{\mu\nu}\{\psi\} = \frac{A}{S^2}\mathrm{Cov}_\psi(\Lambda_\mu, \Lambda_\nu) \qquad (2)$$

where,

$$\mathrm{Cov}_\psi(\Lambda_\mu, \Lambda_\nu) = \langle \Lambda_\mu \Lambda_\nu \rangle - \langle \Lambda_\mu \rangle \langle \Lambda_\nu \rangle$$

with Λ_μ and Λ_ν the hermitian operators that generate the unitary parameterization for the state $|\psi\rangle$ via,

$$|\psi(\lambda)\rangle = e^{-i\lambda\Lambda} |\psi\rangle, \qquad (3)$$

* lambej3@mcmaster.ca
† sorensen@mcmaster.ca

The constant, A, hereafter the *metric constant*, may be thought of as a normalization (see Sec. I A). The QFI matrix can be decomposed into a real, symmetric, Riemannian metric g [8], and an anti-symmetric symplectic tensor Γ (the Berry curvature [9]),

$$Q_{\mu\nu} = g_{\mu\nu} + i\Gamma_{\mu\nu}, \qquad (4)$$

While the trace of the QFI matrix for a suitable choice of parameterization obeys the following bound [10, 11],

$$\bar{f} := \frac{1}{3N} \mathrm{Tr}\{Q\} > 2mA. \qquad (5)$$

for states that are $(m + 1)$-partite entangled.

In this work, we calculate the QFI matrix associated with the staggered magnetization operator, and map out the phase diagram of the spin-1 antiferromagnetic Heisenberg chain as a function of a uniform applied field and the uniaxial anisotropy. Using the metric g, hereafter the *quantum metric*, we compute the volumes of spheres parameterized by the strength and orientation of a staggered magnetic field. By computing the scaling of these spheres with radius, we compute the curvature of the state space in the vicinity of the ground state, demonstrating that the entanglement in the SPT Haldane phase and at the critical points appears to be associated with the presence of positive curvature in the state space, thus demonstrating a connection between entanglement and state space curvature.

Since the QFI quantifies the distinguishability of probability distributions, it can be naturally expressed in terms of the dynamical response, of which Eq. 2 is the zero temperature limit [12, 13]. This has allowed for the direct measurement of GME in recent inelastic neutron scattering experiments [11, 14].

The QFI matrix plays a central role in quantum metrology and parameter estimation. It also appears in the generalizations of the uncertainty relation that allow for the formulation of the time-energy uncertainty principle (time having no associated Hermitian operator and thus being a parameter that must be inferred by other measurements) [15, 16]. Most importantly for our purposes, the mean trace of the QFI matrix quantifies the

degree to which the state ψ has genuine multipartite entanglement (GME) [10]. This connection is especially interesting as it holds even at finite temperatures [17] (we discuss the details in Sec. III A). Entries of the QFI matrix have now been studied in a wide range of models [18–25]. These studies have emphasized either parameterizations that are linear in the spin degrees of freedom, or in the case of [25], parameterizations using non-local operators that exhibit super extensive scaling in topologically non trivial phases. The full QFI matrix that would correspond to these parameterizations has been relatively less explored.

The proof connecting the QFI to GME is for operators linear in the spin degrees of freedom [10]. This is advantageous from the perspective of response function experiments, since in a typical scattering experiment one imagines that that scattering beam is exploring the response of the state to an applied operator that is often linear in the local degrees of freedom. From a theoretical perspective, however, we can explore parameterizations corresponding to a wide range of operators which would not necessarily be linear in the local degrees of freedom and hence have no established connection to the GME. For instance, the fidelity susceptibility (FS) [26–29] is identical to the QFI up to a constant of proportionality [30]. In this context one considers the overlap in the ground state of a Hamiltonian depending on a parameter λ with the ground state at $\lambda + d\lambda$, where the parameter coupled to λ might be non-local in the spin degrees of freedom. Thus, the FS is not generally known to have a relationship with the GME. An analogous relationship to response functions holds true of the FS [31].

In the context where quantum geometry is studied for driving parameters of the Hamiltonian one tends to talk about the quantum geometric tensor (QGT) [32], the entries of which are the FS and which, away from level crossings, is the same object as the QFI matrix defined in Eq. 2. The form of the QFI matrix in terms of the covariance may thus be thought of as an adiabatic form of the QFI [7]. In the vicinity of the critical point the QGT and QFI matrix display different scaling relationships [12, 32]. In this work we focus on the QFI matrix in this adiabatic form, since determining the entire spectrum is generally a very hard problem for all but a handful of exactly solvable models. If, however, the operators generating the transformations are relevant in a renormalization group sense then both the QFI and QGT will exhibit divergences at the critical point.

The Hilbert space of a many body system is exponentially large in the number of degrees of freedom. Computing the QFI matrix for a complete parameterization of such a space is intractable. Studying quantum geometry in the many body context therefore relies on the judicious choice of a lower dimensional slice of the state space. Different systems call for different choices of parameterization, and we identify two broad categories of approach in the literature.

First, in the context of topological insulators and band systems, it is natural to examine the state space from the perspective of the Brillouin zone geometry of the bands. Such insulators are, after all, characterized by their integrated Berry curvature, or Chern number [33]. Recently, the Riemannian component of the QGT, $g_{\mu\nu}$ has been shown to also indicate the presence of topologically non-trivial band structures via calculations of the Euler characteristic [23, 34–36]. This approach has allowed for a general classification of the Euler characteristic of N level systems from the intuitive perspective of Bloch-hyperspheres (generalizing the familiar 2D Bloch sphere) [37].

The second approach is to consider a state space manifold composed of some combination of Hamiltonian parameters that drive the phase transitions, along with rotations of the local degrees of freedom [26, 27, 32, 38–41].

The QFI matrix and QGT have been theoretically examined in a wide range of models, including Andreev states [42], magnetic systems at finite temperature [39] the Lipkin-Meshkov-Glick model [41], the Dicke model[43], photonic systems [44], and in quantum dot chains [45]. This in turn has given rise to a recent surge of experimental investigations in planar micro cavities [46], superconducting qubits [47], Hall systems [48], and simple qubits formed at the NV center of diamond [1].

In this work we introduce a generalization, specifically for many body spin systems, of the Hilbert space manifold considered in [1] to the case of spin-1. Our construction is directly relevant for inelastic neutron scattering experiments and relies on a linear operator parameterization, allowing us to employ the bound in Eq. 5 to detect genuine multipartite entanglement. Previous studies of the quantum geometry of spin systems tend to emphasize the geometry of the state space manifold as parameterized by the driving parameters of the phase transitions. By contrast, the manifold that we introduce could be applied consistently to any spin system, regardless of the particular operators that drive the transitions. Using the mean QFI density for a staggered magnetic field, we first construct a map of the multipartite entanglement for the spin-1 antiferromagnetic Heisenberg chain with uniaxial anisotropy, D, and applied magnetic field oriented along the z axis, B_z (see Sec. I B). Subsequently, using the quantum metric, we calculate the volume of a two dimensional slice of state space parameterized by the orientation of a perturbatively small staggered magnetic field. By taking the ratio of the volume of this slice of state space in the vicinity of the ground state to the volume of a sphere in a flat state space (see II for our definition of flat), we compute the local curvature in the quantum state space. The Haldane phase appears to be characterized by the presence of a large positive curvature, while the trivial insulator phase and Néel phase appear to be flat.

In the remainder of the introduction we expand our discussion of the QFI and its quantitative relationship to GME. We also review the relevant details of the spin-1 antiferromagnetic Heisenberg chain, which we use as a

test case. In Sec. II we introduce our generalization of the construction in [49] and the notions of quantum volume and quantum curvature. The results of our analysis of the Heisenberg chain are presented in III with concluding remarks given in IV.

A. Quantum Fisher Information

The relationship between the QFI and genuine multi-partite entanglement is derived in [10]. In that work a linear spin operator of the form,

$$\Lambda_{\hat{n}_r} = \sum_r \hat{n}_r \cdot \vec{S}_r, \qquad (6)$$

is considered, where $\hat{n}$ is a unit vector whose orientation may, in the most general case, be site dependent. We call Eq. 6 the *generator* of the QFI. In choosing these generators, the key point is that not all generators relative orientation are equivalent. If the generator commutes with the Hamiltonian, then the ground state will be an eigenstate of the generator, and the covariance, and hence the QFI, will be zero. We discuss the implications of this fact for the spin-1 Heisenberg chain more in Sec. II. The generator that will detect the greatest QFI is the one for which $[H, \Lambda]$ is maximal. Often at the critical point this will be the most relevant operator[12].

Once the orientations of $\hat{n}_r$ are fixed on each site Λ may be used to define a family of three operators, corresponding to the three orthogonal spin directions on each site. Calling the original orientation Λ_3 (whatever the orientation of $\hat{n}_r$ is on a given site), the other two orientations Λ_1 and Λ_2, can be found by a suitable global rotation of all of the unit vectors $\hat{n}_r$. The diagonal entries of the 3×3 QFI matrix associated with the generators in Eq. 6 are given up to the constant A by,

$$Q_{\mu\mu} = \frac{A}{S^2}(\langle \Lambda_\mu^2 \rangle - \langle \Lambda_\mu \rangle^2), \qquad (7)$$

Once we have chosen our set n_r and hence our three generators we can consider the quantum metric at the state $|\psi\rangle$ associated with the three dimensional parameterization generated by the vector of operators $\vec{\Lambda}$. The corresponding QFI matrix, Q (see Eq. 2) can be used to define an intensive, *mean QFI density* [10]

$$\bar{f} = \frac{1}{3N} \operatorname{Tr}(Q), \qquad (8)$$

where Q is the QFI matrix and N is the number sites. The threshold for genuine multipartite entanglement is then given (in the thermodynamic limit) by $\bar{f} > 3mA$ where A is the metric constant. The bound in [10] can be recovered for the choice of $A = 4$ which corresponds to the QFI most used in a physics context. The trace on the right hand side of Eq. 8 can be arrived at by considering the operator defined in Eq. 6 and then integrating over all

possible orientations of the unit vectors (for fixed relative orientations).

We now discuss the meaning of the metric constant, A. It emerges from the fact that when Eq. 1 is generalized to the quantum case, one wants to make the identification $p(x|\vec{\lambda}) \to \hat{\rho}(\vec{\lambda})$, where $\hat{\rho}$ is a density matrix, and replace the integral over x by a trace operator. This introduces an ambiguity due to the non commutativity of $\hat{\rho}$ with $\partial_{\lambda_\mu}\hat{\rho}$. Where the classical Fisher information is the unique, Riemannian, monotone metric on the space of classical states, the QFI is unique only up to the definition of an operator monotone function [50]. There is, therefore, a whole family of QFI's (see [13] for a list of some common generalizations and their associated operator monotone functions). In the physics literature, what tends to be called the QFI corresponds to a special choice of operator monotone function which treats this ambiguity in the most symmetric possible way. This is done by the implicit definition of the *symmetric logarithmic derivative* (SLD), $\mathcal{L}_\mu$, via [51],

$$\partial_\mu \hat{\rho} = \frac{1}{2}\{\hat{\rho}, \mathcal{L}_\mu\}, \qquad (9)$$

where $\{\cdot, \cdot\}$ is the anti-commutator. The generalization of Eq. 1 is then given by,

$$Q_{\mu\nu} = \operatorname{Tr}\{\hat{\rho}\mathcal{L}_\mu\mathcal{L}_\nu\}, \qquad (10)$$

which, in the zero temperature, limit recovers Eq. 2 with the metric constant $A = 4$. In this work we are concerned only with pure states, and in the pure state limit the difference between various choices of operator monotone functions amounts to a multiplicative factor that we interpret as a normalization. However, no choice of operator monotone function gives a metric constant greater than 4, and in this sense the SLD choice is the maximal QFI [52]. In this work we plot $\frac{1}{A}\bar{f}$, and thus avoid the need to worry about the particular value of the metric constant.

B. Spin-1 Heisenberg Chain

We focus on the spin-1 antiferromagnetic Heisenberg chain with uniaxial anisotropy, D and applied magnetic field along the z axis, B_z,

$$H_0 = \sum_r \vec{S}_r \cdot \vec{S}_{r+1} + D(S_r^z)^2 + B_z S_r^z, \qquad (11)$$

hereafter referred to as the Heisenberg chain. It is a well studied model in low dimensional magnetism which has been extensively studied [53–64]. The completely isotropic point ($D = B_z = 0$) is an example of a phase with symmetry protected topological (SPT) order [65] and exhibits a characteristic doubling of the spectrum of the entanglement Hamiltonian [63]. We call this phase the isotropic phase or the Haldane phase interchangeably. The ground state in this phase is a singlet with a
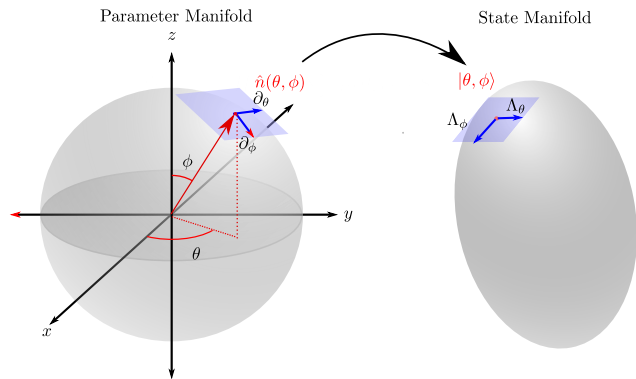
FIG. 1. A schematic of the manifold generated by the applied field parameterized by $\{\theta, \phi\}$, with the corresponding ground state given by $|\theta, \phi\rangle$. The tangent vector ∂_μ becomes the generator Λ_μ.

bulk gap to a degenerate triplet mode [56] for periodic boundary conditions. In the presence of an applied magnetic field, the degeneracy of this mode is lifted, with one (or two depending on the field orientation) of the triplet modes diminishing in energy until a lower critical field, B_z^{lower} where hybridization with the ground state singlet induces a phase with long range AFM order that can be interpreted as a BEC phase [57, 66, 67]. We use the term BEC or magnon BEC to refer to this phase from this point on. Once the upper critical field B_z^{upper} is attained, the per-site magnetization saturates and the spins form a classical paramagnet. For large and positive D, there is a Gaussian transition to a so called "Large-D Phase", which we refer to as the insulator phase, and for negative D a transition to a quasi-ordered Néel phase [61, 62].

II. METHODS

A. Quantum volume and curvature

1. Defining a manifold

In order to investigate the state space geometry in the vicinity of many body wavefunctions we consider the two-dimensional sub manifold of the state space that generalizes the result in [49] to a many-body context. In that work, the manifold we introduce here generated by the operator Λ_{n_r} defined in Eq. 6 was examined for just a single site.

When considering the QFI density of a state, one imagines infinitesimal transformations of the state generated by a hermitian operator. We extend this concept by perturbing a *source Hamiltonian*, $H_0(x)$ with the generator defined in Eq. 6,

$$\mathcal{H}(x; h, \theta, \phi) = H_0(x) + h\Lambda_h(\theta, \phi) \quad (12)$$

and considering the manifold in state space defined by the ground state of the above Hamiltonian for different

strengths and orientations of the perturbing field (see Fig. 1). In state space this manifold can be considered in terms of slices at fixed values of h,

$$\Omega_h = \{|h, \theta, \phi\rangle \,|(\theta, \phi) \in [0, 2\pi] \times [0, \pi]\}, \quad (13)$$

with the state manifold (actually a submanifold) given by $\mathcal{P} = \bigcup_{h>0} \Omega_h$.

The spin-1 Heisenberg chain commutes with the uniform magnetization operator, and so the QFI for the generator with $\hat{n}_r$ uniform is zero. In terms of the QFI, the fully anti-ferromagnetic generator detects the greatest amount of entanglement [60]. This is easy to see from the equivalence between the QFI and the equal time structure factor, which, for the AFM Heisenberg chain, exhibits a peak at $k = \pi$ [58, 59]. From this point on we assume that the generator is the staggered field operator,

$$\Lambda_h(\theta, \phi) = \sum_r (-1)^r \hat{n} \cdot \vec{S}_r, \quad (14)$$

where $\hat{n} = (\cos(\theta)\sin(\phi), \sin(\theta)\sin(\phi), \cos(\phi))$. The superscript π is omitted in the following discussion. For a given orientation of the vector $\hat{n}$, the generators of the three orthogonal transformations are given by

$$\Lambda_\mu = \partial_\mu \mathcal{H} \quad (15)$$

which we hereafter refer to as *tangent operators*. In order to examine the curvature of the manifold $\mathcal{P}$, we are interested in the scaling of the volume of the two dimensional submanifolds, Ω_h, and thus we are particularly interested in Λ_θ and Λ_ϕ. This manifold is schematically depicted in Fig. 1. Λ_h is the tangent operator orthogonal to the sphere. Since we're keeping h fixed and looking at the volume of the two dimensional sphere parameterized by (θ, ϕ) we don't consider the three dimensional metric that would include Λ_h.

Choosing a manifold in state space parameterized by the orientation and strength of a magnetic field makes this study distinct from many other investigations of the many-body quantum state space geometry, which tend to employ state space manifolds parameterized by the driving parameters of the phase transitions (see, for example [26, 27, 32, 38–41], or by examining the geometry of the momentum bands in Fermion models (see [37] for a very general treatment of N level systems).

For each manifold in Eq. 13, the real symmetric part of the QFI matrix corresponding to the generators for transformations in θ and ϕ gives the metric at each point on Ω_h,

$$g(x; h, \theta, \phi) = \frac{1}{2}(Q + Q^*), \quad (16)$$

From the metric, the *quantum volume* of the state space manifold Ω_h can be calculated,

$$V(\lambda; h) = \int_{\mathcal{S}} \sqrt{\det g} \, d\theta d\phi \quad (17)$$

where $\mathcal{S} = [0, 2\pi) \times [0, \pi)$. Here we use the word volume to refer to the size of the 2D state space manifold [68].

In the limit $h \to 0$ the QFI matrix used to define the mean QFI density in Eq. 8 can be recovered by considering perturbations in the x, y, and z directions as defined by the generators Λ_μ with $\mu \in \{x, y, z\}$ discussed in Sec. I A. The mean QFI density is then computed by evaluating the three connected covariances in Eq. 7 in the ground state of the source Hamiltonian.

By contrast, when we wish to compute the quantum volume of the 2D submanifold depicted schematically in Fig. 1, we evaluate the covariances of the tangent operators Λ_θ and Λ_ϕ for states that are held at some small, non-zero field h with orientation (θ, ϕ).

2. Volumes in Flat Space

As an example, consider the quantum metric for a space of $S = 1/2$ particles for which there is no energy landscape (i.e. $H_0 = 0$ in Eq. 12). We call a space where $H_0 = 0$ an *empty* space, as there is nothing to distinguish between different spin states except the orientation of the generator. In this case the generator cannot be treated as a perturbation because there is nothing to perturb and the ground state manifold is isomorphic to a sphere. Explicitly for the case of $S = \frac{1}{2}$ the QFI matrix is,

$$Q = ANh^2 \begin{pmatrix} 1 & -i\sin(\phi) \\ i\sin(\phi) & \sin^2(\phi) \end{pmatrix}, \qquad (18)$$

where the real symmetric part is the metric for a sphere and integrating the imaginary asymmetric part simulates a Dirac monopole as the origin as discussed in [47]. The resulting quantum volume is,

$$V_{S=\frac{1}{2}} = 4\pi ANh^2. \qquad (19)$$

(a detailed derivation is given in App. B) this expression can be generalized to the case of spin-S

$$V_{\mathrm{P}} = 4\pi \left(\frac{AN}{2S}\right) h^2. \qquad (20)$$

(see App. C). The volume of the quantum paramagnetic has no dependence on the relative orientations of $\hat{n}_r$. Moreover, the volume scales exactly as h^2 and thus the local geometry of the empty space is *flat*, with zero curvature. In the classical case, the covariance of the generators of tangential transformations will be zero, since there are no quantum fluctuations. This can be seen explicitly from Eq. 20 which goes to zero in the classical limit, $S \to \infty$. A non-zero quantum volume can be taken to indicate the presence of quantum fluctuations, since this non-zero quantum volume is coming from the fluctuations in the spin expectation value in the direction transverse to the orientation of the generator. Hence the quantum volume represents the same information as the Heisenberg uncertainty relations for the spin components and is an intrinsic consequence of the relationships

between the angular momentum components. We will return to this point in discussing the results for the $S = 1$ Heisenberg chain.

3. Quantum Curvature

The notion of state space curvature can be developed by considering the ratio of the quantum volume of the manifold Ω_h centered on a ground state ψ relative to the quantum volume in an empty space. The *quantum volume ratio*,

$$v_h(\psi(\lambda; h)) := \frac{V(\psi(\lambda; h))}{V_{\mathrm{P}}}$$
$$= v_0 - bRh^2 + \mathcal{O}(h^3) \qquad (21)$$

may be expanded about small values of h, where in the quadratic term determines the curvature of the manifold $\mathcal{P}$. This is essentially the definition of curvature familiar from classical differential geometry, with the scalar curvature R controlling the degree to which the scaling of volumes is enhanced or suppressed in spaces with negative or positive curvatures respectively. We call R the *quantum curvature*. It is independent of the metric normalization A, and should therefore hold for any choice of QFI. The constant b is a positive number that depends only on the dimension of the manifolds used to compute the volumes. For the case of a two dimensional sphere $b = \frac{1}{12}$. The negative sign can be understood by imagining drawing a circle on a saddle or on a sphere. On the saddle (a surface with negative curvature), the circumference of the circle will be greater than in the Euclidean case, and so the scaling of the circumference with the radius of the circle will be greater than in the case of flat space, with the opposite argument going through the sphere (a surface with positive curvature) [69].

When we speak of the quantum volume ratio of a state ψ, we mean the quantum volume of the spheroidal shell centered at ψ in the state space.

B. Numerical Methods

All data was collected using an iDMRG algorithm implemented using the ITensor library [70]. Simulations were performed with bond dimensions of up to 2800 in the vicinity of the critical points, and optimization was run until truncation errors not exceeding 10^{-9} were achieved. In the BEC phase we found that convergence was challenging, likely owing to the long range nature of the correlations that phase [66].

Within the iDMRG, correlation functions were measured to a distance of 1000 sites starting from the center of an effectively infinite chain. These correlations were then used to compute the per-site connected covariances required for the evaluation of the quantum volume.

The sum over N sites is easiest to compute in the iDMRG because we can take advantage of the translation

invariance. The covariances involve a double summation over the correlation matrix C_{r_1,r_2}, $\sum_{r_1=1}^{N} \sum_{r_2=1}^{N} C_{r_1,r_2}$. In systems with translation invariance we can assume that $C_{r_1,r_2} = C_{|r_1-r_2|}$ and reduce the double sum to $N \sum_{r=1}^{N} C_r$. If we had instead considered a finite system with a boundary, the entire double sum would've been

needed. While this is still tractable for non-trivial system sizes when considering the mean QFI density, evaluating the quantum volumes becomes challenging in all but the most symmetrical cases.

In order to compute the integral in Eq. 17, we can take advantage of the symmetries of the source Hamiltonian. We derive (see App. A) the following formulae for the case of full rotational symmetry and axial symmetry,

$$V^{\mathrm{Spherical}}(\lambda; h) = 4\pi Ah^2 \sqrt{\Xi_{xxyy}} \tag{22a}$$

$$V^{\mathrm{Axial}}(\lambda; h) = 2\pi Ah^2 \int_0^\pi \sqrt{\Xi_{xxyy} \cos^2(\phi) \sin^2(\phi) - 2\Xi_{yyzx} \cos(\phi) \sin^3(\phi) + \Xi_{yyzz} \sin^4(\phi)} \; \mathrm{d}\phi \tag{22b}$$
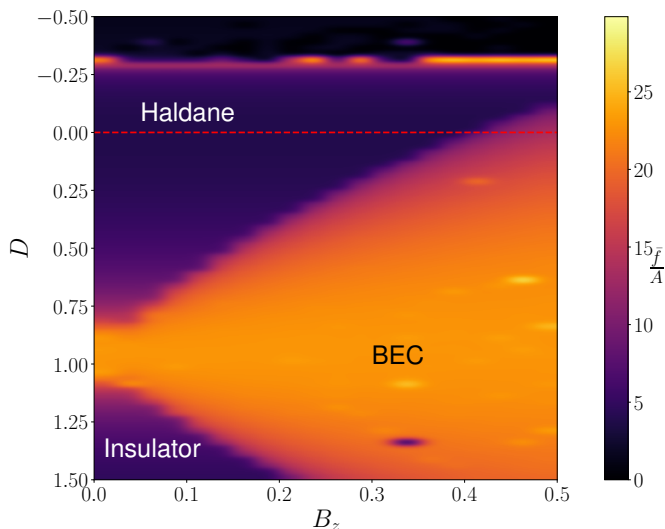

FIG. 2. Phase Diagram of the mean QFI generated by the staggered magnetization operator. The Néel and Insulator phases are un-entangled away from the critical point. The Magnon BEC phase appears as the critical fan of the Gaussian critical point separating the Haldane phase from the Insulator phase. Regions of low entanglement in the BEC phase are numerical artifacts from failed convergence of the iDMRG. When points do converge it is with a truncation error of no more than 10^{-9}. The red horizontal line indicates the slice that is shown and extended in Fig. 3

where in general,

$$\Xi_{abcd}(\lambda; h, \theta, \phi) = \mathcal{A}_{ab}\mathcal{A}_{cd} - \mathcal{A}_{ac}\mathcal{A}_{bd}. \tag{23}$$

Here $\mathcal{A}_{ab}$ is the real part of the correlation matrix,

$$\mathcal{C}^{ab} = \sum_{r_1,r_2} (-1)^{r_1+r_2} \mathrm{Cov}_{\psi(\theta,\phi)}(S_{r_1}^a, S_{r_2}^b), \tag{24}$$

given by $\mathcal{A} = \frac{1}{2}(\mathcal{C}+\mathcal{C}^*)$ and the indices $a, b, c, d \in \{x, y, z\}$ are taken in the lab frame. The correlation matrix will depend on the strength of the perturbing field h, and also

on the particular values of the Hamiltonian parameters which we here denote as λ. In Eqs. 22, the angular dependence in (θ, ϕ) has been integrated out completely in the spherical case, while in the axial case Ξ will have some dependence on ϕ. In the axial case the integral over ϕ can be performed numerically with relatively few integration points. For the data shown in Figs. 5 6 the ϕ component was integrated with 50 equally spaced points. This is relevant for experiments where measurements would be required at a range of field orientations in order to compute the quantum volume.

III. RESULTS AND DISCUSSION

A. Mean QFI Density

Taking Eq. 11 as our source Hamiltonian, the mean QFI density divided by the metric constant was computed for a patch of the (D, B_z) parameter space with $D \in [-0.5, 1.5]$ and $B_z \in [0, 0.5]$. In this section we imagine a 3×3 QFI matrix where the parameterizations are generated by the fields in the x, y, and z directions in the lab frame as discussed in Sec. I A. The correlation functions are evaluated for the ground state of the source Hamiltonian, taking $h = 0$ in Eq. 12. The results are given in Fig. 2. We see robust multipartite entanglement through the Haldane phase indicating at minimum bipartite entanglement. We find our results to be consistent with the low temperature single mode approximation employed by the authors in [60].

Taking a slice of the phase diagram along $D = 0$ (see Fig. 3), we see that the multipartite entanglement of the magnon BEC is substantially higher, and estimate the value of the lower critical field to be $B_z^{\mathrm{lower}} \approx 0.41$, which is consistent with previous studies [57] which place the value of B_z^{lower} at the Haldane gap [64]. From Fig. 3 the multipartite entanglement can be seen to peak before falling to the upper critical field of approximately $B_z^{\mathrm{upper}} \approx 4$, beyond which the system enters a classical

paramagnetic phase for which the mean QFI density is nearly zero and the per site magnetization becomes saturated.

In Fig 2 we see that the BEC phase appears as a fan of genuine multipartite entanglement emanating from the Gaussian transition to the insulator phase. The BEC phase can be reached from either the insulator phase or the Haldane phase. Experimental studies [66] on the material $NiCl_2$-$4SC(NH_2)_2$, for which the ground state is in the insulator phase and which exhibits an additional easy axis anisotropy, reveal that the long range correlations in the BEC phase persist up to a finite temperature that grows as a function of the applied field to a maximal point which occurs at approximately the point where the average onsite magnetization assumes a value of $\langle M_z \rangle/N \approx 0.4$. Owing to the analogous peak in the GME as witnessed by the QFI at the point where the onsite magnetization assumes the values of $\langle M_z \rangle/N \approx 0.4$, we speculate that this temperature scale may be related to the massive multipartite entanglement in the ground state. In particular, the temperature curve for the BEC phase in [66] is of a form that is very similar to the curve of genuine multipartite entanglement in Fig. 3.

Within the Haldane phase the multipartite entanglement is completely constant as a function of B_z, as can been seen in Fig. 3 in the phase labelled H. This indicates that the Haldane phase entanglement is robust to the presence of magnetic fields. Coupled with the already established robustness of the Haldane phase entanglement to finite temperatures [17, 60], our observations establish Haldane gap anti-ferromagnets as reliable sources of at least bi-partite entanglement even in the presence of environmental disturbances that tend to decohere entangled states. This has especially important application in light of the application of SPT phases to measurement based quantum computation [71, 72].

In contrast to a homogeneous applied field, any non-zero uniaxial anisotropy appears to increase the amount of genuine multipartite entanglement as seen by considering a cut in the state space where $B_z = 0$ (see Fig. 4). Along this cut we can see clear divergences in the GME at both the Néel and insulator transitions. The Haldane phase exhibits two partite entanglement in the vicinity of the isotropic point where $D = 0$, while the other phases are trivial from a quantum perspective, exhibiting zero GME.

The behaviour of the mean QFI can be contrasted with the fidelity susceptibility, which, for the Gaussian transition in particular, exhibits a less pronounced signal (see Fig. 3 of [62]). While the fidelity susceptibility associated with the Ising transition does exhibit a divergence, this divergence does not establish the entanglement of the critical point, due to the reasons discussed in Sec. I A.

While the Ising transition was already established as a strongly entangled critical point by the authors in [60], the observation of entanglement at the Gaussian critical point was not made. This is because the component Q_{zz} of the QFI matrix which was studied by the authors
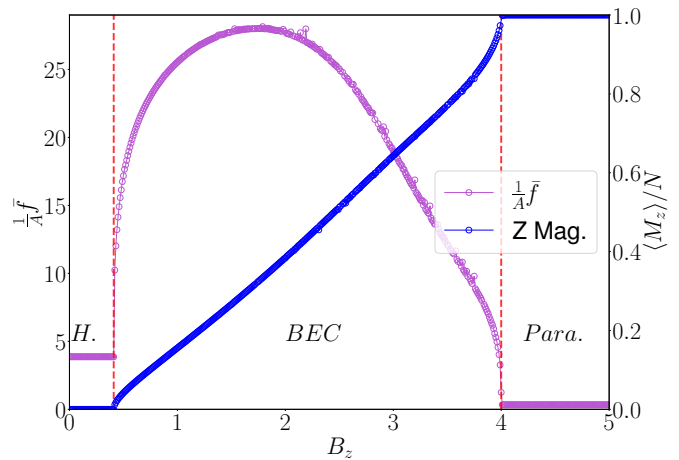

FIG. 3. QFI associated with staggered magnetization operator as a function of magnetic field in the z direction (magenta curve) and average per site magnetization along the z axis (blue curve). Notice that the mean QFI density is constant in the Haldane phase and nearly zero in the paramagnetic phase.
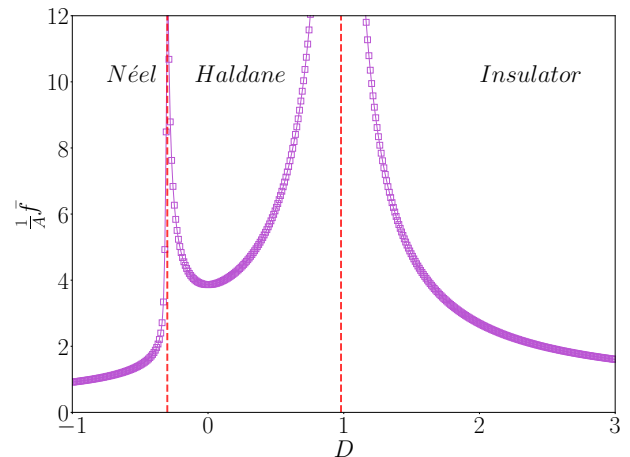

FIG. 4. QFI associated with staggered magnetization operator as a function of the uniaxial anisotropy. The Haldane phase exhibits the largest amount of multipartite entanglement, which is enhanced by non-zero values of the uniaxial anisotropy.

in [60] does not diverge at the Gaussian transition, and it is rather the components of the QFI matrix in the directions transverse to the critical point.

B. Quantum Curvature

In this section we consider the 2D submanifold centered at the ground state of the source Hamiltonian for small, non-zero values of h in Eq. 12. The correlation functions then in general depend on both h and the orientation of the field (θ, ϕ). Due to the symmetries of the spin-1 chain defined in Eq. 11, we can integrate
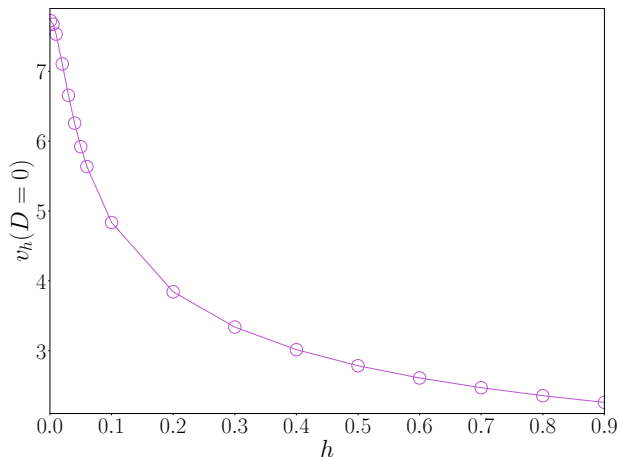
FIG. 5. Quantum volume ratio for spheres centered at the isotropic point.

FIG. 6. Quantum volume ratio for spheres of perturbatively small radius as a function of the uniaxial anisotropy D. Sphere sizes (applied fields) range in size from $h = 0.0001$ to $h = 0.04$. The red shaded region indicates where the curvature is positive while the grey region indicates where the curvature is negative, approximately corresponding to the onset of the scaling regime.

out the dependence on (θ, ϕ) at the isotropic point, and the dependence on θ for the case of non-zero uniaxial anisotropy, using the formulae defined in Eqs. 22. The correlations are then evaluated as functions of h in the case of spherical symmetry, or as functions of h and ϕ in the case of axial symmetry. In both cases the correlations will depend on the value of D. The volumes of the 2-spheres for different values of h are sufficient for us to then compute the quantum curvature defined in Eq. 21. If all correlations $\langle S_{r_1}^a S_{r_2}^b \rangle$ for a given field strength h and orientation (θ, ϕ) are evaluated with $a, b \in \{x, y, z\}$ in the lab frame then Eq. 22 can be evaluated.

We begin at the isotropic point with $D = B_z = 0$ and examine the volume ratios of the ground state of Eq. 12 as function of h that are taken to be small relative to the exchange coupling. The results of this calculation are shown in Fig 5. We see that the volume ratio decreases monotonically, indicating that the manifold $\mathcal{P}$ is asymptotically flat in the limit of large h. Near $h = 0$ it is clear that this function is concave down, which, from Eq. 21 implies that the curvature is positive. The volume ratio being larger than 1 indicates the presence of a high degree of quantum fluctuation relative to those implied purely by the uncertainty relation for the spin operators, as discussed in Sec. II.

By sweeping across values of D from -1 to 3 we can determine how the curvature of the state space depends on the uniaxial anisotropy. The results of this analysis are shown in Fig. 6. Taking the second derivative of the volume ratio as a function of h at $h = 0$ gives us the sign of curvature, indicated by the red (positive curvature) and grey (negative curvature) shaded regions in Fig. 6). We see that the Haldane phase is characterized by strong positive curvature, while the Néel and insulator phases are flat with essentially zero curvature.

Recall from Sec. II that the quantum volume quantifies the fluctuations in the spin degrees of freedom. In flat space (i.e. spaces where $H_0 = 0$), these fluctuations
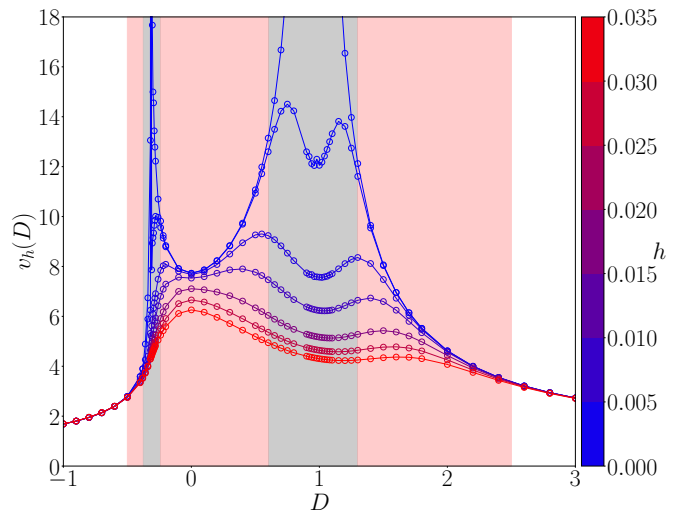
come purely from the Heisenberg uncertainty relations. Hence the quantum volume in a flat space of N spin-S particles tends to zero in the limit $S \to \infty$. In the Néel and Insulator phases, we find a quantum volume ratio $v_h > 1$, indicating that these phases exhibit enhanced fluctuations relative to what would be expected from the pure uncertainty relations. From Fig. 4, we see clearly that neither of these phase are entangled, (see the inequality in Eq. 5). Hence, quantum phases might have enhanced fluctuations without necessarily exhibiting any entanglement.

Despite these enhanced fluctuations, both the Néel and insulator phases are flat, with quantum volume ratios that are constant as a function of the field h. By contrast, the Haldane phase, which exhibits the greatest enhancement in quantum fluctuations of the three, also exhibits a region of large positive curvature, leading into the critical points where we find a sudden, discontinuous jump to a region of negative curvature which we interpret as the onset of the scaling regime. The Haldane phase is the only phase of the three that exhibits any degree of entanglement, and it appears that the quantum curvature tends to grow as the entanglement increases, as seen by the dispersion of the curves at fixed values of h in Fig. 6. The flatness of the insulator phase also establishes that the curvature in the Haldane phase is not simply a consequence of the Haldane gap, as the insulator phase is also gapped but exhibits no quantum curvature.

It seems clear that the quantum curvature is connected to the presence of entanglement, with the trivial phases appearing completely flat. A phase with no entanglement would then be expected to have zero curvature, except

perhaps when the critical point is approached. But it is not clear whether or not the presence of quantum curvature is only incidental in the Haldane phase, and is in fact due to the nearby quantum critical points which exhibit a massive divergence in the amount of GME. This would account for the presence of small amounts of positive curvature in the Néel and insulator phases as the critical points are approached. In this case the positive curvature in the Haldane phase is a consequence of the phases existing in between these two critical points. This introduces the possibility of detecting the presence of quantum critical points even outside of the scaling regime, without the need to directly witness the diverging multipartite entanglement at the critical point. This would be especially useful in inelastic neutron scattering experiments where resolution issues make it effectively impossible to directly measure diverging multipartite entanglement [11]. That state space curvature is induced by the phase boundary implies that quantum critical regions have long range effects in the state space, influencing not just the geometry of states in the scaling regime, but also the states that lie in between these critical points.

It is also possible that state space curvature is generic in the presence of any amount of entanglement, with entanglement and state space curvature sharing a relationship that is somewhat analogous to the relationship between mass and space-time curvature.

Our calculation of the state space curvature can be contrasted with those of [27, 32, 40] and especially [38, 39]. In these studies, it is the curvature corresponding to the ground state manifold parameterized by the driving parameters of the phase transitions themselves that is computed. In particular, [38] finds that the curvature of the manifold parameterized by a uniform field along the z axis and the temperature in the XXZ model reveal different scaling regimes in the vicinity of the quantum critical point.

This is similar to our observation that the state space curvature becomes negative in the immediate vicinity of the quantum critical point, but our construction pertains to a state space manifold that might be applied to transitions where the magnetic field is not a priori the driving parameter of the phase transition. It is also interesting that there is a discontinuous jump from a region of positive state space curvature in the Haldane phase and immediately around the critical points to a region of negative state space curvature in the quantum critical regime, without any intermediate flat region. In the grey regions of Fig. 6, it is important to emphasize that the form of the quantum metric defined in Eq. 2 breaks down, as it does not account for the non-adiabatic level crossings that occur at the critical point. A more careful treatment would involve computing the entire spectrum and applying the form of the quantum metric introduced in [26]. We leave these questions to future study.

IV. CONCLUSION

In this work we have mapped out the phase diagram of the spin-1 antiferromagnetic Heisenberg chain in the space of applied magnetic field and uniaxial anisotropy (both along the z axis). The five phases of the spin-1 Heisenberg chain considered here have all been shown to have substantially different behaviour in terms of the mean QFI density. In particular we find the both the Néel and insulator phases exhibit small but non-zero genuine multipartite entanglement relative to the SPT Haldane phase. The entanglement in the SPT phase seems to be greatly enhanced by the presence of unixial anisotropy, and is undiminished under the application of a uniform magnetic field. The fact the the multipartite entanglement in the Haldane phase is robust against the application of magnetic fields and exhibits a finite temperature plateau up to energies on the scale of the Haldane gap [17, 60] may have implications from quantum metrology and quantum information, where state exhibiting robust entanglement are used as a resource in various measurement and information processing tasks

Once the applied field reaches a strength on the order of the Haldane gap we find a drastic increase in the multipartite entanglement in the magnon BEC phase. This condensate is found to emanate from the Gaussian quantum critical point that is generated by large positive values of the uniaxial anisotropy, and is similar to the quantum critical fans expected in the finite temperature region above the quantum critical point. In the BEC phase we find a peak multipartite entanglement at $B_z^{\max} \approx 1.6$. More work should be done to understand the relationship between the massive amount of multipartite entanglement in the ground state and the finite temperature transition points of the BEC phase mapped out in [66].

By computing the quantum metric corresponding to a state space manifold parameterized by the magnitude and orientation of a small, staggered magnetic field, we introduced the ideas of quantum volume and quantum curvature, and computed both for a range of values of the uniaxial anisotropy.

Crucially, we have demonstrated that the Haldane phase in this model is characterized by a sizeable, positive quantum curvature, while the Néel and insulator phases are flat. We have identified two possibilities. First, that the presence of quantum curvature is induced by the presence of quantum critical points, in which case measurement of such curvature may prove applicable as a probe of quantum criticality outside of the scaling regime in neutron scattering experiments. Second, it is possible that massive positive curvature is an intrinsic feature any GME phase. It is important to emphasize that the entanglement in the SPT phase is short range in nature [65]. It is unclear whether or not the state space geometry computed in terms of a linear, local operator would be sensitive to long range entangled phases, where the mean QFI density of local operators does not detect GME [19, 25].

One final observation is that the mean QFI density along the $B_z = 0$ cut shown in Fig. 4, and the quantum volume ratio in the limit $h \to 0$, v_0 shown as the maximal curve in Fig. 6 appear to be almost exactly proportional to one another. Furthermore, the curvature appears to grow proportionately to the mean QFI density up to the onset of the critical region. This raise the possibility that the GME is a source of curvature in the state space, analogous to the curvature of space time due to the presence of mass-energy. We do not present any rigorous proof of the relationship between v_0 and $\bar{f}$ in this work, leaving the problem to future study.

Appendix A: Symmetric Formulae for the Quantum Volume

In order to efficiently evaluate Eq. 17 is is crucial that we exploit symmetries of the source Hamiltonian. This would also be the case for experimental explorations of the quantum volume ratio. There are two symmetries that are of particular interest to us. The first is the full rotational symmetry given by the Euler angles (θ, ϕ). Recall the rotation operator [73],

$$R(\theta, \phi) = e^{i \sum_r S_r^z \theta} e^{i \sum_r S_r^y \phi} \tag{A1}$$

where the gauge angle representing an initial rotation about the z axis is taken to be zero. If this operator represents a symmetry of the source Hamiltonian, we may generate the state manifold by applying the rotation to $\mathcal{H}$,

$$\mathcal{H}(\lambda; h, \theta, \phi) = R(\theta, \phi)\mathcal{H}(\lambda; h, 0, 0)R^{-1}(\theta, \phi) \tag{A2}$$

Each element of the quantum metric is given by the real symmetric part of the covariance of the generators, as defined in Eq. 16. Using the particular form of the generator in Eq. 15 and denoting the real symmetric part of the covariance matrix $\mathcal{A}$ gives,

$$g_{\mu\nu} = \frac{A}{S^2} h^2 d_\mu^a d_\nu^b \mathcal{A}^{ab} \tag{A3}$$

where $\mathcal{A} = \frac{1}{2}(\mathcal{C} + \mathcal{C}^*)$, and

$$\mathcal{C}^{ab} = \sum_{r_1, r_2} (-1)^{r_1+r_2} \text{Cov}_{\psi(\theta,\phi)}(S_{r_1}^a, S_{r_2}^b) \tag{A4}$$

Under a rotation the covariance matrix transforms

$$\text{Cov}_{\psi(\theta,\phi)}(S_{r_1}^a, S_{r_2}^b) \to R^{aa'} R^{bb'} \text{Cov}_{\psi(0,0)}(S_{r_1}^{a'}, S_{r_2}^{b'})$$
where Einstein summation is used and,

$$R = \begin{pmatrix} \cos(\theta)\cos(\phi) & -\sin(\theta) & \cos(\theta)\sin(\phi) \\ \sin(\theta)\cos(\phi) & \cos(\theta) & \sin(\theta)\sin(\phi) \\ \sin(\phi) & 0 & \cos(\phi) \end{pmatrix} \tag{A5}$$

Using this transformation we can extract the angular dependence of the metric for the case of spherical and axial symmetry, and integrate out that dependence completely, leaving

$$V^{\text{Spherical}}(\lambda; h) = 4\pi \frac{A}{S^2} h^2 \sqrt{\Xi_{xxyy}} \tag{A6}$$

where,

$$\Xi_{abcd} = \mathcal{A}_{ab}\mathcal{A}_{cd} - \mathcal{A}_{ac}\mathcal{A}_{bd}. \tag{A7}$$

For the axial case we, without loss of generality, choose the case where the system is symmetric about rotations about the z axis (set $\phi = 0$ in Eq. A5). In this case we have,

$$V^{\text{Axial}}(\lambda; h) = 2\pi \frac{A}{S^2} h^2 \int_0^\pi \sqrt{\Xi_{xxyy}\cos^2(\phi)\sin^2(\phi) - 2\Xi_{yyzx}\cos(\phi)\sin^3(\phi) + \Xi_{yyzz}\sin^4(\phi)}\, \mathrm{d}\phi \tag{A8}$$

In the axial case we still have to perform a numerical integration with respect to ϕ but good convergence can be achieved using relatively few slices.

Appendix B: QFI matrix of a flat space for $S = 1/2$

The quantum metric of a flat space can be calculated for N spin-1/2 particles by considering the Hamiltonian

in Eq. 12 setting $H_0 = 0$. The tangent operators are given by,

$$\Lambda_\mu = \frac{h}{2} \vec{d}_\mu \cdot \vec{\sigma} \tag{B1}$$

Where d_μ is the derivative of the unit vector along the μ direction.

Substituting these definitions into Eq. 2 (assuming

summation over repeated indices),

$$Q_{\mu\nu} = Ah^2 d_\mu^a d_\nu^b \left(\langle \sigma^a \sigma^b \rangle - \langle \sigma^a \rangle \langle \sigma^b \rangle \right)$$
$$= Ah^2 d_\mu^a d_\nu^b C^{ab} \qquad (B2)$$

Where we've defined the connected correlation C^{ab}. We

can use the algebra of the Pauli matrices to simplify the expression for the correlations somewhat,

$$C^{ab} = \langle \sigma^a \sigma^b \rangle - \langle \sigma^a \rangle \langle \sigma^b \rangle$$
$$= \delta^{ab} + i\epsilon_{abc}\langle \sigma^c \rangle - \langle \sigma^a \rangle \langle \sigma^b \rangle \qquad (B3)$$

Now substituting this Eq. B2 gives,

$$Q_{\mu\nu} = Ah^2 \left(\vec{d}_\mu \cdot \vec{d}_\nu + i(\vec{d}_\mu \times \vec{d}_\nu) \cdot \langle \vec{\sigma} \rangle - d_\mu^a d_\nu^b \langle \sigma^a \rangle \langle \sigma^b \rangle \right) \qquad (B4)$$

Now we must evaluate the expectation values of the Pauli matrices. Recall that these are themselves functions of (θ, ϕ). For the two level case we can compute the ground state explicitly,

$$\left| \lambda_-^{\Delta=0} \right\rangle = \begin{pmatrix} \sin\left(\frac{\phi}{2}\right) \\ -\cos\left(\frac{\phi}{2}\right)e^{i\theta} \end{pmatrix} \qquad (B5a)$$

The expectation value of the Pauli vector in the ground state is then,

$$\langle \vec{\sigma} \rangle = \begin{pmatrix} -\cos(\theta)\sin(\phi) \\ -\sin(\theta)\sin(\phi) \\ -\cos(\phi) \end{pmatrix} = -\hat{n}(\theta, \phi) \qquad (B6)$$

The metric in Eq. B4 is now given by,

$$Q_{\mu\nu} = Ah^2 \left(\vec{d}_\mu \cdot \vec{d}_\nu - i(\vec{d}_\mu \times \vec{d}_\nu) \cdot \hat{n} \right) \qquad (B7)$$

In this form, evaluating the components of the metric proves to be a straightforward exercise

$$Q = Ah^2 \begin{pmatrix} 1 & -i\sin(\phi) \\ i\sin(\phi) & \sin^2(\phi) \end{pmatrix} \qquad (B8)$$

Generalizing this expression to N spins amounts to multiplying by N

$$Q = ANh^2 \begin{pmatrix} 1 & -i\sin(\phi) \\ i\sin(\phi) & \sin^2(\phi) \end{pmatrix} \qquad (B9)$$

since the connected correlations between sites is zero by construction. Notice that this expression does not depend on the relative orientation of the neighbouring sites. For $S = \frac{1}{2}$, the quantum volume (surface area of a 2D sphere in the spin Hilbert space) is then,

$$V_{S=\frac{1}{2}} = 4\pi ANh^2 \qquad (B10)$$

Appendix C: Quantum volume of a flat space for spin-S

In computing to quantum volume ratio, we want to generalize the volume computed in Eq. B10 to the case of spin-S. This is easy to do by employing the formula for the spherically symmetric quantum volume given in Eq. A6

Using Eq. A6 we can compute the quantum volume of a paramagnet. Taking $H_0 = 0$ in Eq. 12 and denoted the ground state of the spin-S paramagnet as $|S, -S\rangle$, we can use the raising and lowering operators,

$$S^+ |S, m\rangle = \sqrt{S(S+1) - m(m+1)} |S, m+1\rangle$$
$$S^- |S, m\rangle = \sqrt{S(S+1) - m(m-1)} |S, m-1\rangle$$

For the paramagnet the connected correlation between is exactly zero, so we can evaluate only the onsite correlations in the directions transverse to the orientation of the field (which we take to be z). The expectation values in x and in y are the same, so we only present the calculation of the former. For the state that is fully polarized down along the z axis, the only contribution to $(S^x)^2$ is given by,

$$\mathcal{A}^{xx} = \frac{1}{4} \langle S, -S| S^- S^+ |S, -S\rangle = \frac{S}{2} \qquad (C2)$$

Substituting this into Eq. A6 gives,

$$V_P = 4\pi \left(\frac{AN}{2S} \right) h^2 \qquad (C3)$$

where we have group the spin, S, metric constant A, and number of sites N along with the factor of $\frac{1}{2}$ in order to emphasize the familiar form of the volume of a sphere. The factor N is coming from the fact that $\mathcal{A}^{ab}$ in Ξ^{abcd} contains a sum over N sites, which for the the case of $H_0 = 0$ scales linearly in N (since the connected correlations between sites are zero). We can check and see that for $S = \frac{1}{2}$ we recover Eq. B10.

[1] M. Yu, P. Yang, M. Gong, Q. Cao, Q. Lu, H. Liu, S. Zhang, M. B. Plenio, F. Jelezko, T. Ozawa, *et al.*, Experimental measurement of the quantum geometric tensor using coupled qubits in diamond, National science review **7**, 254 (2020).

[2] R. A. Fisher, On the mathematical foundations of theoretical statistics, Philosophical transactions of the Royal Society of London. Series A, containing papers of a mathematical or physical character **222**, 309 (1922).

[3] O. Johnson, *Information theory and the central limit theorem* (World Scientific, 2004).

[4] W. K. Wootters, Statistical distance and hilbert space, Physical Review D **23**, 357 (1981).

[5] S. L. Braunstein and C. M. Caves, Statistical distance and the geometry of quantum states, Physical Review Letters **72**, 3439 (1994).

[6] I. Bengtsson and K. Życzkowski, *Geometry of quantum states: an introduction to quantum entanglement* (Cambridge university press, 2017).

[7] J. Provost and G. Vallee, Riemannian structure on manifolds of quantum states, Communications in Mathematical Physics **76**, 289 (1980).

[8] A. Lesniewski and M. B. Ruskai, Monotone riemannian metrics and relative entropy on noncommutative probability spaces, Journal of Mathematical Physics **40**, 5702 (1999).

[9] M. V. Berry, Quantal phase factors accompanying adiabatic changes, Proceedings of the Royal Society of London. A. Mathematical and Physical Sciences **392**, 45 (1984).

[10] P. Hyllus, W. Laskowski, R. Krischek, C. Schwemmer, W. Wieczorek, H. Weinfurter, L. Pezzé, and A. Smerzi, Fisher information and multiparticle entanglement, Physical Review A **85**, 022321 (2012).

[11] A. Scheie, P. Laurell, A. Samarakoon, B. Lake, S. Nagler, G. Granroth, S. Okamoto, G. Alvarez, and D. Tennant, Witnessing entanglement in quantum magnets using neutron scattering, Physical Review B **103**, 224434 (2021).

[12] P. Hauke, M. Heyl, L. Tagliacozzo, and P. Zoller, Measuring multipartite entanglement through dynamic susceptibilities, Nature Physics **12**, 778 (2016).

[13] T. Shitara and M. Ueda, Determining the continuous family of quantum fisher information from linear-response theory, Physical Review A **94**, 062316 (2016).

[14] P. Laurell, A. Scheie, C. J. Mukherjee, M. M. Koza, M. Enderle, Z. Tylczynski, S. Okamoto, R. Coldea, D. A. Tennant, and G. Alvarez, Quantifying and controlling entanglement in the quantum magnet cs 2 cocl 4, Physical Review Letters **127**, 037201 (2021).

[15] S. L. Braunstein, C. M. Caves, and G. J. Milburn, Generalized uncertainty relations: theory, examples, and lorentz invariance, annals of physics **247**, 135 (1996).

[16] A. S. Holevo, *Probabilistic and statistical aspects of quantum theory*, Vol. 1 (Springer Science & Business Media, 2011).

[17] M. Gabbrielli, A. Smerzi, and L. Pezzè, Multipartite entanglement at finite temperature, Scientific reports **8**, 1 (2018).

[18] S. Yin, J. Song, Y. Zhang, and S. Liu, Quantum fisher information in quantum critical systems with topological characterization, Physical Review B **100**, 184417 (2019).

[19] J. Lambert and E. S. Sørensen, Revealing divergent length scales using quantum fisher information in the kitaev honeycomb model, Physical Review B **102**, 224401 (2020).

[20] S. Yang, S.-J. Gu, C.-P. Sun, and H.-Q. Lin, Fidelity susceptibility and long-range correlation in the kitaev honeycomb model, Physical Review A **78**, 012304 (2008).

[21] Q. Zheng, Y. Yao, and X.-W. Xu, Probing berezinskii–kosterlitz–thouless phase transition of spin-half xxz chain by quantum fisher information, Communications in Theoretical Physics **63**, 279 (2015).

[22] S.-S. Li, H.-G. Yi, and R.-H. Chen, Spin squeezing and quantum fisher information in the lipkin-meshkov-glick model, International Journal of Theoretical Physics **52**, 1175 (2013).

[23] Y.-Q. Ma, S.-J. Gu, S. Chen, H. Fan, and W.-M. Liu, The euler number of bloch states manifold and the quantum phases in gapped fermionic systems, EPL (Europhysics Letters) **103**, 10008 (2013).

[24] W.-F. Liu, J. Ma, and X. Wang, Quantum fisher information and spin squeezing in the ground state of the xy model, Journal of Physics A: Mathematical and Theoretical **46**, 045302 (2013).

[25] L. Pezze, M. Gabbrielli, L. Lepori, and A. Smerzi, Multipartite entanglement in topological quantum phases, Physical review letters **119**, 250401 (2017).

[26] P. Zanardi and N. Paunković, Ground state overlap and quantum phase transitions, Physical Review E **74**, 031123 (2006).

[27] P. Zanardi, P. Giorda, and M. Cozzini, Information-theoretic differential geometry of quantum phase transitions, Physical review letters **99**, 100603 (2007).

[28] A. F. Albuquerque, F. Alet, C. Sire, and S. Capponi, Quantum critical scaling of fidelity susceptibility, Phys. Rev. B **81**, 064418 (2010).

[29] M. Thesberg and E. S. Sørensen, General quantum fidelity susceptibilities for the J_1-J_2 chain, Phys. Rev. B **84**, 224435 (2011).

[30] J. Liu, H.-N. Xiong, F. Song, and X. Wang, Fidelity susceptibility and quantum fisher information for density operators with arbitrary ranks, Physica A: Statistical Mechanics and its Applications **410**, 167 (2014).

[31] M. Kolodrubetz, D. Sels, P. Mehta, and A. Polkovnikov, Geometry and non-adiabatic response in quantum and classical systems, Physics Reports **697**, 1 (2017).

[32] L. C. Venuti and P. Zanardi, Quantum critical scaling of the geometric tensors, Physical review letters **99**, 095701 (2007).

[33] R. B. Laughlin, Quantized hall conductivity in two dimensions, Physical Review B **23**, 5632 (1981).

[34] T. Ozawa and B. Mera, Relations between topology and the quantum metric for chern insulators, arXiv preprint arXiv:2103.11582 (2021).

[35] A. Zhang, Revealing chern number from quantum metric, Chinese Physics B **31**, 040201 (2022).

[36] B. Mera and T. Ozawa, Kähler geometry and chern insulators: Relations between topology and the quantum metric, Physical Review B **104**, 045104 (2021).

[37] C. J. Kemp, N. R. Cooper, and F. N. Ünal, Nested spheres description of the n-level chern number and the generalized bloch hypersphere, arXiv preprint

arXiv:2110.06934 (2021).

[38] P. Zanardi, L. C. Venuti, and P. Giorda, Bures metric over thermal state manifolds and quantum criticality, Physical Review A **76**, 062318 (2007).

[39] H. Janyszek and R. Mrugal, Riemannian geometry and the thermodynamics of model magnetic systems, Physical Review A **39**, 6515 (1989).

[40] M. Kolodrubetz, V. Gritsev, and A. Polkovnikov, Classifying and measuring geometry of a quantum ground state manifold, Physical Review B **88**, 064304 (2013).

[41] D. Gutiérrez-Ruiz, D. Gonzalez, J. Chávez-Carlos, J. G. Hirsch, and J. D. Vergara, Quantum geometric tensor and quantum phase transitions in the lipkin-meshkov-glick model, Physical Review B **103**, 174104 (2021).

[42] R. L. Klees, G. Rastelli, J. C. Cuevas, and W. Belzig, Microwave spectroscopy reveals the quantum geometric tensor of topological josephson matter, Physical Review Letters **124**, 197002 (2020).

[43] D. Gutiérrez-Ruiz, J. Chávez-Carlos, D. Gonzalez, J. G. Hirsch, and J. D. Vergara, Quantum metric tensor of the dicke model: Analytical and numerical study, Physical Review B **105**, 214106 (2022).

[44] O. Bleu, D. Solnyshkov, and G. Malpuech, Measuring the quantum geometric tensor in two-dimensional photonic and exciton-polariton systems, Physical Review B **97**, 195422 (2018).

[45] R. L. Klees, J. C. Cuevas, W. Belzig, and G. Rastelli, Ground-state quantum geometry in superconductor–quantum dot chains, Physical Review B **103**, 014516 (2021).

[46] A. Gianfrate, O. Bleu, L. Dominici, V. Ardizzone, M. De Giorgi, D. Ballarini, K. West, L. Pfeiffer, D. Solnyshkov, D. Sanvitto, *et al.*, Direct measurement of the quantum geometric tensor in a two-dimensional continuous medium, arXiv preprint arXiv:1901.03219 (2019).

[47] X. Tan, D.-W. Zhang, Z. Yang, J. Chu, Y.-Q. Zhu, D. Li, X. Yang, S. Song, Z. Han, Z. Li, *et al.*, Experimental measurement of the quantum metric tensor and related topological phase transition with a superconducting qubit, Physical review letters **122**, 210401 (2019).

[48] A. Gianfrate, O. Bleu, L. Dominici, V. Ardizzone, M. De Giorgi, D. Ballarini, G. Lerario, K. West, L. Pfeiffer, D. Solnyshkov, *et al.*, Measurement of the quantum geometric tensor and of the anomalous hall drift, Nature **578**, 381 (2020).

[49] G. Palumbo and N. Goldman, Revealing tensor monopoles through quantum-metric measurements, Physical review letters **121**, 170401 (2018).

[50] E. A. Morozova and N. N. Chentsov, Markov invariant geometry on state manifolds, Itogi Nauki i Tekhniki. Seriya" Sovremennye Problemy Matematiki. Noveishie Dostizheniya" **36**, 69 (1989).

[51] A. S. Holevo, *Statistical structure of quantum theory*, Vol. 67 (Springer Science & Business Media, 2003).

[52] G. Tóth and D. Petz, Extremal properties of the variance and the quantum fisher information, Physical Review A **87**, 032324 (2013).

[53] R. Botet and R. Jullien, Ground-state properties of a spin-1 antiferromagnetic chain, Physical Review B **27**, 613 (1983).

[54] R. Botet, R. Jullien, and M. Kolb, Finite-size-scaling study of the spin-1 heisenberg-ising chain with uniaxial anisotropy, Physical Review B **28**, 3914 (1983).

[55] D. Peters, I. McCulloch, and W. Selke, Spin-one heisenberg antiferromagnetic chain with exchange and single-ion anisotropies, Physical Review B **79**, 132406 (2009).

[56] F. D. M. Haldane, Continuum dynamics of the 1-d heisenberg antiferromagnet: Identification with the o (3) nonlinear sigma model, Physics letters a **93**, 464 (1983).

[57] E. S. Sørensen and I. Affleck, Large-scale numerical evidence for bose condensation in the s= 1 antiferromagnetic chain in a strong field, Physical review letters **71**, 1633 (1993).

[58] S. R. White and I. Affleck, Spectral function for the s= 1 heisenberg antiferromagetic chain, Physical Review B **77**, 134437 (2008).

[59] E. S. Sorensen, I. Affleck, *et al.*, Equal-time correlations in haldane-gap antiferromagnets, Physical Review B **49**, 15771 (1994).

[60] J. Lambert and E. Sørensen, Estimates of the quantum fisher information in the s= 1 antiferromagnetic heisenberg spin chain with uniaxial anisotropy, Physical Review B **99**, 045117 (2019).

[61] W. Chen, K. Hida, and B. Sanctuary, Ground-state phase diagram of s= 1 xxz chains with uniaxial single-ion-type anisotropy, Physical Review B **67**, 104401 (2003).

[62] A. Langari, F. Pollmann, and M. Siahatgar, Ground-state fidelity of the spin-1 heisenberg chain with single ion anisotropy: quantum renormalization group and exact diagonalization approaches, Journal of Physics: Condensed Matter **25**, 406002 (2013).

[63] F. Pollmann, A. M. Turner, E. Berg, and M. Oshikawa, Entanglement spectrum of a topological phase in one dimension, Physical review b **81**, 064439 (2010).

[64] H. Nakano, H. Tadano, N. Todoroki, and T. Sakai, The haldane gap of the s= 1 heisenberg antiferromagnetic chain, Journal of the Physical Society of Japan **91**, 074701 (2022).

[65] X. Chen, Z.-C. Gu, and X.-G. Wen, Complete classification of one-dimensional gapped quantum phases in interacting spin systems, Physical review b **84**, 235128 (2011).

[66] S. Zvyagin, J. Wosnitza, C. Batista, M. Tsukamoto, N. Kawashima, J. Krzystek, V. Zapf, M. Jaime, N. Oliveira Jr, and A. Paduan-Filho, Magnetic excitations in the spin-1 anisotropic heisenberg antiferromagnetic chain system nicl 2- 4 sc (nh 2) 2, Physical review letters **98**, 047205 (2007).

[67] T. Giamarchi, C. Rüegg, and O. Tchernyshyov, Bose–einstein condensation in magnetic insulators, Nature Physics **4**, 198 (2008).

[68] Readers familiar with differential geometry will know that the expression for the volume in Eq. 17 can be stated equivalently in terms of the magnitude of the cross product of the tangent vectors (or in our case tangent operators), $|\Lambda_\theta \times \Lambda_\phi|$. This can be seen to be equivalent to the determinant of the quantum metric by considering the Lagrange identity, which, for vectors in $\mathbb{R}^3$, is given by, $|\vec{a} \times \vec{b}|^2 = (\vec{a} \cdot \vec{a})(\vec{b} \cdot \vec{b}) - (\vec{a} \cdot \vec{b})^2$. Consistency with the definitions in Eq. 17 and Eq. 16 is achieved by identifying the dot product with the covariance. This is also consistent with the form of the quantum metric as having matrix elements defined by the inner products of the tangent operators.
It might be tempting to start from the expression $|\Lambda_\theta \times \Lambda_\phi|$ and assume that the correct notion of the cross product would be achieved by evaluating the commutator between the operators Λ_θ and Λ_ϕ. In fact this is not

the case, as taking such a commutator for the case of the staggered magnetization generator defined in Eq. 14 would yield the uniform magnetization operator, which would be inconsistent with the definition of the three tangent operators given in Eq. 15.

[69] M. P. Do Carmo and J. Flaherty Francis, *Riemannian geometry*, Vol. 6 (Springer, 1992).

[70] M. Fishman, S. R. White, and E. M. Stoudenmire, The ITensor software library for tensor network calculations (2020), arXiv:2007.14822.

[71] D. V. Else, I. Schwarz, S. D. Bartlett, and A. C. Doherty, Symmetry-protected phases for measurement-based quantum computation, Physical review letters **108**, 240505 (2012).

[72] R. Raussendorf, W. Yang, and A. Adhikary, Measurement-based quantum computation in finite one-dimensional systems: string order implies computational power, arXiv preprint arXiv:2210.05089 (2022).

[73] A. Auerbach, *Interacting electrons and quantum magnetism* (Springer Science & Business Media, 2012).

Chapter 5

Conclusion

> "Geometry has always struck me as a kind of express lane to truth."

<div align="right">S. T. Yau</div>

In this thesis we have explored the applications of quantum information geometry to the study of multipartite entanglement in low dimensional quantum spin systems. Our work has demonstrated that the QFIM associated with operators that are linear in the spin degrees of freedom can detect genuine multipartite entanglement in the spin-1 anti-ferromagnetic Heisenberg model. A key application of this study is to the implementation of measurement based quantum computation (MBQC) [93], where SPT states are viewed as resources of entanglement. The analyses in Papers I and III add further evidence that the entanglement in SPT systems is robust to both finite temperature and the application of magnetic fields.

While operators that are linear in the spin degrees of freedom don't detect genuine multipartite entanglement in the long range entangled phases of the Kitaev honeycomb model, we have demonstrated that the quantum Fisher information associated with the magnetization operators probed by neutron scattering experiments exhibit a diverging second derivative as a function of the driving parameters of the phase transitions in that model.

The primary conclusion of this thesis is that the state space geometry associated with the ground state manifold of quantum many body systems exhibit strong responses to the criticality, including at finite temperature. These quantum critical points can produce long range effects in the state space, influencing the geometry even far from the critical points themselves. This is sharply illustrated in Paper III where we demonstrate that the presence of genuine multipartite is associated with curvature in the quantum state space which extends away from the quantum critical points and into the neighbouring phases. By considering primarily manifolds generated by sums of the spin degrees of freedom we have maintained close contact between genuine multipartite entanglement, state space geometry, and neutron scattering experiments which have recently begun to probe the genuine multipartite entanglement in terms of quantum Fisher information.

A major open question is the generality of the relationship between state space curvature in terms of local operators and multipartite entanglement. Is curvature ubiquitous in short range entangled phases? Do long range entangled phases exhibit state space curvature that might be used to verify the presence of topological order? The relationship between entanglement and curvature looks tantalizingly similar to the relationship between mass and state space curvature in general relativity and deserves further investigation.

Appendices

Appendix A

Properties of Shannon Information

In this appendix we discuss some properties of information measures. We use $P = \{p_1, ..., p_N\}$ to denote a discrete distribution. The Shannon information defined in Eq. 1.4 has the following properties [4],

- *Positivity*, $S(P) \geq 0$

- *Continuity*, $S(P)$ will vary continuous with the distribution P.

- *Expansibility*, $S(p_1, ..., p_N) = S(p_1, ..., p_N, 0)$.

- *Concavity*, $S(\alpha P_1 + (1 - \alpha)P_2) \geq \alpha S(P_1) + (1 - \alpha)S(P_2)$. The mixing of distributions always increases the information.

- *Subadditivity* For two random variables, not necessarily independent, where p_{12} is the joint probability distribution,

$$S(P_{12}) \leq S(P_1) + S(P_2) \tag{A.1}$$

  with equality only if the two distributions are independent.

- *Recursion.* We can coarse grain a distribution $P = p_1, \ldots, p_N$, via,

$$q_j = \sum_{i=k_{j-1}+1}^{k_j} p_i \tag{A.2}$$

where $j = 1, \ldots, r$ and $k_0 = 0$. The discrete distribution has been partition according to the sum $N = \sum_{i=1}^{r} k_i$. Then the Shannon information is given by,

$$S(P) = S(Q) + q_1 S\left(\frac{p_1}{q_1}, \ldots, \frac{p_{k_1}}{q_1}\right) + \ldots + q_r S\left(\frac{p_{k_{N-k_r+1}}}{q_r}, \ldots, \frac{p_N}{q_r}\right) \quad \text{(A.3)}$$

It is the property of recursion that makes the Shannon information unique amongst all possible choice of information measure. It appears in many other interesting contexts. In particular in the field of signal transmission where it was originally developed.

88

Appendix B

Example Calculations

B.1 Single Qubit

We may compute the trace explicitly by diagonalizing the Hamiltonian with source term. We denote the coefficients of the magnetization operator as m_α (no hat) and temporarily suppress the explicit dependence on θ and ϕ

$$\hat{H} \doteq \begin{pmatrix} \Delta - hm_z & h(m_x - im_y) \\ h(m_x + im_y) & -(\Delta - hm_z) \end{pmatrix}$$

We can immediately read off the eigenvalues for this matrix,

$$\lambda_\pm = \pm\sqrt{(\Delta - hm_z)^2 + h^2(m_x - im_y)(m_x + im_y)}$$
$$= \pm\sqrt{\Delta^2 - 2\Delta m_z h + h^2}$$

and thus find,

$$\mathcal{Z}(h) = 2\cosh\left(\beta\sqrt{\Delta^2 - 2\Delta m_z h + h^2}\right) \tag{B.1}$$

The variance is given by,

$$\mathrm{Var}(\hat{M}) = \mathrm{tr}\left(\rho\hat{M}^2\right) - \mathrm{tr}\left(\rho\hat{M}\right)^2$$
$$= 1 - \tanh^2(\beta|\Delta|)\cos^2(\phi) \tag{B.2}$$

89

The thermal variance can be evaluated by first computing the first and second derivatives of the partition function with respect to the driving field,

$$
\begin{aligned}
\partial_{h=0}\mathcal{Z} &= \partial_{h=0}2\cosh\left(\beta\sqrt{\Delta^2 - 2\Delta m_z h + h^2}\right) \\
&= 2\beta\left(\frac{\sinh\left(\beta\sqrt{\Delta^2 - 2\Delta m_z h + h^2}\right)}{\sqrt{\Delta^2 - 2\Delta m_z h + h^2}}(h - \Delta m_z)\right)_{h=0} \\
&= -2\beta\mathrm{sgn}(\Delta)m_z\sinh(\beta|\Delta|) \tag{B.3a}
\end{aligned}
$$

$$
\begin{aligned}
\partial_{h=0}^2\mathcal{Z} &= \left(2\beta^2\frac{\cosh\left(\beta\sqrt{\Delta^2 - 2\Delta m_z h + h^2}\right)}{\Delta^2 - 2\Delta m_z h + h^2}(h - \Delta m_z)^2\right. \\
&\quad -2\beta\frac{\sinh\left(\beta\sqrt{\Delta^2 - 2\Delta m_z h + h^2}\right)}{(\Delta^2 - 2\Delta m_z h + h^2)^{\frac{3}{2}}}(h - \Delta m_z)^2 \\
&\quad \left.+ 2\beta\frac{\sinh\left(\beta\sqrt{\Delta^2 - 2\Delta m_z h + h^2}\right)}{\sqrt{\Delta^2 - 2\Delta m_z h + h^2}}\right)_{h=0} \\
&= 2\beta^2\cosh(\beta|\Delta|)m_z^2 - 2\beta\frac{\sinh(\beta|\Delta|)}{|\Delta|}m_z^2 + 2\beta\frac{\sinh(\beta|\Delta|)}{|\Delta|} \\
&= 2\beta^2\cosh(\beta|\Delta|)m_z^2 + 2\beta(1 - m_z^2)\frac{\sinh(\beta|\Delta|)}{|\Delta|} \tag{B.3b}
\end{aligned}
$$

No we substitute these relations into the definition of the thermal variance which we restate below,

$$
\begin{aligned}
\mathrm{Var}_{\mathcal{T}}(\hat{M};\hat{\rho}) &= \frac{1}{\beta^2}\left(\frac{1}{\mathcal{Z}(h=0)}\left(\frac{\partial^2\mathcal{Z}}{\partial h^2}\right)_{h=0} - \frac{1}{\mathcal{Z}^2(h=0)}\left(\frac{\partial\mathcal{Z}}{\partial h}\right)^2_{h=0}\right) \\
&= \frac{1}{\beta^2}\left(\beta^2 m_z^2 + \beta(1 - m_z^2)\frac{\tanh(\beta|\Delta|)}{|\Delta|} - \beta^2 m_z^2\tanh^2(\beta|\Delta|)\right) \\
&= m_z^2 + (1 - m_z^2)\frac{\tanh(\beta|\Delta|)}{\beta|\Delta|} - m_z^2\tanh^2(\beta|\Delta|) \\
&= m_z^2(1 - \tanh^2(\beta|\Delta|)) + (1 - m_z^2)\frac{\tanh(\beta|\Delta|)}{\beta|\Delta|} \tag{B.4}
\end{aligned}
$$

The QV can be computed by substituting Eq. B.2 and Eq. B.4 into Eq. 1.72,

$$\text{Var}_\mathcal{Q}(\hat{M}; \hat{\rho}) = 1 - \tanh^2(\beta|\Delta|)m_z^2 - m_z^2(1 - \tanh^2(\beta|\Delta|)) - (1 - m_z^2)\frac{\tanh(\beta|\Delta|)}{\beta|\Delta|}$$

$$= (1 - m_z^2)\left(1 - \frac{\tanh(\beta|\Delta|)}{\beta|\Delta|}\right) \tag{B.5}$$

Using Eq. 1.46, we can calculate an explicit form of the QFI for the single qubit as well. Since diagonal entries don't contribute to the QFI, we consider only off diagonal terms, and denote by $\lambda_\pm = \pm\Delta$ the two eigenvalues and eigenstates of the Hamiltonian. We denote the corresponding eigenstates of σ^z by $|\pm\rangle$. The QFI given by,

$$\mathcal{F}(\hat{M}; \hat{\rho}) = 2\sum_{\lambda,\lambda'}\frac{(p_\lambda - p_{\lambda'})^2}{p_\lambda + p_{\lambda'}}\left|\langle\lambda|\hat{M}|\lambda'\rangle\right|^2$$

$$= 4\frac{(p_+ - p_-)^2}{p_+ + p_-}\left|\langle+|\hat{M}|-\rangle\right|^2$$

$$= \frac{4}{\mathcal{Z}}\frac{(e^{-\beta|\Delta|} - e^{\beta|\Delta|})^2}{e^{-\beta|\Delta|} + e^{\beta|\Delta|}}(m_x^2 + m_y^2)$$

$$= \frac{4}{\mathcal{Z}}\frac{4\sinh^2(\beta|\Delta|)}{2\cosh(\beta|\Delta|)}(1 - m_z^2)$$

$$= 4\tanh^2(\beta|\Delta|)(1 - m_z^2)$$

$$= 4\tanh^2(\beta|\Delta|)\sin^2(\phi) \tag{B.6}$$

Bibliography

[1] Claude Elwood Shannon. A mathematical theory of communication. *The Bell system technical journal*, 27(3):379–423, 1948.

[2] Solomon Kullback and Richard A Leibler. On information and sufficiency. *The annals of mathematical statistics*, 22(1):79–86, 1951.

[3] Ivan N Sanov. *On the probability of large deviations of random variables*. United States Air Force, Office of Scientific Research, 1958.

[4] Ingemar Bengtsson and Karol Życzkowski. *Geometry of quantum states: an introduction to quantum entanglement*. Cambridge university press, 2017.

[5] Ronald A Fisher. On the mathematical foundations of theoretical statistics. *Philosophical transactions of the Royal Society of London. Series A, containing papers of a mathematical or physical character*, 222(594-604):309–368, 1922.

[6] Ronald Aylmer Fisher. Theory of statistical estimation. In *Mathematical proceedings of the Cambridge philosophical society*, volume 22, pages 700–725. Cambridge University Press, 1925.

[7] Anil Bhattacharyya. On a measure of divergence between two multinomial populations. *Sankhyā: the indian journal of statistics*, pages 401–406, 1946.

[8] NN Cencov. Statistical decision rules and optimal inference, transl. math. monographs, vol. 53. *Amer. Math. Soc., Providence-RI*, 1981.

[9] C Radhakrishna Rao. Information and the accuracy attainable in the estimation of statistical parameters. *Reson. J. Sci. Educ*, 20:78–90, 1945.

[10] John Von Neumann. *Mathematical foundations of quantum mechanics: New edition*. Princeton university press, 2018.

[11] Frank Pollmann, Ari M Turner, Erez Berg, and Masaki Oshikawa. Entanglement spectrum of a topological phase in one dimension. *Physical review b*, 81(6):064439, 2010.

[12] Luigi Amico, Rosario Fazio, Andreas Osterloh, and Vlatko Vedral. Entanglement in many-body systems. *Reviews of modern physics*, 80(2):517, 2008.

[13] Pasquale Calabrese and John Cardy. Entanglement entropy and conformal field theory. *Journal of physics a: mathematical and theoretical*, 42(50):504005, 2009.

[14] Alexei Kitaev and John Preskill. Topological entanglement entropy. *Physical review letters*, 96(11):110404, 2006.

[15] Jens Eisert, Marcus Cramer, and Martin B Plenio. Colloquium: Area laws for the entanglement entropy. *Reviews of modern physics*, 82(1):277, 2010.

[16] William K Wootters. Statistical distance and hilbert space. *Physical Review D*, 23(2):357, 1981.

[17] Samuel L Braunstein and Carlton M Caves. Statistical distance and the geometry of quantum states. *Physical Review Letters*, 72(22):3439, 1994.

[18] GW Gibbons. Typical states and density matrices. *Journal of Geometry and Physics*, 8(1-4):147–162, 1992.

[19] Guido Fubini. *Sulle metriche definite da una forma hermitiana: nota*. Office graf. C. Ferrari, 1904.

[20] Eduard Study. Kürzeste wege im komplexen gebiet. *Mathematische Annalen*, 60(3):321–378, 1905.

[21] Alexander S Holevo. *Probabilistic and statistical aspects of quantum theory*, volume 1. Springer Science & Business Media, 2011.

[22] Elena Aleksandrovna Morozova and Nikolai Nikolaevich Chentsov. Markov invariant geometry on state manifolds. *Itogi Nauki i Tekhniki. Seriya" Sovremennye Problemy Matematiki. Noveishie Dostizheniya"*, 36:69–102, 1989.

[23] Tomohiro Shitara and Masahito Ueda. Determining the continuous family of quantum fisher information from linear-response theory. *Physical Review A*, 94(6):062316, 2016.

[24] Philipp Hauke, Markus Heyl, Luca Tagliacozzo, and Peter Zoller. Measuring multipartite entanglement through dynamic susceptibilities. *Nature Physics*, 12(8):778–782, 2016.

[25] Géza Tóth and Dénes Petz. Extremal properties of the variance and the quantum fisher information. *Physical Review A*, 87(3):032324, 2013.

[26] Donald Bures. An extension of kakutani's theorem on infinite product measures to the tensor product of semifinite w*-algebras. *Transactions of the American Mathematical Society*, 135:199–212, 1969.

[27] Armin Uhlmann. The "transition probability" in the state space of a $\star$-algebra. *Reports on Mathematical Physics*, 9(2):273–279, 1976.

[28] Géza Tóth. Multipartite entanglement and high-precision metrology. *Physical Review A*, 85(2):022322, 2012.

[29] Jens Eisert, Marcus Cramer, and Martin B Plenio. Area laws for the entanglement entropy-a review. *arXiv preprint arXiv:0808.3773*, 2008.

[30] Philipp Hyllus, Wiesław Laskowski, Roland Krischek, Christian Schwemmer, Witlef Wieczorek, Harald Weinfurter, Luca Pezzé, and Augusto Smerzi. Fisher information and multiparticle entanglement. *Physical Review A*, 85(2):022321, 2012.

[31] Allen Scheie, Pontus Laurell, AM Samarakoon, B Lake, SE Nagler, GE Granroth, S Okamoto, G Alvarez, and DA Tennant. Witnessing entanglement in quantum magnets using neutron scattering. *Physical Review B*, 103(22):224434, 2021.

[32] Pontus Laurell, Allen Scheie, Chiron J Mukherjee, Michael M Koza, Mechtild Enderle, Zbigniew Tylczynski, Satoshi Okamoto, Radu Coldea, D Alan Tennant, and Gonzalo Alvarez. Quantifying and controlling entanglement in the quantum magnet cs 2 cocl 4. *Physical Review Letters*, 127(3):037201, 2021.

[33] Luca Pezze, Marco Gabbrielli, Luca Lepori, and Augusto Smerzi. Multipartite entanglement in topological quantum phases. *Physical review letters*, 119(25):250401, 2017.

[34] Xie Chen, Zheng-Cheng Gu, and Xiao-Gang Wen. Complete classification of one-dimensional gapped quantum phases in interacting spin systems. *Physical review b*, 84(23):235128, 2011.

[35] Marco Gabbrielli, Augusto Smerzi, and Luca Pezzè. Multipartite entanglement at finite temperature. *Scientific reports*, 8(1):1–18, 2018.

[36] Paolo Zanardi, Paolo Giorda, and Marco Cozzini. Information-theoretic differential geometry of quantum phase transitions. *Physical review letters*, 99(10):100603, 2007.

[37] Michael Victor Berry. Quantal phase factors accompanying adiabatic changes. *Proceedings of the Royal Society of London. A. Mathematical and Physical Sciences*, 392(1802):45–57, 1984.

[38] James Lambert and Erik S Sørensen. State space geometry of the spin-1 antiferromagnetic heisenberg chain. *arXiv preprint arXiv:2209.05005*, 2022.

[39] Paolo Zanardi and Nikola Paunković. Ground state overlap and quantum phase transitions. *Physical Review E*, 74(3):031123, 2006.

[40] Shi-Jian Gu, Ho-Man Kwok, Wen-Qiang Ning, Hai-Qing Lin, et al. Fidelity susceptibility, scaling, and universality in quantum critical phenomena. *Physical Review B*, 77(24):245109, 2008.

[41] Paolo Zanardi, Lorenzo Campos Venuti, and Paolo Giorda. Bures metric over thermal state manifolds and quantum criticality. *Physical Review A*, 76(6):062318, 2007.

[42] Jing Liu, Heng-Na Xiong, Fei Song, and Xiaoguang Wang. Fidelity susceptibility and quantum fisher information for density operators with arbitrary ranks. *Physica A: Statistical Mechanics and its Applications*, 410:167–173, 2014.

[43] Lorenzo Campos Venuti and Paolo Zanardi. Quantum critical scaling of the geometric tensors. *Physical review letters*, 99(9):095701, 2007.

[44] Michael Kolodrubetz, Vladimir Gritsev, and Anatoli Polkovnikov. Classifying and measuring geometry of a quantum ground state manifold. *Physical Review B*, 88(6):064304, 2013.

[45] Shuo Yang, Shi-Jian Gu, Chang-Pu Sun, and Hai-Qing Lin. Fidelity susceptibility and long-range correlation in the kitaev honeycomb model. *Physical Review A*, 78(1):012304, 2008.

[46] Shi-Jian Gu and Hai-Qing Lin. Scaling dimension of fidelity susceptibility in quantum phase transitions. *EPL (Europhysics Letters)*, 87(1):10003, 2009.

[47] Silvano Garnerone, Damian Abasto, Stephan Haas, and Paolo Zanardi. Fidelity in topological quantum phases of matter. *Physical Review A*, 79(3):032302, 2009.

[48] Michael Kolodrubetz, Dries Sels, Pankaj Mehta, and Anatoli Polkovnikov. Geometry and non-adiabatic response in quantum and classical systems. *Physics Reports*, 697:1–87, 2017.

[49] Irénée Frérot and Tommaso Roscilde. Quantum variance: a measure of quantum coherence and quantum correlations for many-body systems. *Physical Review B*, 94(7):075121, 2016.

[50] Eugene P Wigner and Mutsuo M Yanase. Information contents of distributions. In *Part I: Particles and Fields. Part II: Foundations of Quantum Mechanics*, pages 452–460. Springer, 1997.

[51] Eugene P Wigner and Mutsuo M Yanase. On the positive semidefinite nature of a certain matrix expression. *Canadian journal of mathematics*, 16:397–406, 1964.

[52] Anders W Sandvik and Juhani Kurkijärvi. Quantum monte carlo simulation method for spin systems. *Physical Review B*, 43(7):5950, 1991.

[53] Jorge E Hirsch, Robert L Sugar, Doug J Scalapino, and Richard Blankenbecler. Monte carlo simulations of one-dimensional fermion systems. *Physical Review B*, 26(9):5033, 1982.

[54] Ansgar Dorneich and Matthias Troyer. Accessing the dynamics of large many-particle systems using the stochastic series expansion. *Physical Review E*, 64(6):066701, 2001.

[55] Irénée Frérot and Tommaso Roscilde. Reconstructing the quantum critical fan of strongly correlated systems using quantum correlations. *Nature communications*, 10(1):1–7, 2019.

[56] Daniele Malpetti and Tommaso Roscilde. Quantum correlations, separability, and quantum coherence length in equilibrium many-body systems. *Physical review letters*, 117(13):130401, 2016.

[57] Elliott Lieb, Theodore Schultz, and Daniel Mattis. Two soluble models of an antiferromagnetic chain. *Annals of Physics*, 16(3):407–466, 1961.

[58] F Duncan M Haldane. Continuum dynamics of the 1-d heisenberg antiferromagnet: Identification with the o (3) nonlinear sigma model. *Physics letters a*, 93(9):464–468, 1983.

[59] F Duncan M Haldane. Nonlinear field theory of large-spin heisenberg antiferromagnets: semiclassically quantized solitons of the one-dimensional easy-axis néel state. *Physical review letters*, 50(15):1153, 1983.

[60] WJ L Buyers, RM Morra, RL Armstrong, MJ Hogan, P Gerlach, and K Hirakawa. Experimental evidence for the haldane gap in a spin-1 nearly isotropic, antiferromagnetic chain. *Physical review letters*, 56(4):371, 1986.

[61] JP Renard, LP Regnault, and M Verdaguer. Experimental evidences for an haldane gap in quasi one-dimensional antiferromagnets. *Le Journal de Physique Colloques*, 49(C8):C8–1425, 1988.

[62] Ian Affleck, Tom Kennedy, Elliott H Lieb, and Hal Tasaki. Valence bond ground states in isotropic quantum antiferromagnets. In *Condensed matter physics and exactly soluble models*, pages 253–304. Springer, 1988.

[63] Xiao-Gang Wen. Topological orders and edge excitations in fractional quantum hall states. *Advances in Physics*, 44(5):405–473, 1995.

[64] Frank Pollmann, Erez Berg, Ari M Turner, and Masaki Oshikawa. Symmetry protection of topological phases in one-dimensional quantum spin systems. *Physical review b*, 85(7):075125, 2012.

[65] Erik S Sørensen and Ian Affleck. Large-scale numerical evidence for bose condensation in the s= 1 antiferromagnetic chain in a strong field. *Physical review letters*, 71(10):1633, 1993.

[66] SA Zvyagin, J Wosnitza, CD Batista, M Tsukamoto, N Kawashima, J Krzystek, VS Zapf, M Jaime, NF Oliveira Jr, and A Paduan-Filho. Magnetic excitations in the spin-1 anisotropic heisenberg antiferromagnetic chain system nicl 2- 4 sc (nh 2) 2. *Physical review letters*, 98(4):047205, 2007.

[67] Thierry Giamarchi, Christian Rüegg, and Oleg Tchernyshyov. Bose–einstein condensation in magnetic insulators. *Nature Physics*, 4(3):198–204, 2008.

[68] Hiroki Nakano, Hiroto Tadano, Norikazu Todoroki, and Tôru Sakai. The haldane gap of the s= 1 heisenberg antiferromagnetic chain. *Journal of the Physical Society of Japan*, 91(7):074701, 2022.

[69] Carl W Helstrom and Carl W Helstrom. *Quantum detection and estimation theory*, volume 84. Academic press New York, 1976.

[70] Alexander S Holevo. *Statistical structure of quantum theory*, volume 67. Springer Science & Business Media, 2003.

[71] Samuel L Braunstein, Carlton M Caves, and Gerard J Milburn. Generalized uncertainty relations: theory, examples, and lorentz invariance. *annals of physics*, 247(1):135–173, 1996.

[72] Luca Pezze, Augusto Smerzi, Markus K Oberthaler, Roman Schmied, and Philipp Treutlein. Quantum metrology with nonclassical states of atomic ensembles. *Reviews of Modern Physics*, 90(3):035005, 2018.

[73] Jing Liu, Haidong Yuan, Xiao-Ming Lu, and Xiaoguang Wang. Quantum fisher information matrix and multiparameter estimation. *Journal of Physics A: Mathematical and Theoretical*, 53(2):023001, 2019.

[74] JP Provost and G Vallee. Riemannian structure on manifolds of quantum states. *Communications in Mathematical Physics*, 76(3):289–301, 1980.

[75] Lei Wang, Ye-Hua Liu, Jakub Imriška, Ping Nang Ma, and Matthias Troyer. Fidelity susceptibility made simple: A unified quantum monte carlo approach. *Physical Review X*, 5(3):031007, 2015.

[76] Daniel Gutiérrez-Ruiz, Jorge Chávez-Carlos, Diego Gonzalez, Jorge G Hirsch, and J David Vergara. Quantum metric tensor of the dicke model: Analytical and numerical study. *Physical Review B*, 105(21):214106, 2022.

[77] Tomoki Ozawa and Bruno Mera. Relations between topology and the quantum metric for chern insulators. *arXiv preprint arXiv:2103.11582*, 2021.

[78] Yu-Quan Ma, Shi-Jian Gu, Shu Chen, Heng Fan, and Wu-Ming Liu. The euler number of bloch states manifold and the quantum phases in gapped fermionic systems. *EPL (Europhysics Letters)*, 103(1):10008, 2013.

[79] Tomoki Ozawa and Nathan Goldman. Extracting the quantum metric tensor through periodic driving. *Physical Review B*, 97(20):201117, 2018.

[80] Bruno Mera and Tomoki Ozawa. Kähler geometry and chern insulators: Relations between topology and the quantum metric. *Physical Review B*, 104(4):045104, 2021.

[81] Anwei Zhang. Revealing chern number from quantum metric. *Chinese Physics B*, 31(4):040201, 2022.

[82] Cameron JD Kemp, Nigel R Cooper, and F Nur Ünal. Nested spheres description of the n-level chern number and the generalized bloch hypersphere. *arXiv preprint arXiv:2110.06934*, 2021.

[83] Xinsheng Tan, Dan-Wei Zhang, Zhen Yang, Ji Chu, Yan-Qing Zhu, Danyu Li, Xiaopei Yang, Shuqing Song, Zhikun Han, Zhiyuan Li, et al. Experimental measurement of the quantum metric tensor and related topological phase transition with a superconducting qubit. *Physical review letters*, 122(21):210401, 2019.

[84] Min Yu, Pengcheng Yang, Musang Gong, Qingyun Cao, Qiuyu Lu, Haibin Liu, Shaoliang Zhang, Martin B Plenio, Fedor Jelezko, Tomoki Ozawa, et al. Experimental measurement of the quantum geometric tensor using coupled qubits in diamond. *National science review*, 7(2):254–260, 2020.

[85] Wan-Fang Liu, Jian Ma, and Xiaoguang Wang. Quantum fisher information and spin squeezing in the ground state of the xy model. *Journal of Physics A: Mathematical and Theoretical*, 46(4):045302, 2013.

[86] Jordyn Hales, Utkarsh Bajpai, Tongtong Liu, Denitsa R Baykusheva, Mingda Li, Matteo Mitrano, and Yao Wang. Witnessing light-driven entanglement using time-resolved resonant inelastic x-ray scattering. *arXiv preprint arXiv:2209.02283*, 2022.

[87] Qiang Zheng, Yao Yao, and Xun-Wei Xu. Probing berezinskii–kosterlitz–thouless phase transition of spin-half xxz chain by quantum fisher information. *Communications in Theoretical Physics*, 63(3):279, 2015.

[88] Song-Song Li, Hong-Gang Yi, and Rong-Hua Chen. Spin squeezing and quantum fisher information in the lipkin-meshkov-glick model. *International Journal of Theoretical Physics*, 52(4):1175–1181, 2013.

[89] Yu-Chin Tzeng and Min-Fong Yang. Scaling properties of fidelity in the spin-1 anisotropic model. *Physical Review A*, 77(1):012311, 2008.

[90] A Langari, F Pollmann, and M Siahatgar. Ground-state fidelity of the spin-1 heisenberg chain with single ion anisotropy: quantum renormalization group and exact diagonalization approaches. *Journal of Physics: Condensed Matter*, 25(40):406002, 2013.

[91] Irénée Frérot and Tommaso Roscilde. Quantum critical metrology. *Physical review letters*, 121(2):020402, 2018.

[92] Lucile Savary and Leon Balents. Quantum spin liquids: a review. *Reports on Progress in Physics*, 80(1):016502, 2016.

[93] Hans J Briegel, David E Browne, Wolfgang Dür, Robert Raussendorf, and Maarten Van den Nest. Measurement-based quantum computation. *Nature Physics*, 5(1):19–26, 2009.